2011

Evanescent Wave Coupling Using Different Subwavelength Gratings for a MEMS Accelerometer

Al-Aakhir A. Rogers
University of South Florida, al3aakhir@gmail.com

Evanescent Wave Coupling Using Different Subwavelength Gratings for a MEMS Accelerometer

by

Al-Aakhir A. Rogers

A dissertation submitted in the partial fulfillment
of the requirements for degree of
Doctor of Philosophy
Department of Electrical Engineering
College of Engineering
University of South Florida

Co-Major Professor: Shekhar Bhansali, Ph.D.
Co-Major Professor: Scott Samson, Ph.D.
Rasim Guldiken, Ph.D.
Andrew Hoff, Ph.D.
Myung Kim, Ph.D.
Jing Wang, Ph.D.

Date of Approval:
March 28, 2011

Keywords: Accelerometer, Infrared, Output Intensity, Micromachining, FDTD

Dedication

As a child, my great-grandfather, Heyward “Da-Da” Brandon spoke into my life unlike anyone else. I used to wonder if he knew my real name because he always called me “Preacher Man”. He persisted in calling me “Preacher Man”, even into adulthood. I am thankful that before he went home to be with the Lord I was able to show him how powerful his words were. I became that “Preacher Man” he always called me.

I dedicate this manuscript in memory of “Da-Da” who would remind me of Colossians 3:23, “Whatever you do, work at it with all your heart, as working for the Lord, not for men.”

Acknowledgements

I would like to thank Dr. Shekhar Bhansali (Shake-daddy) for giving me a chance and the opportunity to pursue my doctoral studies. The type of teaching and training that Dr. Bhansali implemented are skills that aren't taught in the classroom. Thank you for passing on to me such an unconventional skill set. Dr. Scott Samson, my co-major professor, I would like to thank you for your mentoring. Every word that you spoke, I hung on to. I want to thank you for your patience, mentorship, and integrity. I want to thank both my co-major professors for their encouragement, guidance and support throughout my Ph.D. program. Additionally, I would like to extend my thanks to the entire SRI© International staff. Special thanks to Dave Edwards for EBL and SEM training, Dr. Rahul Agarwal for his guidance, Dr. Raj Popuri and Sunny Kedia for fabrication support and testing.

I want to thank Mr. Bernard Batson for being the "Mr. Everything". Thank you for looking after me, for seeing that I received the proper instruction and professional development, for providing every resource imaginable, and being there whenever I needed someone to talk to. I could not have made it without you! Thank you to the Alfred P. Sloan Foundation, the Florida Education Fund's McKnight Doctoral Fellowship and the National Science Foundation for providing financial support under the following grants: NSF S-STEM Award #0807023, NSF CMMI Award # 0700659, NSF Florida-Georgia LSAMP Award # 0217675.

I would also like to thank Dr. Ashanti Johnson Turner for introducing and getting me to come to USF. The BioMEMS and Microsystems group and the Bridge to the Doctorate Fellowship program for presentation and poster critiques, proposal editing, manuscript feedback, and professional and emotional support. Special thanks to Dr. Praveen Sekhar Kumar, Dr. Subramanian Krishnan, and Dorielle Price for their technical writing support and key input to having accepted journal publications.

I would like to thank my fifth grade teacher, Malcolm Bialik who believed in me at an early age; Coach Darrell G. Moore, my high school wrestling coach who taught me to believe in myself and touched my life in a very special way; Dr. Anthony B. Stinson, my high school AP Calculus teacher who would not let me slack off; Kareem Hogan my Circuits I TA for getting me interested in graduate school. Thank you for being committed to making a difference in my life.

I would like to thank my family in Georgia and New York for their support, encouragement, love, and sacrifices during my graduate studies. Pastors Otis Lockett, Jason Hancock, Darryl Bass, Elder Michael T. Lewis, and the Evangel Fellowship Church, for growing me up and sending me out. Pastor Aubrey Shines and Glory to Glory Ministries for being with me during this entire journey. Without them it wouldn't have been possible for me to complete this work and this manuscript.

Last but not the least I would like to thank my Lord and Savior Jesus Christ for the gift of faith. Faith to begin a journey; faith to speak to the obstacles; faith to run and not faint; and faith to endure to the end. I love you mommy!

Table of Contents

List of Tables

List of Figures

Abstract

A novel technique of coupling near-field evanescent waves by means of variable period subwavelength gratings (1.2 μm and 1.0 μm), using a 1.55 μm infrared semiconductor laser is presented for the use of an optical MEMS accelerometer. The subwavelength gratings were fabricated on both glass and silicon substrates respectively.

Optical simulation of the subwavelength gratings was carried out to obtain the maximum coupling efficiency of the two subwavelength gratings; the grating thickness, grating width, and the grating separation were optimized. This was performed for both silicon and glass substrates.

The simulations were used to determine the total system noise, including the noise generated from the germanium photodiode, sensitivity, and displacement detection resolution of the coupled subwavelength grating MEMS accelerometer. The coupled gratings were utilized as optical readout accelerometers.

The spring/proof mass silicon accelerometer was fabricated using a four mask process, in which the structure was completed using two deep reactive ion etching (DRIE) processes. The designed serpentine spring styles determine the sensitivity of the accelerometer; when the springs are made longer or shorter, thicker or thinner, this directly attributes to the sensitivity of the device.

To test function of the example of the devices, the accelerometer is placed on a platform, which permits displacement normal to the plane of the grating. The 1.550 μm infrared laser is incident on the coupled subwavelength grating accelerometer device and the output intensity is measured using a geranium photodiode. As the platform is displaced, the grating separation between the two gratings changes and causes the output intensity to change. Using the coupled subwavelength grating simulations as a reference to the output intensity change with respect to gap, the mechanical and coupling sensitivity properties of as it relates to acceleration is presented.

Chapter 1

Introduction

1.1 Overview of Gratings and Subwavelength Gratings

Gratings are optical elements with properties of dispersing and diffracting light. There are many types of diffraction gratings, which are specified by their geometry, material, efficiency behavior, fabrication type, and their application [1]. Additionally, these types are classified as either amplitude or phase gratings [2]. Amplitude gratings are made by patterning and or etching a material on top of a substrate, thus affecting only the amplitude of the incident source. Phase gratings are etched into the substrate and influence the phase of the incident wave. Diffraction is observed by reflecting from a reflection grating or by passing through a transmission grating. Typically, reflection gratings are coated with a metal layer in which the incident source is reflected from the grating and transmission grating allows the incident source to pass through the medium.

Selecting a grating is application specific, wherein, the grating efficiency and grating wavelength are common characteristics for grating selection. The grating efficiency is related to the grating shape, incidence angle, and the material properties. The grating wavelength or grating period is the co-contributor to the desired diffraction, the other being the incident wavelength. Diffraction from a grating is visibly seen when the grating period is greater than the wavelength of the illuminating source. This type of

diffraction is known as Fraunhofer diffraction, as illustrated in Figure 1-1. The first grating was created using 50 hairs elongated between two screws with a grating period of 250,000 nm, and was later modified by Joseph von Fraunhofer with metal wire wound about the screws. Fraunhofer's diffraction grating was used to measure the wavelength of the dark absorption lines of the solar spectrum [3, 4].

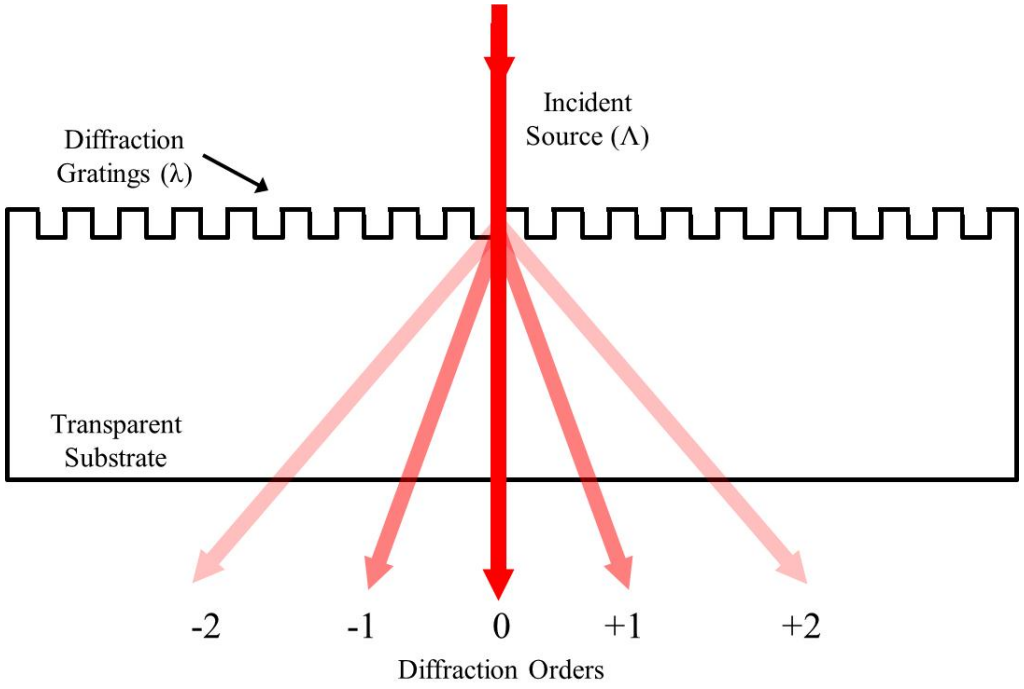

Figure 1-1: Diffraction from a grating

Subwavelength (SW) gratings are spaced, diffractive or reflective optical elements that have a grating wavelength shorter than the incident illumination source. The near field region contains useful non propagating spatial information that information can be retrieved, demodulated, and re-propagated into the visible far field region by coupling it with a second SW grating which has a different grating period. When the period of a grating is below the wavelength of incident source it is considered

SW. These SW gratings do not exhibit any higher diffraction orders and the near field (NF) region where non-propagating evanescent waves (EW) are parallel to the grating surface exist are often filtered out as noise [5]. This diffraction is known as Fresnel diffraction. Since the mid 1960's, these exponentially decreasing EWs have commanded the attention of researchers [6].

There has been wide-ranging research of gratings and particularly, SW gratings. This research includes studying light propagation in singly and doubly periodic planar waveguides [7], high efficiency input coupling using surface corrugations [8], and analysis of thin film waveguides with groove structures [9] to name a few. Gupta and Peng were the first researchers to demonstrate evanescent wave coupling by fabricating SW gratings using interference beam lithography on a glass substrate [10]. Gupta and Peng only compared the diffraction angles from the evanescent coupling and made inferred speculation about the output intensity.

Our research focus is placed on maximizing the output intensity for implementing this technique on a microelectro-mechanical systems (MEMS) accelerometer. This technique will be able to detect highly sensitive, detecting nanometer displacement movements.

1.2 Goal and Objective

In this research near field EW coupling using two SW gratings with different grating periods, creates a larger effective grating period that propagates diffraction orders with grating gap dependent intensities in the far field region will be discussed for assembling and testing a novel MEMS accelerometer. As MEMS accelerometers are further miniaturized, their range of motion is minimized and detecting this sub-nanometer

displacement requires a highly sensitive measurement technique, which can be realized with this coupled grating method. The design of the envisioned accelerometer consist of two chips: a glass chip with 1.2 μm SW gratings etched into the glass using reactive ion etching (RIE) and having a thin gold bond frame outside the grating area, and a silicon chip having a suspended spring/proof mass structure with 1.0 SW gratings etched into the silicon by deep reactive ion etching (DRIE), and also having a thin gold bond frame. This sensor operates in the NF region where EWs exist. In this region, EW coupling from both SW gratings produces far field (FF) diffraction, where output intensity is a function of change in grating separation between the coupled SW gratings and will correlate displacement versus output intensity exhibited by the accelerometer shown in Figure 1-2.

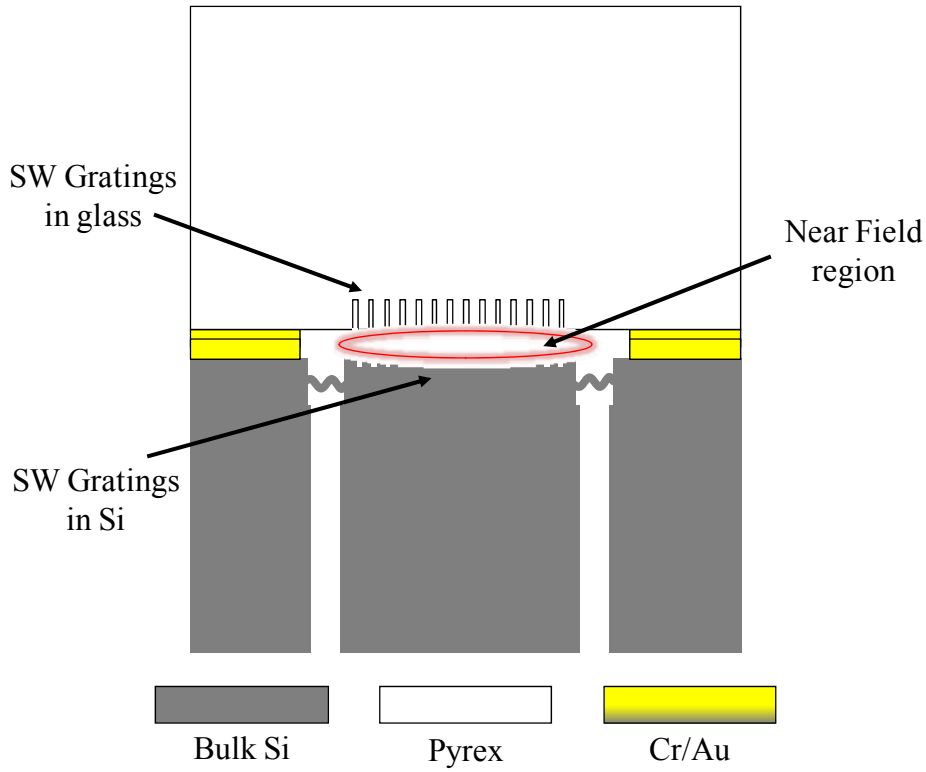

Figure 1-2: Coupled SW grating accelerometer schematic

The proposed optical MEMS accelerometer is advantageous over other accelerometer types in its flexibility and ease of fabrication towards creating a robust sensor, the minimal external disturbances (temperature, electro-magnetic interference, capacitance, etc.) which prevent interference in acceleration measurements, and EW coupling in the near field promoting high sensitivity. Additionally, optical sensing has the potential for high speed readout.

This research explores fabrication of SW gratings with different grating periods to demonstrate the EW coupling concept. This involves placing two SW gratings within the near field region where the non-propagating EWs are coupled and propagated into the far field where visible diffraction orders can be observed show, as represented in Figure 1-3.

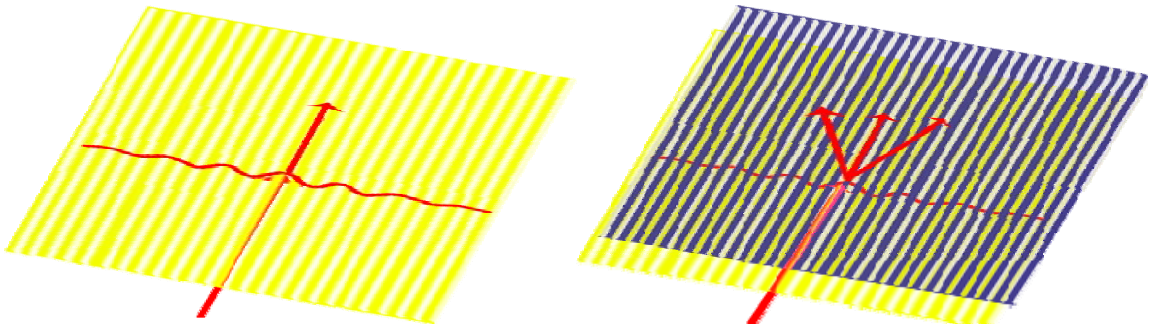

Figure 1-3: Illustration of a single SW grating and coupled SW gratings (a) plane wave source incident on a single SW grating, exhibiting non-propagating EWs and the transmitted 0^{th} order (b) plane wave source incident on a single SW grating, in which the EWs are re-coupled by the secondary SW gratings exhibiting higher diffraction orders

The physical SW grating dimensions (etch depth, grating width, sidewall angle) will be investigated for optimal coupling efficiency. Furthermore, real-time applications for using coupled SW gratings for MEMS sensors would be another research effort.

The goal of fabricating and etching SW gratings into silicon and glass substrates for the purpose of coupling the exponentially decaying EWs into propagating waves visible in the far field is essential to realizing the envisioned accelerometer. This would be accomplished by (a) simulating the effects of single SW gratings, determining the optimum grating thickness of both substrates for maximum coupling efficiency, and coupling the optimum thickness SW gratings with variable grating separations, (b) using nano-lithographic methods for fabricating SW gratings on silicon and glass substrates, (c) controlling the bonding parameters to successfully bond the silicon and glass substrates with gratings to demonstrate the EW coupling concept, and (d) implementing the entire coupled SW gratings proof of concept into a MEMS accelerometer is seen in Figure 1-4.

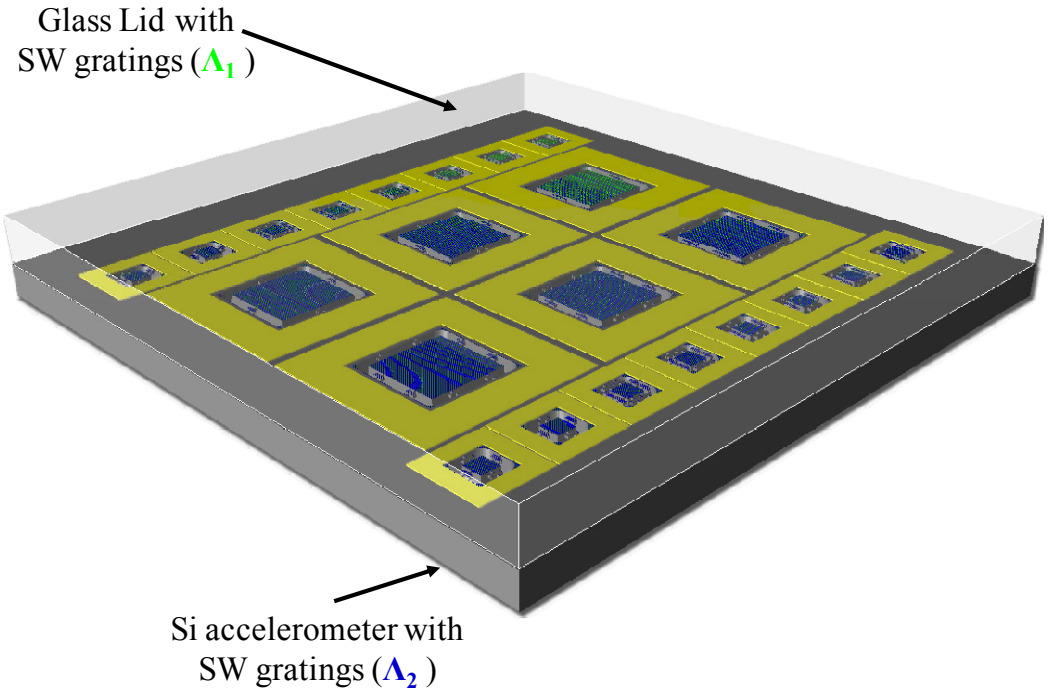

Figure 1-4: 3D Coventorware model of the coupled SW grating accelerometer

The specific goals of this research are detailed in the following objectives:

(a) To use OptiWave™ FDTD software package to compute the electromagnetic (EM) field components – To obtain the maximum output intensity in the 1st diffraction order, simulations that reflect the desired output need to be performed.

(b) Fabricate and etch SW gratings using into the glass and silicon substrates – From the simulation results, SW gratings with specific dimensions have to be fabricated

(c) Use various analytical methods to measure, characterize, and obtain images of the SW gratings – to verify the simulated and fabricated grating dimensions for data comparison.

(d) Chip level assembly and testing of an accelerometer device – The glass and silicon chips have to be assembled to complete the accelerometer device. Configure a testing setup to determine the acceleration displacement from the change output intensity.

1.3 Dissertation Organization

A brief overview of SW gratings and evanescent wave generation followed by processing techniques and characterization of EW coupling for SW gratings is presented in detail.

In Chapter 2 a detailed background study on accelerometers, the current state-of-the-art of other optical accelerometer devices, the theoretical complex electric field where EWs are generated from a single SW grating is presented in detail. Additionally, using a communication theory approach, the EW grating modulation of the two SW gratings is illustrated.

In Chapter 3, EW coupling was simulated using OptiWave™ where the simulation parameters and optimum coupling efficiency from the coupled SW gratings,

and the mechanical characteristics of the spring/proof mass accelerometer membrane are discussed in detail. Also, SW grating fabrication methods are presented, where analysis methods to determine the SW grating dimensions are shown.

Chapter 4 presents in detail the designed masks for the coupled SW grating accelerometer, and the process flow and fabrication of the coupled SW grating MEMS accelerometer is presented.

In Chapter 5, total system signal and noise analysis results are presented. Additionally, the accelerometer test apparatus and physical testing of the coupled SW grating optical MEMS accelerometer is defined. As a force is applied to the sensor, the grating gap is changed, resulting in a related diffraction light intensity. This chapter will present simulated, calculated, and measured values as it relates to determining the acceleration of the device.

Chapter 6 concludes the research work by summarizing the results of the coupled SW grating accelerometer and providing suggestions for future use of this novel sensitive sensing technique.

Chapter 2

Background

2.1 Introduction

The overall objective of this research is to simulate, design, and fabricate a MEMS accelerometer. This section provides an overview of what accelerometers are and the existing MEMS accelerometer types. Also, the sensitivity, noise, and sensing gap parameters of different commercial MEMS accelerometers are highlighted, which are the parameters that the proposed accelerometer will be compared to.

An accelerometer is a device that measures acceleration forces. These forces can be static, like the force of gravity acting on a fixed object, or dynamic. These accelerometers are used for protection in seismic trembles, detection in automobile airbag deployment, and as part of everyday life in our electronic devices and video games. In measuring acceleration, knowing the intended application, desired *g-force* detection, sensitivity, and various other factors are necessary in selecting the proper accelerometer.

There are many types of sensing methods for MEMS accelerometers, which include piezoelectric [6], capacitive [11], piezoresistive [12], tunneling [13], electromagnetic [14], and optical [15], of which capacitive and piezoelectric are the most common. While capacitive and piezoelectric sensing are commonly used, the drawbacks of these techniques include cross-coupling capacitance sensor and temperature sensitivity and power consumption for the piezoresistive sensor [16]. While most accelerometer

sensors today can boast the use of MEMS technology, sharing the advantage of sensor miniaturization, the coupled SW grating MEMS accelerometer sensor proposed in this research has a significant advantage over the other types. While the piezoresistive sensor is easily damaged when dropped, as reported by Li and Shemansky Jr. [17], the proposed coupled SW grating accelerometer has the design flexibility to minimize device failure from shock. Also, the coupled SW grating is completely resistant to electromagnetic interference, which is a drawback of the capacitive accelerometer. A description of the various types of accelerometers and how they measure acceleration is in Table 2-1.

Accelerometers have had tremendous growth in the past twenty years. Measuring seismic activity, navigation systems, and most popular, the automobile industry for air bag deployment and tilt suspension systems are just a few of their applications [18, 19]. Most successfully, in March 2008, Nintendo Inc. achieved a 73 percent increase in net sales and 47.7 percent increase in income from the previous fiscal year with the addition of the accelerometer based Nintendo Wii gaming console controllers [20, 21]. Similarly, net sales of Apple's iPhone and related products and services were $419 million and $1 billion in the third quarter and first nine months of 2008. Similarly, the iPhone handset unit sales totaled 717,000 and 4.7 million during the third quarter and first nine months of 2008, respectively [22]. As the scale of technology continues to get smaller, cutting edge research remains highly competitive and the demand for newer, simpler, and more novel sensors like the proposed EW coupling concept are likely to contribute to this technological advancement. More recently, MEMS company iSuppli Corp. reported MEMS accelerometers and gyroscopes used for e-books and slate tablets like the iPad will bring in $105 million in 2014, compared to only $3 million in 2009 [23].

To measure the gap displacement and gravity force (g-force) acceleration, this research has chosen an optical sensing method for a surface micromachined MEMS accelerometer. This approach aims to demonstrate near field EW coupling using two SW gratings with different grating periods to create a larger effective grating period that will result in propagating diffraction orders into the far field region. Optical modeling of this approach is presented later to obtain the optimum grating thickness, output intensity per change in grating separation, and the optimum coupling efficiency between the variable period SW gratings.

Table 2-1: Accelerometer types and their operation.

Author	**Accelerometer Type**	**Accelerometer Operation**
[13, 24]	Piezoresistive	Has resistive material properties that change under physical pressure, thus changing the internal resistance of the material which is measured
[13]	Tunneling	Induced current change between tunneling tip and electrode, inducing a change in tunneling current and converted into acceleration
[14]	Electromagnetic	Mutual coupling of two planar coils in which the rate of change of current and the distance between the two coils is detected
[6]	Piezoelectric	A piezoelectric material attached to the proof mass, in which an applied force transduces piezoelectric material to a voltage and then to acceleration
[11]	Capacitive	Has a spring and proof mass configuration where gap changes between the two parallel plates capacitors are converted into acceleration
[15]	Optical	Uses a Mach Zender or Michelson Interferometer setup which measures light intensity with a photodiode or light collecting source which is converted to acceleration
[25]	MEMS	MEMS cantilever beam with a proof mass on the end of the beam. Beam deflection is transduced from light intensity to acceleration

Optical sensors are used for various functions which include earthquake/seismic activity detection, displacement detection, acceleration measurement, motion detection, and as transducers. Commonalities of these sensors are their high sensitivity designs and their sensing function shown in Table 2-2. The differences in the various types of optical sensors lie in their sensing function, which directly relates to their sensitivity. There are grating methods, spring and proof mass, waveguide, doubled clamped beams, and Fabry Perot methods that are used for sensing. Currently, there are no published results of EW coupling being used for an accelerometer. Preliminary investigation and calculations shows that the novel coupled SW grating method proposed in this research will prove the sensitivity of this sensor to be comparable to the other highly sensitive optical sensors and has the potential to demonstrate a greater enhanced sensitivity.

Table 2-2: Accelerometer types and their sensing parameters

Author	Sensor Type	Optical type	Sensing Function	Sensitivity
[26]	Optical	µlaser encoder	Seismic Activity	6.4 µg
[27]	Optical	Fiber Bragg grating	Acceleration	2–12.5 µg
[28]	Optical	Spring/proof mass with optical filter	Acceleration	3.3 nm/g
[29]	Optical	Deformable grating	Motion detection	$10\,\mathrm{fm}/\sqrt{\mathrm{Hz}}$ > 1kHz
[30]	Optical	Deformable grating	Sub-Å in plane motion	$0.02\,\mathrm{pm}/\sqrt{\mathrm{Hz}}$
[31]	Optical	Deformable grating	NEMS transducer	$160\,\mathrm{fm}/\sqrt{\mathrm{Hz}}$ at 1Hz
[32]	Optical	Proof mass & Interferometeric	Vibratory acceleration	$40\,\mathrm{ng}/\sqrt{\mathrm{Hz}}$
[33]	Optical	Optical waveguide	Mechanical Resonator Motion	$40\,\mathrm{fm}/\sqrt{\mathrm{Hz}}$
[34]	Optical	Diffraction grating	Acoustic	$2.08\,\mathrm{A}/\sqrt{\mathrm{Hz}}$
[35]	Optical	Diffraction grating	Displacement	$16\,\mu\mathrm{A}/\mathrm{nm}$ at 250 kHz
[30]	Optical	NEMS Beam	Displacement	$0.055\,\mathrm{pm}/\sqrt{\mathrm{Hz}}$
[36]	Optical	Knife Edge	Displacement	$1.0\,\mathrm{pm}/\sqrt{\mathrm{Hz}}$
[15]	Optical	Fabry-Perot	Motion Detection	$100\,\mathrm{nm}/\mathrm{g}$
[37]	Optical	Fiber Bragg grating	Acceleration	$1.0\,\mathrm{mg}/\sqrt{\mathrm{Hz}}$

2.1.1 Subwavelength Gratings

Gratings are optical elements with properties of diffracting light into specific wavelengths. The grating period (grating wavelength) and the wavelength of the illuminating source both determine the direction of the diffracted beams. Diffraction from a grating is visible when the grating period is greater than the wavelength of the illuminating source. This type of diffraction is known as Fraunhofer diffraction. The Fraunhofer diffraction grating equation is used to determine the diffraction angle θ of the higher diffraction orders m where λ is the monochromatic wavelength and Λ is the grating period.

$$m\Lambda = \lambda \cdot \sin(\theta) \rightarrow \theta = \sin^{-1}(m\Lambda/\lambda) \quad (1)$$

There are many types of diffraction gratings: holographic, blazed, concave, sinusoidal, triangular, transmission, and several others which are specified by their geometry, material, efficiency behavior, fabrication type, and their usage [38]. Additionally, these types are classified as either amplitude or phase gratings [38]. There are many complexities in classifying the grating types, wherein amplitude gratings are made by patterning and or etching a material on top of a substrate, thus affecting only the amplitude of the incident source, whereas phase gratings are etched into the substrate and influence the phase of the incident wave.

In the case where the wavelength of the incident monochromatic light is larger than the grating period, there is no real solution for θ in the grating equation and propagating waves are not transmitted in the far field (there is no diffraction). Periodic structures with features smaller than the wavelength of the illuminating light, defined as subwavelength gratings, create a non-propagating electromagnetic field near their surface

called evanescent waves (EWs). These EWs are not detectable by traditional optics because the energy decays exponentially to a negligible level within a micrometer from the grating surface. This diffraction is known as Fresnel diffraction. Although SW gratings do not produce visible waves, the EWs from these structures have been intensely studied and many applications have been reported using the EW field to leverage new optical effects. Some of the applications include high efficiency light emitting diodes [39], transmission color filters [40] and resonant transmission of infra-red [41] and THz radiation [42] for communication. Recently, the propagation and enhanced transmission of EWs using sub-wavelength gratings has gained paramount importance. This stems from the fact that the near-field EWs have been exploited in biosensing [43], guided optics [44], optic fiber couplers [45], apertureless microscopy [46, 47], and nanoelectromechanical devices [30]. It was Keeler, et al. who demonstrated the use of near field optical effects of nanostructured SW gratings for a very sensitive micromachined accelerometer [29].

A MEMS based accelerometer has been envisioned for sensing acceleration using two SW gratings. As previously mentioned, EWs are not detectable by traditional optics. However, if a second periodic structure is brought into close proximity (~ 0.6 μm) to the first grating, re-propagation of the evanescent energy into propagating waves can be accomplished. Importantly, the efficiency of the energy coupling is highly dependent upon the spacing between the gratings. The two SW gratings in close proximity each have different grating periods which creates an effective grating period,

$$1/\Lambda_{eff} = |1/\Lambda_1 - 1/\Lambda_2| \quad (2)$$

where Λ_1 and Λ_2 are the different grating periods, and Λ_{eff} is the effective grating period. When the gratings are far apart propagating waves are not observed, because there is effectively no coupling in the near field region. However, when the gratings are closer together the output intensity of the coupled EWs varies with subtle grating separation changes, making this new coupling method ideal for sub-nanometer displacement detection.

2.2 Theoretical Grating Analysis

2.2.1 Evanescent Wave Generation From a SW Grating

The optical configuration and analysis of a monochromatic plane wave source incident upon a grating is illustrated in the following. A plane wave propagating in the +Z direction incident on an amplitude grating at z = 0 is described as $A_0 \exp(-j(2\pi/\lambda)t$ in the time domain. In the phasor notation, the normally monochromatic plane wave is expressed as

$$E_{0-}(z) = A_0 \exp^{-jkz} \tag{3}$$

where $k=2\pi/\lambda$ (λ is the light wavelength) and $E_{0-}(z)$ is simplified to be A_0 at z=0.

The Fraunhofer diffraction grating equation below is used to determine the diffraction angle θ of the higher diffraction orders m where λ is the monochromatic wavelength and Λ is the grating period.

$$m\Lambda = \lambda \sin(\theta) \rightarrow \theta = \sin^{-1}\left(\frac{m\Lambda}{\lambda}\right) \tag{4}$$

When the wavelength of the incident monochromatic light is larger than the periodic grating wavelength, there is no real solution for θ and propagating waves are not

transmitted in the far field, yet, exponentially decreasing EWs exist in the near field. At z = 0, where the plane wave is incident on the grating, the transmittance function of a sinusoidal amplitude grating is

$$t_1(x) = 1 + b_1 \cos(K_1 x) \tag{5}$$

where b_1 represents the grating modulation depth and grating wave number is K_1 (= $2\pi/\Lambda_1$, Λ_1 is the grating period). The field after the grating, at plane $z = 0^+$ is given by

$$E_{0+}(x) = A_0\left[1 + b_1 \cos(K_1 x)\right] \tag{6}$$

The plane wave spectrum of the field at $z = 0^+$ is represented in the spatial frequency domain and found by taking the inverse Fourier transform of equation (6) [48].

$$P_{0+}(k_x) = \int_{-\infty}^{\infty} E_{0+}(x) \times \exp(jk_x x)\, dx$$

$$= A_0\delta(k_x) + \frac{A_0 b_1}{2}\delta(k_x - K_1) + \frac{A_0 b_1}{2}\delta(k_x + K_1) \tag{7}$$

The resulting inverse Fourier transform in equation (7) represents the total spectrum of the sinusoidal grating propagating in specific directions. The complex exponential function exp ($-jk_z z$) details how plane waves propagate with a wave vector (k_x, k_y, k_z), in which

$$k_z = \pm\left(k^2 - k_x^2\right)^{1/2} \tag{8}$$

[49]. Thus, the propagation of the plane wave spectrum is found to be

$$F_z(k_x) = A_0\delta(k_x) + \frac{A_0 b_1}{2}\delta(k_x - K_1) + \frac{A_0 b_1}{2}\delta(k_x + K_1) \times \exp\left\{\pm jz\left[\left(k^2 - k_x^2\right)^{1/2}\right]\right\} \tag{9}$$

Herein, the complex electric field is determined by taking the Fourier transform of equation (9)

$$\begin{aligned} E_z(x,z) &= \int_{-\infty}^{\infty} F_z(k_x) \times \exp(-jk_x x)\, dk_x \\ &= A_0 \exp(-jkz) + \frac{A_0 b_1}{2} \exp\left[\pm jz\left(k^2 - K_1^2\right)^{1/2}\right] \times \exp(-jK_1 x) \\ &\quad + \frac{A_0 b_1}{2} \exp\left[\pm jz\left(k^2 - K_1^2\right)^{1/2}\right] \times \exp(jK_1 x) \end{aligned} \tag{10}$$

For the case of $\Lambda_1 < \lambda$ ($K_1 > k$), choosing the negative solution of equation (8), which allows only the solution with a decaying real exponential, equation (10) can be re-written as:

$$\begin{aligned} E_z(x,z) &= \int_{-\infty}^{\infty} F_z(k_x) \times \exp(-jk_x x)\, dk_x \\ &= A_0 \exp(-jkz) + \frac{A_0 b_1}{2} \exp\left[-z\left(K_1^2 - k^2\right)^{1/2}\right] \times \exp(-jK_1 x) \\ &\quad + \frac{A_0 b_1}{2} \exp\left[-z\left(K_1^2 - k^2\right)^{1/2}\right] \times \exp(jK_1 x) \end{aligned} \tag{11}$$

This describes waves propagating parallel to the grating substrate in the ±x direction with wavenumber K_1 and exponentially decay in the z-direction [48].

2.2.2 EW Coupling From Two Different Period SW Gratings

The plane wave analysis shown in the previous section derived the evanescent wave properties for the case of a single SW grating where $\Lambda_1 < \lambda$. Now, we present further analysis for two coupled SW gratings with different grating periods, Λ_1 and Λ_2. Similar to equation (5), the transmittance function of the second SW grating is

$$t_2(x) = 1 + b_2 \cos(K_2 x) \tag{12}$$

where b_2 represents the second grating modulation depth and K_2 represents the second grating wave number ($2\pi/\Lambda_2$, where Λ_2 is the second grating period). Equation (13) is the plane wave spectrum of the field at $z = 0^{++}$ found by multiplying equation (3) by equation (12) and taking the inverse Fourier transform.

$$P_{0++}(k_x) = \int_{-\infty}^{\infty} \left[E_{0+}(x) \times t_2(x) \right] \times \exp(jk_x x)\,dx$$

$$= A_0\delta(k_x) + \frac{A_0 b_1}{2}\left[\delta(k_x - K_1) + \delta(k_x + K_1)\right] + \frac{A_0 b_2}{2}\left[\delta(k_x - K_2) + \delta(k_x + K_2)\right]$$

$$+ \frac{A_0 b_1 b_2}{4}\left\{\delta\left[k_x - (K_1 + K_2)\right] + \delta\left[k_x + (K_1 + K_2)\right] + \delta\left[k_x - (K_1 - K_2)\right] + \delta\left[k_x + (K_1 - K_2)\right]\right\} \quad (13)$$

By multiplying equation (13) by the free space propagator, $\exp(-jk_z z)$, where $k_z = \pm\text{sqrt}(k^2 - k_x^2)$, computing for the EM fields at plane z, and by taking the Fourier transform, the propagation of the plane wave spectrum is found to be

$$E_z(x,z) = \int P_{0++}(k_x) \times \exp(-jk_x x)\,dk_x$$

$$= A_0\left[\exp(-jzk_z)\right] + \frac{A_0 b_1}{2}\begin{bmatrix} \exp(jxK_1)\times\exp\left[\pm jz\left(k^2 - K_1^2\right)^{1/2}\right] \\ +\exp(-jxK_1)\times\exp\left[-jz \pm \left(k^2 - K_1^2\right)^{1/2}\right] \end{bmatrix}$$

$$+ \frac{A_0 b_2}{2}\begin{bmatrix} \exp(jxK_2)\times\exp\left[\pm jz\left(k^2 - K_2^2\right)^{1/2}\right] \\ +\exp(-jxK_2)\times\exp\left[-jz \pm \left(k^2 - K_2^2\right)^{1/2}\right] \end{bmatrix}$$

$$+ \frac{A_0 b_1 b_2}{4}\begin{bmatrix} \exp\left[jx(K_1 + K_2)\right]\times\exp\left\{\pm jz\left[k^2 - (K_1 + K_2)^2\right]^{1/2}\right\} \\ +\exp\left[-jx(K_1 + K_2)\right]\times\exp\left\{\pm jz\left[k^2 - (K_1 + K_2)^2\right]^{1/2}\right\} \\ +\exp\left[jx(K_1 - K_2)\right]\times\exp\left\{\pm jz\left[k^2 - (K_1 - K_2)^2\right]^{1/2}\right\} \\ +\exp\left[-jx(K_1 - K_2)\right]\times\exp\left\{\pm jz\left[k^2 - (-K_1 + K_2)^2\right]^{1/2}\right\} \end{bmatrix} \quad (14)$$

For the case where $| K_1 - K_2 | < k$, $K_1 > k$, and $K_2 > k$ only the first term and the last terms of equation (14) denote propagating waves in the z, the last two terms are estimated to be the diffracted waves from a the two coupled SW gratings. The other terms denote evanescently decreasing waves in the z direction. The next section will use a model from communication theory to illustrate the EW coupling of the two period SW gratings.

2.2.3 EW Coupling by the Communication Theory Approach

When we take the continuous Fourier transform of a signal wave grating, the grating may be represented by the decomposition into a summation of sine and cosine gratings. For a sinusoidal signal, we obtain two unit delta functions in the spatial frequency domain at the frequency of the sinusoidal grating. The two SW gratings (K_1, K_2) with different grating periods are represented in the spatial frequency domain by two different impulse functions as shown in Figure 2-1 (a, b). When the convolution of the spatial frequency components K_1 and K_2 are taken, frequency components at $(-K_1-K_2)$, $(-K_1)$, $(-K_2)$, $(-K_1+K_2)$, (0), (K_1-K_2), (K_2), (K_1), and (K_1+K_2) are produced. These components are identical to those in the plane wave spectrum of the field in equation (14). Using the model from communication theory, a low pass filter (LPF) is denoted by the bounded box in Figure 2-1 (b) which filters spatial frequencies outside the region. The spatial frequencies $(-K_1+K_2)$ and (K_1-K_2) may be allowed within the LPF region and propagates in free space as illustrated in Figure 2-1 (c). When the two grating periods are each sub-wavelength, real propagating diffraction angles can be produced by a pair of such gratings using this method.

The convolution of the two gratings in the spatial domain is the physical coupling of the two gratings, placing them in close proximity. The image in Figure 2-1 (a) shows

the concept of the coupled gratings as they are directly on top of each other. The unit delta functions of the two SW gratings shown in Figure 2-1 (b) are convolved and the different K_1 and K_2 spatial frequency components are seen in Figure 2-1 (c). Also, the magnitude shown above the delta function components are scaled proportional to the scaling in equation (14). These represent the output intensity of the coupled EWs. The analytical and visual representation through communication theory of EW coupling conceptually shows that this is a plausible technique for the envisioned MEMS accelerometer. To further support the claim of EW coupling and determine the effects of varied grating thicknesses and spacing, finite difference time domain (FDTD) [50] based simulation results will be presented to in the next section.

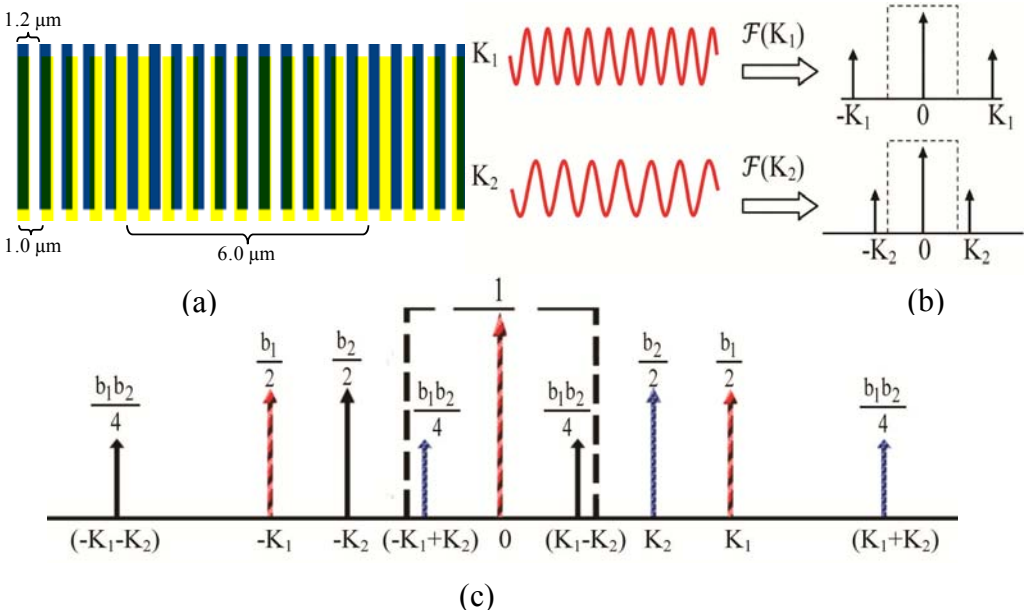

Figure 2-1: (a) Coupled gratings drawn to scale (blue-1.2 µm, yellow-1.0 µm) illustrating the 6.0 µm effective grating (b) Two sinusoidal gratings (K1 and K2) in the time domain and their Fourier transform spatial frequency components surrounded by the LPF region (c) Convolved frequency domain of grating-modulated waves showing coupling (-K1+K2 and K1-K2) in the LPF region

Chapter 3

Optical and Mechanical Simulation of Accelerometer Components

3.1 Background Finite Difference Time Domain (FDTD)

Optical simulation of the SW gratings was carried out using OptiWave™ software package based on finite difference time domain (FDTD) numerical modeling approach. The FDTD approach is based on solving the time-dependent Maxwell's curl equations where space and time steps relate to the accuracy, numerical dispersion, and the stability of the FDTD method [50]. In the case of 2D FDTD equations, the optical layout is in the X-Z plane, where Y is assumed to be infinite, Z is the propagating direction and the Maxwell $\partial/\partial y$ derivatives are removed which separates the equations into two sets, transverse electric (TE) and transverse magnetic (TM). For these simulations and their results, 2D TE waves are used. As a result, the Maxwell equations become:

$$\frac{\partial E_y}{\partial t} = \frac{1}{\varepsilon}\left(\frac{\partial H_x}{\partial z} - \frac{\partial H_z}{\partial x}\right), \qquad \frac{\partial H_x}{\partial t} = \frac{1}{\mu_0}\frac{\partial E_y}{\partial z}, \qquad \frac{\partial H_z}{\partial t} = \frac{1}{\mu_0}\frac{\partial E_y}{\partial x} \tag{15}$$

where $\varepsilon = \varepsilon_0 \varepsilon_r$ is the dielectric permittivity and μ_0 is the magnetic permeability of the vacuum, and $n = \sqrt{\varepsilon_r}$ is the refractive index.

The image in Figure 3-1 (b) is the interface the OptiWave™ software uses to complete mesh size and time parameter simulations. In the time parameters section, there

is time step size and total simulation steps, both of which are directly related to and contribute to the computation of the 2D mesh size. The fields in eq. (15) are represented by a 2D array, $E_y(i,k)$, $H_x(i,k)$, and $H_z(i,k)$, where i and k are the space steps in their respective x and z directions. This 2D array schematic in Figure 3-1 (a) is an illustration of a space grid and time-stepping algorithm investigated by Kane Yee [49]. The solid lines denote a particular mesh size, whereas, the dashed lines form the FDTD cells. The H_x field is associated with coordinates (i, k + 0.5) and the H_z field with (i + 0.5, k) which are both correlated to cell edges; whereas, E_y is the center of the FDTD space cell [49].

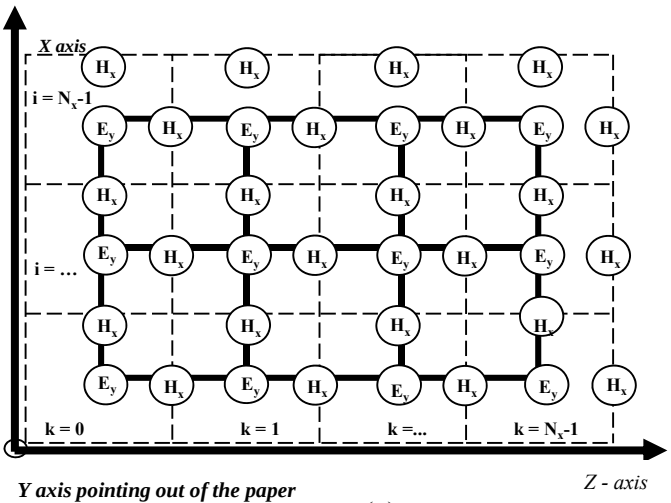

(a)

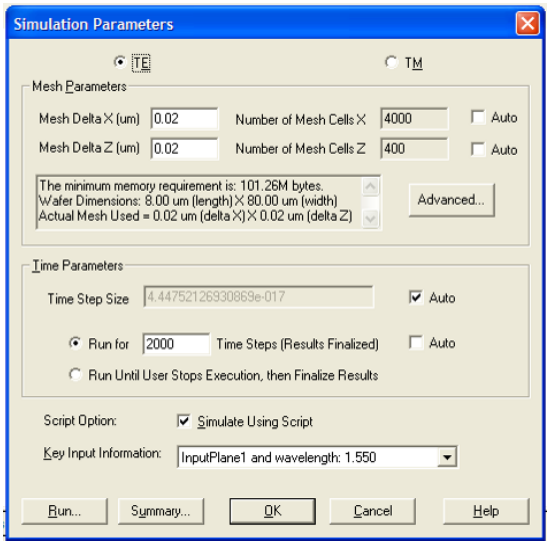

(b)

Figure 3-1: (a) Yee's 2D Lattice [49] (b) OptiFDTD Simulation Parameters

Implementing the electric and magnetic fields with their corresponding coordinate space steps, the 2D numerical discretization of eq. (16) becomes:

$$\frac{E_y^{\,n}(i,k)-E_y^{\,n-1}(i,k)}{\Delta t}=\frac{1}{\varepsilon}\frac{H_x^{\,n-0.5}(i,k+0.5)-H_x^{\,n-0.5}(i,k-0.5)}{\Delta z}-\frac{1}{\varepsilon}\frac{H_z^{\,n-0.5}(i+0.5,k)-H_z^{\,n-0.5}(i-0.5,k)}{\Delta x} \qquad (16)$$

This is developed into the following finite difference equations:

$$E_y^{\,n}(i,k)=E_y^{\,n-1}(i,k)+\frac{\Delta t}{\varepsilon\,\Delta z}\left[H_x^{\,n-0.5}(i,k+0.5)-H_x^{\,n-0.5}(i,k-0.5)\right]-$$

$$\frac{\Delta t}{\varepsilon \Delta x}\left[H_z{}^{n-0.5}\left(i+0.5,k\right) - H_z{}^{n-0.5}\left(i-0.5,k\right)\right]$$

$$H_x{}^{n+0.5}\left(i,k+0.5\right) = H_x{}^{n-0.5}\left(i,k+0.5\right) + \frac{\Delta t}{\mu_0 \Delta z}\left[E_y{}^{n}\left(i,k+1\right) - E_y{}^{n}\left(i,k\right)\right]$$

$$H_z{}^{n+0.5}\left(i+0.5,k\right) = H_x{}^{n-0.5}\left(i+0.5,k\right) - \frac{\Delta t}{\mu_0 \Delta z}\left[E_y{}^{n}\left(i+1,k\right) - E_y{}^{n}\left(i,k\right)\right] \quad (17)$$

The time steps in eq. (17) are denoted by *n*, where *i* and *k* coordinates represent the space steps, and Δx and Δz are along the *X* and *Z* axis respectively.

The FDTD parameter that requires careful attention is the time and space step size. The proposed minimum mesh size is:

$$\text{minimum } (\Delta x, \Delta z) = \lambda_{min}/10 \cdot n_{max} \quad (18)$$

where λ_{min} is the incident wavelength and n_{max} is the maximum refractive index of the material λ_{min} propagates through. The time step was chosen according to the Courant-Friedrichs-Levy (CFL) condition:

$$\Delta t \leq \frac{1}{v\sqrt{\frac{1}{(\Delta x)^2} + \frac{1}{(\Delta z)^2}}} \quad (19)$$

where *v* is the speed of light in the medium. The CFL condition is a convergent algorithmic method for solving partial differential equations to ensure numerical stability of the algorithm [51]. The software calculates the automatic time step as well as the overall time steps including finalization. Also, the software reserves the right to manually change the total number of simulated time steps which is extremely critical to obtaining an accurate output. The simulation has to have ample time to fully propagate

through the system to be detected in the output far field region. Improperly defining this value will result in inaccurate data.

3.2 OptiWave™ FDTD Simulation Modeling

3.2.1 Simulation Parameter Optimization

Evanescent wave coupling was simulated using the OptiWave™ FDTD software. The simulations performed using this software were performed to determine the grating parameters which produce the maximum output intensity and to determine the grating coupling efficiency with respect to the grating separation. However, there are several parameters that have to be optimized before running a parametric simulation. For example, the wave shape, grid size, step size, and grating dimensions contribute to maximizing the output coupling efficiency and simulation accuracy. In addition to the output coupling efficiency, signal to noise ratio (SNR), grating sensor sensitivity, and other signal-related characteristics can be calculated.

Several parameters were simulated prior to the coupled SW grating simulation. The simulations performed ranged from varying the incident wave type, the input boundary layer conditions, the full wave half at maximum (FWHM) laser beam radii, and the X and Z mesh simulation grid in different mediums (i.e. air, glass, and silicon). Performing simulations with these parameters will have an effect on the output intensity, the reflectivity and absorption within the model, interaction with the grating elements, and simulation process time. After optimizing these parameters, the coupled SW grating concept is then designed, processed, analyzed, and interpreted using the OptiWave™ software. The grating design layout is shown in Figure 3-3.

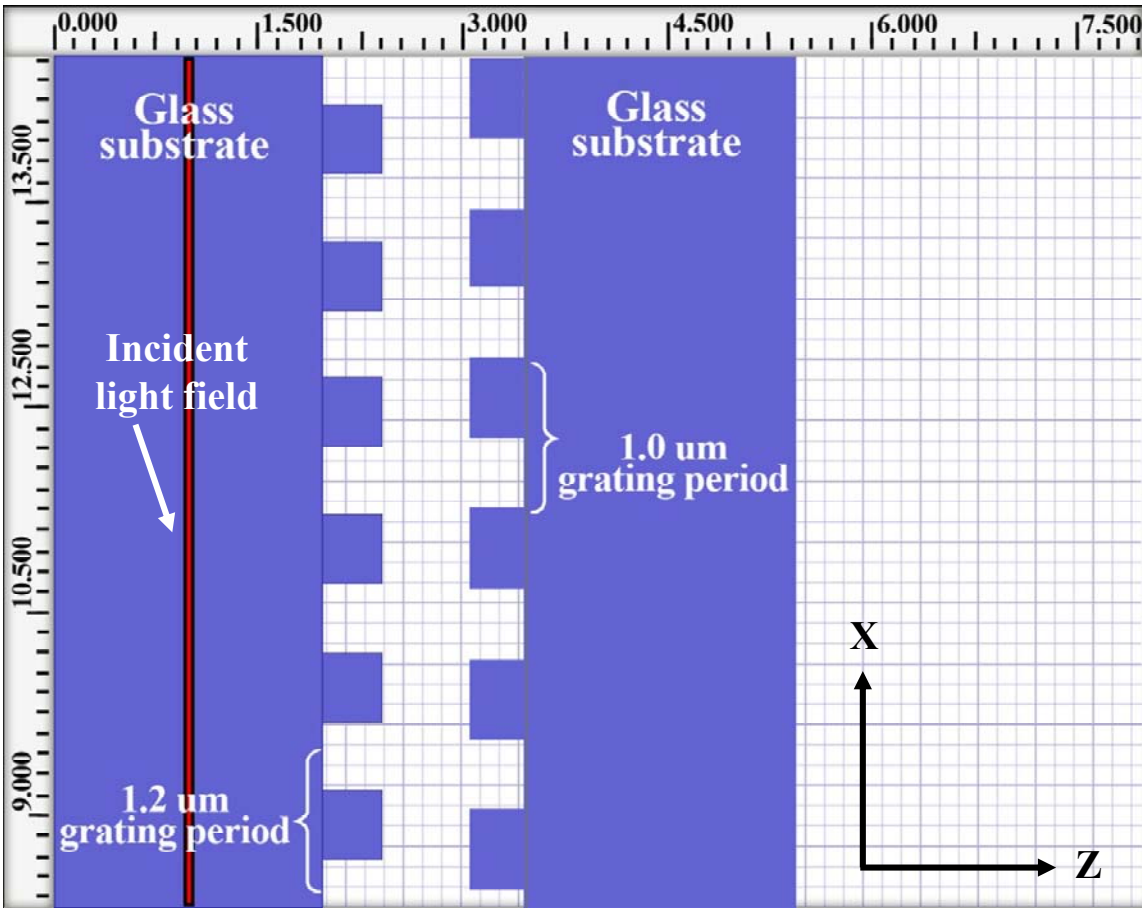

Figure 3-2: OptiFDTD designer layout used to design the coupled SW gratings

In the forthcoming simulations, the procedure for obtaining the output results are as follows: 1) the grating design layout is entered 2) the incident light wave is launched in the gratings 3) the electromagnetic (EM) field evanescently couples and propagates to the output plane 4) the simulation solves Maxwell's curl equations and computes the far field diffraction. The first simulation performed was to compare the input wave field of a Gaussian beam with a 10 μm full width half maximum (FWHM) beam versus a rectangular (RECT) beam with a 10 μm FWHM beam. The simulation was performed under the following conditions: 80 x 8 μm simulation window; 1.550 μm infrared (IR) laser; glass substrate; 6.0 μm period x 0.6 μm thick grating in glass (n=1.57); simulation

grid (0.06 µm); and 750 iteration step size. The simulation in Figure 3-3 clearly illustrates the Gaussian wave is the favored over the RECT wave type. The first diffraction order at ~15° is seen with the Gaussian wave, however, it is unclear where the first diffraction order is for the RECT wave. This diffraction angle accurately corresponds to equation (1), where $\theta = \sin^{-1}(m\Lambda/\lambda)$, which equals 14.97°. It can be concluded that there is better grating efficiency from the grating element when the incident beam is a Gaussian wave source.

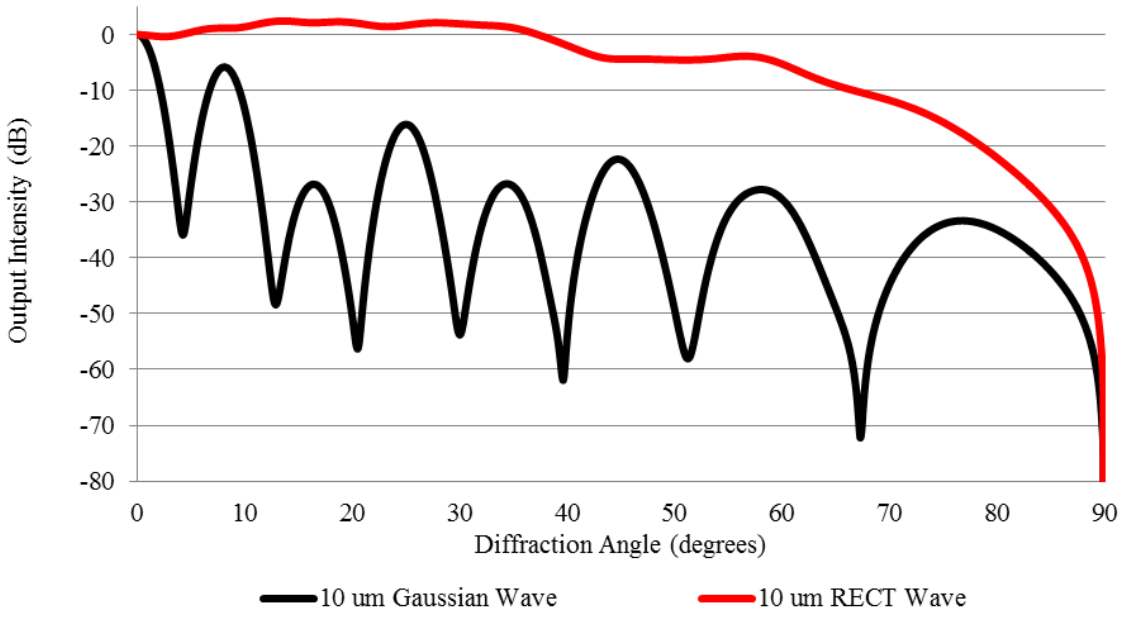

Figure 3-3: OptiFDTD 2D output comparing the RECT wave versus the Gaussian wave

In the next simulation, the Gaussian FWHM beam width was varied from 10 µm, to 15 µm, to 20 µm, to 100 µm. The simulation was performed under the same conditions as before: 80 x 8 µm simulation window; 1.550 µm infrared (IR) laser; glass substrate; 6.0 µm period x 0.6 µm thick grating in glass (n=1.57); simulation grid (0.06

µm); and 750 iteration step size. While the beam widths exhibit similar output intensity, the graphs of the beam widths in Figure 3-4 shows that the 10 µm width gradually decays, in which there could be an overlap of the higher diffraction orders. The 15 µm, 20 µm, and 100 µm beam widths showed ringing effects (similar to the ringing of a sinc function) between the higher diffraction orders. These effects for the 100 µm beam width were too close to the 1st diffraction order at -15 dB, when compared to -40 dB and -30 dB of the 15 µm and 20 µm beam widths respectively. This is likely a result of the simulation window (80 x 8 µm) being smaller than the 100 µm beam width. Using the calculations of the expected physical beam width of the commercial IR laser and optics pair, the 100 µm was excluded and the 20 µm beam width was selected.

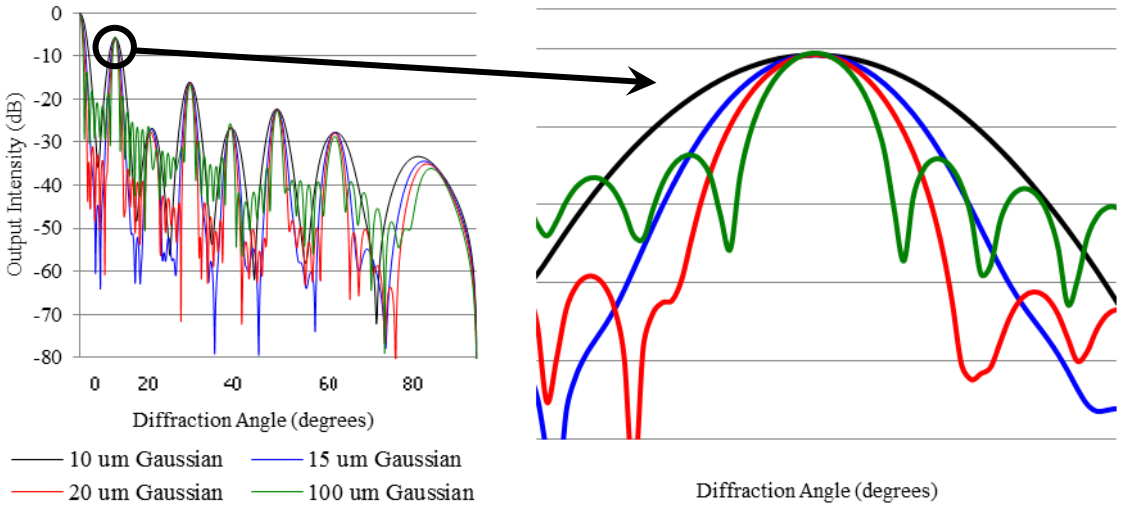

Figure 3-4: OptiFDTD 2D output intensity comparison of 10 µm, 15 µm, 20 µm, and 100 µm FWHM beam widths

The next simulation varied the X and Z mesh delta (grid size) and the number of simulation steps. In Figure 3-5, the grid size was varied from 0.06 µm, 0.04 µm to 0.02

µm, where it was observed that the output intensity was suppressed between the diffraction orders. This suppression between the diffraction orders distinguished between noise and higher diffraction orders. As Yee's 2D lattice explained [49], the trade off with reducing the mesh size doubles the on the Δt simulation time and the computing storage space necessary to store and analyze the data.

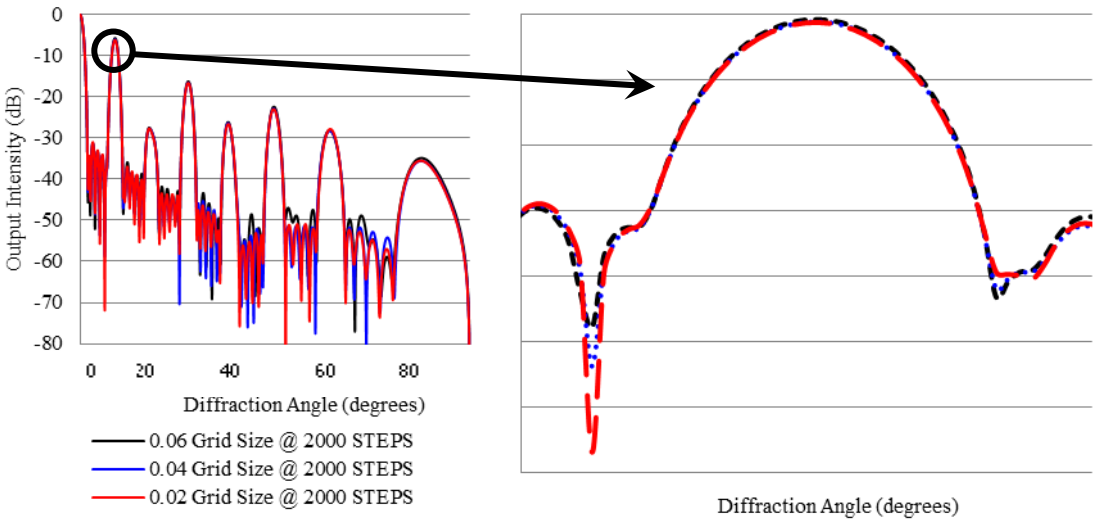

Figure 3-5: OptiFDTD 2D output intensity comparing 0.06 µm, 0.04 µm, and 0.02 µm grid sizes

These results had a significant impact on the simulation computing, where the default simulation iteration step size changed from 8.966E-17 seconds to 4.44E-17 seconds, and the file size increased fourfold from 31 megabytes (MB) to 120 MB.

The next simulation varied the iteration step size from 2000, 1000, 750, and 500 steps in Figure 3-6, where more iteration steps equates to a larger file size and more

suppressed noise. Although there is an increase in space (computer storage) and time, it is a tolerable tradeoff to obtaining more accurate simulation results.

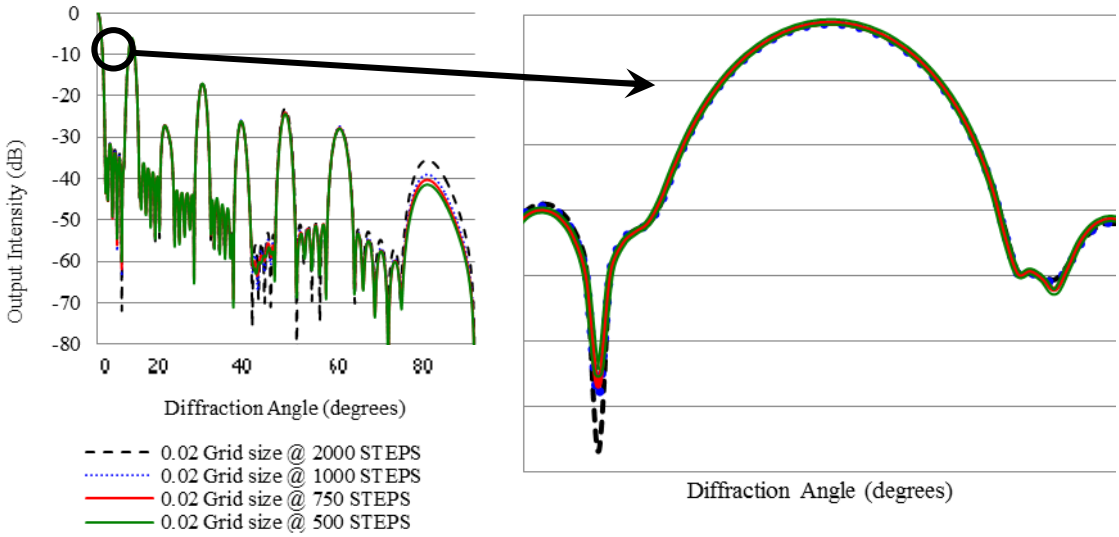

Figure 3-6: OptiFDTD 2D output intensity comparing 2000, 100, 750, and 500 steps with a 0.02 µm grid size

The last of the optimization simulations varied the boundary layer conditions. In comparison to the previous simulations, having obtained optimal simulation parameters, the simulation was performed under the following conditions: 80 x 8 µm simulation window; 1.550 µm infrared (IR) laser, 20 µm FWHM Gaussian diameter; glass substrate; 6.0 µm period x 0.6 µm thick grating in glass (n=1.57); simulation grid (0.02 µm); and 2000 iteration step size. In the OptiFDTD software there are four types of boundary conditions, Anisotropic Perfectly Matched Layer (APML), Perfect Magnetic Conductor (PMC), Perfect Electrical Conductor (PEC), and the Periodic Boundary Condition (PBC). Although the PMC and PEC boundary condition parameters do not meet the device design criteria (being neither perfectly magnetic nor electric), they were simulated and compared along with the APML and PBC boundary layers in Figure 3-7. Also, perfectly

matched layers, in their original form, only attenuate propagating waves; purely evanescent waves oscillate in the PML but do not decay more quickly [50].

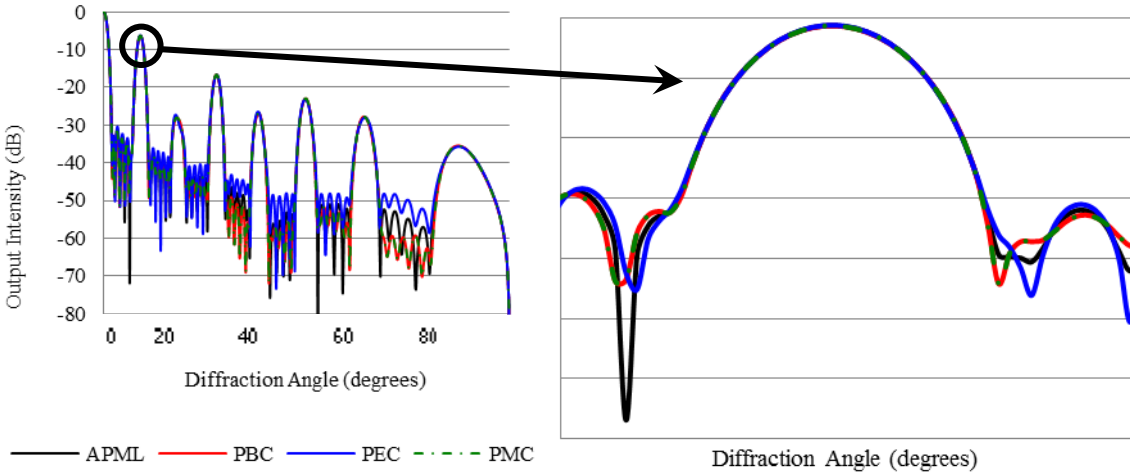

Figure 3-7: OptiFDTD 2D output intensity comparing APML, PBC, PEC, and PML boundary conditions

From the results in Figure 3-7, the curves are very similar; the PBC and PMC boundary conditions are identical, and because the PMC condition does not apply to this model it is not selected as the best model. It was already stated that the PEC condition is not applicable, so the APML layer was selected. Furthermore, the AMPL condition suppressed noise -20 dB more than the other conditions. This clearly distinguishes between the noise region and the first diffraction order where the output intensity is measured. The simulations for software optimization resulted in using the following conditions: a Gaussian input wave; FWHM beam width of 20 μm; 0.02 μm grid size; an iteration step size of 2000; and an AMPL boundary condition.

3.2.2 SW Grating Dimension Optimization and EW Coupling

The envisioned MEMS accelerometer will have 1.2 μm and 1.0 μm gratings etched in glass and silicon respectively. With the 1.55 μm infrared laser incident on a single 1.2 μm or 1.0μm SW grating, no diffraction orders are observed; but, when coupled together this grating pair has an effective grating period of 6.0 μm_{eff} from equation (2). The optimal grating thickness (etch depth) for maximum output intensity of both substrates is unknown, wherein, simulations varying the grating thickness of both gratings in glass and silicon, and the grating separation were performed to achieve the maximum output intensity.

To determine the optimum grating thickness for maximum coupling efficiency in glass, simulation of 1.2 μm and 1.0 μm SW gratings in glass (n = 1.57) were performed. The grating separation between the gratings were kept fixed at 0.3 μm, while the grating thickness of the 1.2 μm and 1.0 μm SW gratings was varied from 0.1 μm to 1.0 μm in 0.1 μm increments. The 0.3 μm grating separation was based on the envisioned accelerometer design, in which the design would need a separation between the two gratings to detect a change in the output intensity, as applied forces affect the gap. In Figure 3-8 (a-d), the simulation layout of the coupled SW gratings in glass are shown and the output intensity results. From the initial simulation results, it was determined that the maximum output intensity was between 0.2 μm and 0.3 μm, so the simulation was modified to 0.01 μm increments. The results showed that the maximum output intensity occurred when the gratings in glass were 0.21 μm with the output intensity measuring -7.5 dB. Also, we see in Figure 3-8 (d) that the output intensity increases and decreases (more or less EW coupling) at different grating thicknesses.

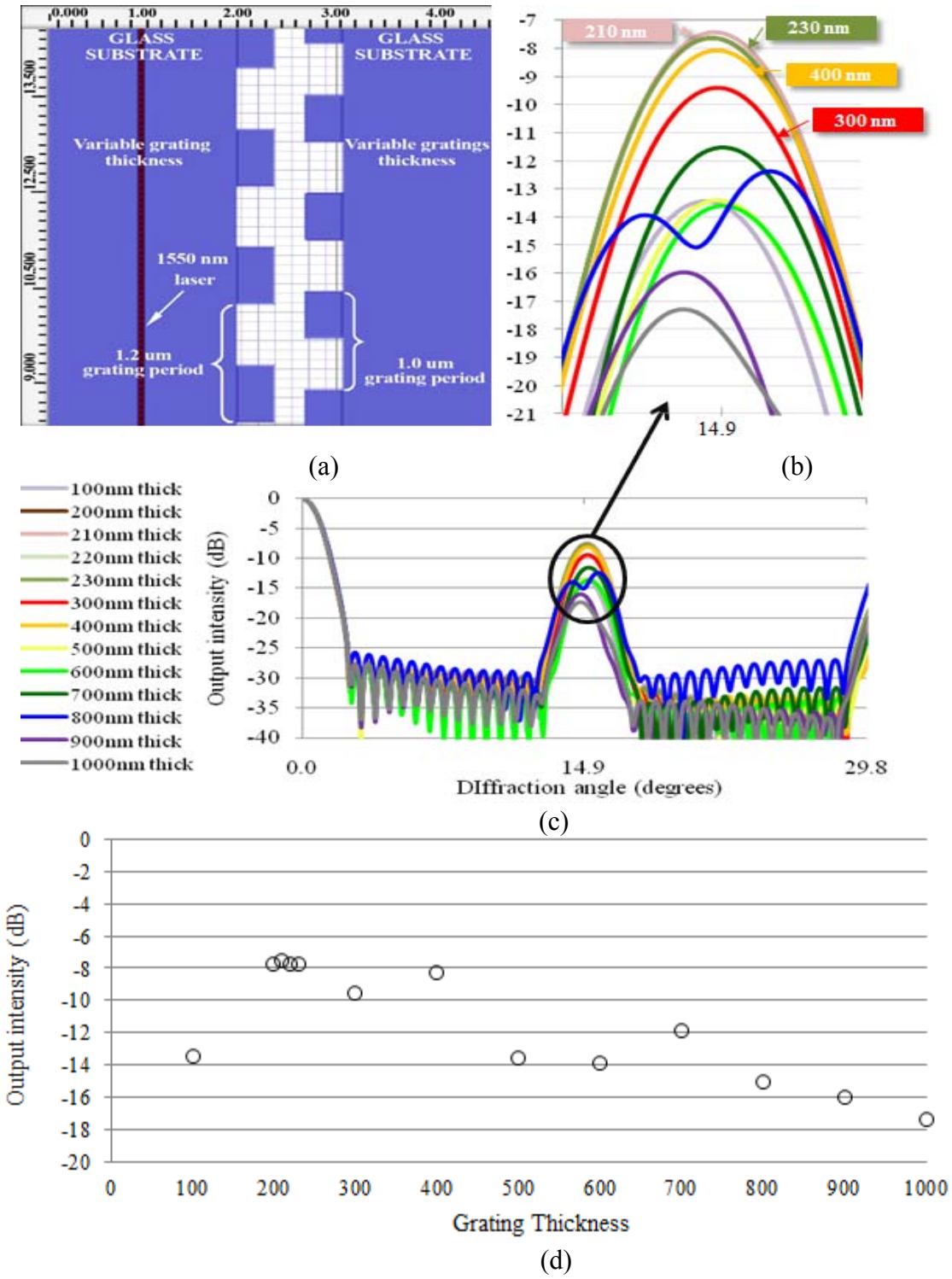

Figure 3-8: Optimal thickness results from 1.2 and 1.0 SW gratings in glass (a) Simulation layout of variable grating thickness in glass (b-c) magnified and normal view of the output intensity vs. diffraction angle (d) output intensity vs. grating thickness

The next simulation uses the optimum grating thickness in glass from the previous simulation and it is used to determine the optimum grating thickness for the silicon substrate (n = 3.48). The grating separation was fixed at 0.3 μm and the grating thickness was varied from 0.1 μm to 1.0 μm in 0.1 μm increments. The output intensity of the coupled gratings is shown in Figure 3-9 (a-d) where maximum output intensity occurs when the gratings were between are 0.4 μm and 0.5 μm thick. The simulation was again modified to 0.01 μm increments, where the output intensity measured -5.7 dB for 0.41 μm, 0.42 μm, and 0.43 μm thick gratings. The 0.42 μm grating period was chosen since the output intensity was identical with the others.

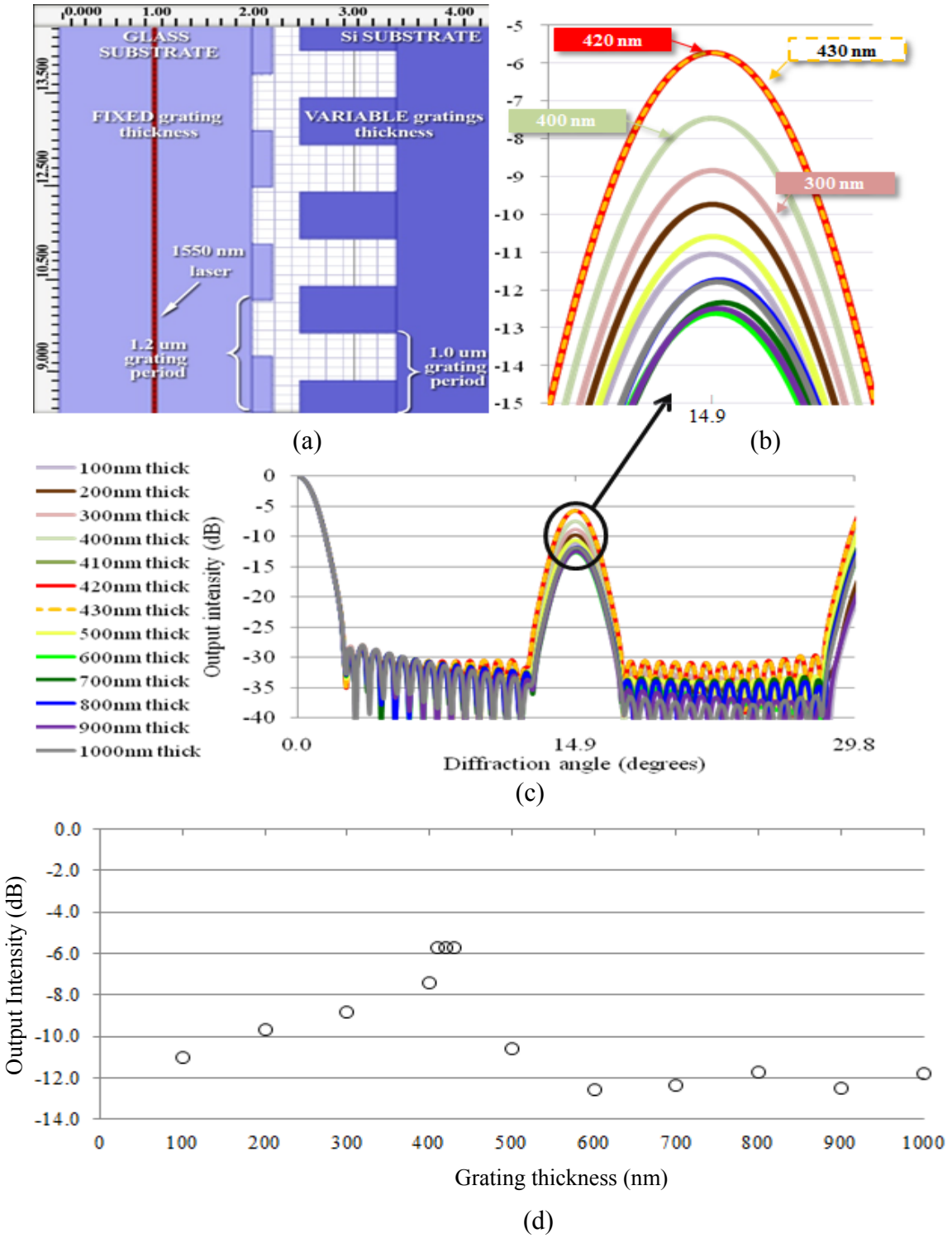

Figure 3-9: Fixed glass grating thickness coupled with variable grating thickness in Si (a) Simulation layout of fixed glass and variable grating thickness in silicon (b-c) magnified and normal view of the output intensity vs. diffraction angle (d) output intensity vs. grating thickness

With the optimum grating thicknesses for glass and silicon established, the next simulation will be modeled to reflect the envisioned MEMS accelerometer device, using a 1.2 μm period grating, 0.21 μm thick in glass and a 1.0 μm period grating, 0.42 μm thick in silicon. In this simulation, the grating thicknesses are fixed (obtained from the previous simulations) and the grating separation is varied from 0.1 μm to 1.0 μm in 0.1 μm increments. The grating separation represents the area where the EW energy couples. Using the 1.55 μm IR laser incident on the SW grating structure, as the two gratings are brought closer together, EW coupling occurs and an increase in the output intensity is observed. In Chapter 5, this is correlated to the acceleration and displacement of the spring/proof membrane of the accelerometer.

Understanding the exponentially decaying properties of EWs, when the gratings are not close enough, EW coupling is minimal and sometimes nonexistent. When the gratings have a 0 μm grating separation (as if they were touching) the output intensity is at the maximum. However, this is not a feasible position for the gratings, as the accelerometer would be unable to move. Therefore, the grating separation was varied from 0.1 μm to 1.0 μm in 0.1 μm increments. This allows the output intensity of the accelerometer to be monitored at nanometer displacement. It can be seen in Figure 3-10 that the output intensity increases as the grating separation decreases. These simulation results provide the grating dimensions needed to achieve maximum output intensity and for fabrication of the SW gratings for the coupled SW grating MEMS accelerometer. Also, a single 1.0 μm SW grating is shown on the graph in Figure 3-10 to show the exponentially decreasing properties of a single SW grating and to clearly define the evanescent field region.

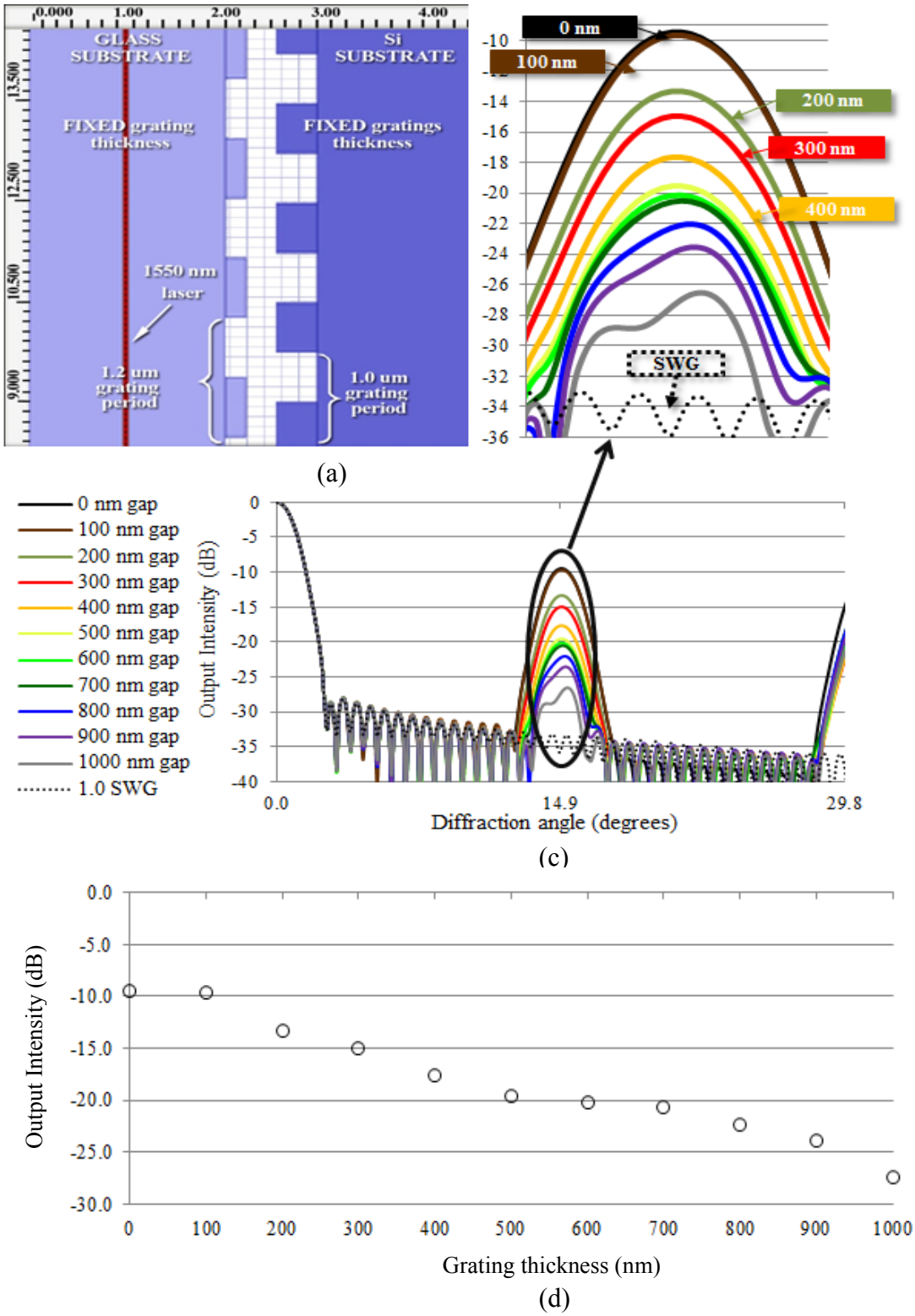

Figure 3-10: Optimized grating thickness in glass and Si a) Simulation layout of fixed grating thickness in both glass and Si (b-c) magnified and normal view of the output intensity vs. diffraction angle (d) output intensity vs. grating thickness

The finite difference time domain optical modeling results presented in this section has provided a better understanding of evanescent wave coupling using different period SW gratings. The simulations performed were designed to optimize EW coupling, resulting in maximum output intensity between the two different period SW gratings. The final simulation demonstrated the strength of the EW coupling concept. The output intensity of the effective grating period (Λ_{eff}) of the coupled SW grating pair displayed a decrease in output intensity as the gap separation increased. Furthermore, we were able to identify the evanescent field from the no-propagating waves from the purely SW 1.0 μm grating. With the simulations complete, validating the EW coupling concept, actual grating fabrication of SW gratings in glass and silicon will be demonstrated.

3.3 Accelerometer Spring Force Design and Analysis

In this section, we will present an overview of meander tether parameters (serpentine spring) for the designed accelerometer. The serpentine spring design parameters and structural analysis are compared using analytical calculations, finite element modeling simulations (Coventorware), and measured data. The aforementioned parameters include spring deflection, spring constant force, and the physical spring dimensions.

The challenges that exist in designing MEMS devices with movable components vary. These challenges arise from being designed differently, being subject to different processing conditions, varying the material characteristics, etc. The commonly used spring types that are used in MEMS devices, as seen in Figure 3-11, are fixed-fixed, folded flexure, u-style, crab-leg, and serpentine-type spring structures [52-56]. While all of these spring styles have favorable advantages for specific applications, they also have

their drawbacks, like extremely high spring constants, minimal beam lengths and widths, and spring thickness restrictions [56]. However, designing a spring with a low spring constant, which limits cross-axis sensitivity motion in the vertical and lateral directions, the serpentine spring style was chosen for our design [57].

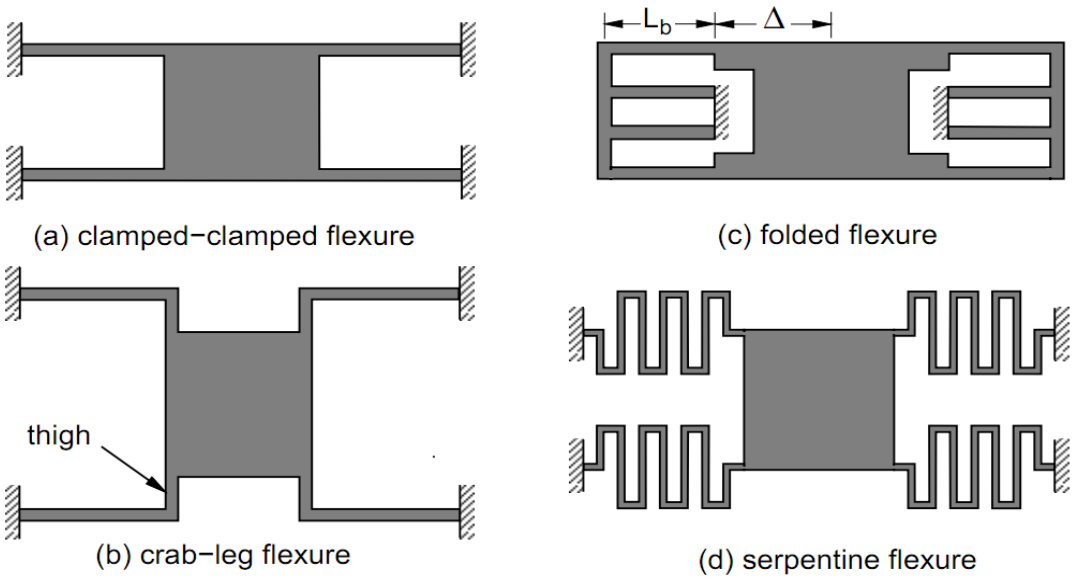

Figure 3-11: Various spring designs (a) fixed-fixed flexure (b) crab-leg flexure (c) folded flexure (d) serpentine flexure [56]

In the design presented in this research, we began with structural analysis of the spring stiffness constant, where the geometrical dimensions of the springs (length, width, and thickness), along with the material properties of the substrate (Si) both are contributing factors in determining the stiffness constant of the designed springs. Additionally, the stiffness constant is an essential parameter in determining the sensitivity of the spring structure.

3.3.1 Numerical Analysis of Serpentine Spring Structures

The initial method for designing the spring model in this research was to obtain the spring constant stiffness by using the equations in the lumped-parameter stiffness modeling matrix. This stiffness matrix has been extensively investigated, where analytical models for each stiffness constant has been derived for fixed-fixed, crab-leg, folded, and serpentine flexures [56]. Therefore, to solve the analytical equations, the stiffness constant was determined by changing the physical dimensions (beam lengths *a* and *b*, width *w*, and thickness *t*) of the spring, which can be seen in Figure 3-12.

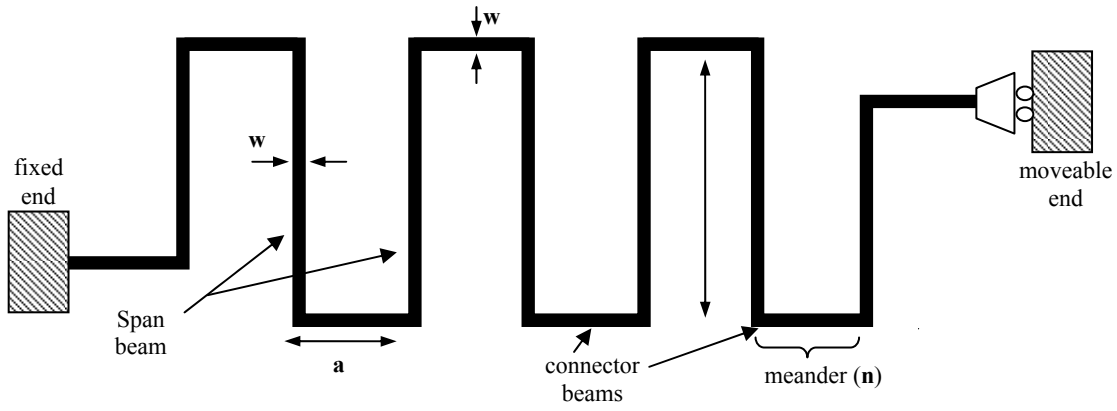

Figure 3-12: Serpentine spring schematic [56]

The advantage in using an analytical approach to solve the stiffness constant allows the designer to approximate stiffness constant value before modeling, fabrication, and testing the structure design.

The envisioned accelerometer design will have one-axis of motion in the *Z*-direction, in which the *X* and *Y* axis are constrained to zero. As previously mentioned, the stiffness constant has been formerly derived, whereto; for *n* even, $k_z = 4F_z/\delta_z$,

where F_z and δ_z is the applied force and displacement in the z-direction, is used to determine the spring constant stiffness in the *Z-axis* in equation (20) [56] as,

$$k_z = \frac{48 \cdot S_{ea} S_{eb} S_{ga} S_{gb}}{\left\{ \begin{array}{l} S_{eb} S_{ga} a^2 \left(S_{gb} a + S_{ea} b \right) n^3 - 3 S_{ea} S_{eb} S_{ga} a^2 b n^2 + \\ S_{ea} b \left(2 S_{eb} S_{ga} a^2 + 3 S_{eb} S_{gb} ab + S_{ga} S_{gb} b^2 \right) n - S_{ea} S_{ga} S_{gb} b^3 \end{array} \right\}} \tag{20}$$

where, $S_{ea} \equiv EI_{x,a}$, $S_{eb} \equiv EI_{x,b}$, $S_{ga} \equiv GJ_a$, $S_{gb} \equiv GJ_b$,. The product EI_x is called the flexural rigidity of the beam, where E is the Young's modulus of Si and the bending moment of inertia (I) is

$$I_x = \frac{\mathrm{t}^3 \mathrm{w}}{12} \tag{21}$$

The torsion modulus of elasticity (G) is correlated to the Young's modulus and Poisson's ratio by

$$G = \frac{E}{2(1+v)} \tag{22}$$

Cho and Pisano [58] illustrated the torsion constant (J) for a beam with rectangular cross-section to be

$$J = \tfrac{1}{3} t^3 w \left(1 - \tfrac{192}{\pi^5} \tfrac{t}{w} \sum_{i=1, i\,odd}^{\infty} \tfrac{1}{i^5} \tanh\left(\tfrac{i\pi w}{2t} \right) \right) \tag{23}$$

In equation (23), when the thickness is greater than the width (t > w), function of t and w are exchanged.

For the design of the accelerometer device, the length of serpentine spring structures and the number of springs attached to the accelerometer proof mass were varied, both of which contribute to a change in the spring stiffness constant. Later, in

Chapter 4, we will discuss the fabrication steps for the spring/proof mass structures, where the dimensions after fabrication were measured and applied to equation (20).

The measured dimensions are as follows: spring thickness (t) 36 μm, beam width (w) 3 μm, connector beam length (a) 10 μm, the span beam length (b) 100, 150, and 150 μm, the number of meanders or turns (n) 4, and the number of springs attached to the proof mass (800 μm x 800 μm x 340 μm) 4 and 8. Using these dimensions, a solid model was created and simulated using Coventorware. First, a process flow was created to generate the solid model. Starting with a bare silicon substrate, four processing steps were used, one deposition (Au layer) and three etches (one wet, two DRIE). Next, the layout was designed using the abovementioned dimensions. Then, the solid model is generated using the process flow and designed layout of the spring/proof mass membrane. A mesh is added to the solid model, and the Memech solver is used to apply a specific load force to the membrane. The following conditions were imposed in the solver design: the ends of the springs were anchored in the x,y, and z directions; the springs and membrane were restricted to permit movement in the z-direction only; and a force (μN) was applied on the spring and membrane in the z-direction using "LoadPatchNodes". A 3D model is generated showing the spring/proof mass displacement. The processing, design layout, and 3D model are shown in Figure 3-13.

Number	Step Name	Layer Name	Material Name	Thickness	Mask Name	Photoresist	Depth
0	Substrate	Substrate	SILICON	340	SubstrateMask		
1	bond frame	Metal	GOLD	0.6			
2	bond frame etch				Metal	+	
3	Proof Mass Define				Metal2	+	315
4	Spring Membrane				Structure	+	27
5	Grating define	gratings	SI3N4	1			
6	Grating etch				Indent	+	

(a)

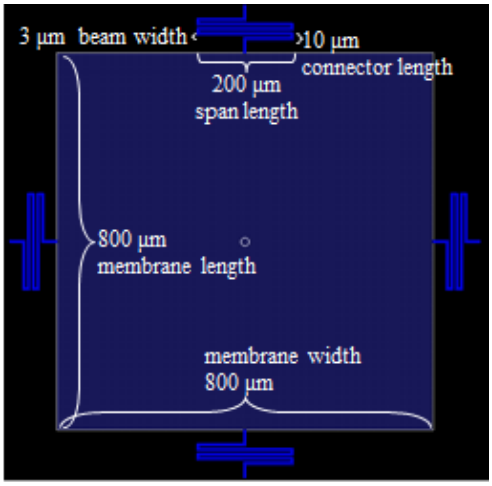

(b)

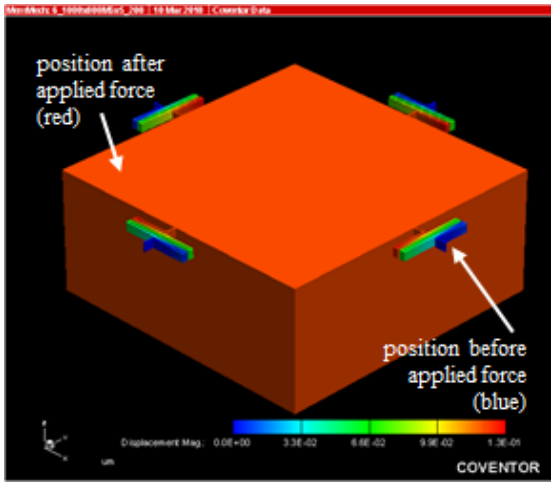

(c)

Figure 3-13: Conventorware simulation steps (a) processing steps (b) design layout (c) displaced 3D model from applied force

The results in Table 3-1 illustrate the spring stiffness constant for 4 spring and 8 springs, along with their associated spring parameters (bending and torsion) obtained from substituting these dimension into equation (20). The analytically and simulated spring stiffness constants are shown in Table 3-1, and the comparison of both spring constants are shown in Figure 3-14.

Table 3-1: Analytical and simulation calculations for the spring constant of 4 and 8 spring/proof mass membranes

# of turns	Bending Moment of Inertia I_x ($kg*m^2$)	Young's Modulus E (Pa)	Poisson's Ratio v	Torsion Modulus G (Pa)	Torsion Constant J(x, ab) (N·m/rad)	S(e, ab) E*I	S(g, ab) G*J	Thickness T (m)	Width w (m)	Connector a (m)	SPAN b (m)	Applied Force F_z (N)	**Analytical** 4 spr.const k_z (N/m)	**Simulated** 4 spr.const k_z (N/m)	**Analytical** 8 spr.const $2*k_z$ (N/m)	**Simulated** 8 spr.const $2*k_z$ (N/m)
4	11.7E-21	185.0E+9	0.3	71.2E+9	308.3E-24	2.2E-9	21.9E-12	36E-6	3E-6	10E-6	200E-6	39E-6	583.5	568.0	1167.0	1136.0
4											150E-6	39E-6	1004.3	1002.0	2008.5	2003.9
4											100E-6	39E-6	2060.1	2017.5	4120.3	4035.0

* Not shown are additional forces of 59, 78, and 98 μN that were applied to the spring/proof mass membranes with 200, 150, and 100 μm span lengths, in which the spring constant is the same for both the analytical and simulated 4 and 8

The green highlighted sections in Table 3-1 indicate the parameters that change, whereas, the red numbers are fixed. When the spring dimensions were calculated, it was observed that some of the physical spring parameters had a greater impact on the spring constant than others. They are as follows: changing the length of the span (*b*) beam by ±1 µm, the stiffness constant changed 6 N/m, changing the thickness (*t*) of the springs by ±1 µm, the stiffness constant changed 21 N/m, changing the length of the connector (*a*) beam by ±1 µm, the stiffness constant changed 70 N/m, and changing the width (*w*) of the span and connector beams by ±1 µm, the stiffness constant changed an astounding 310 N/m.

Understanding how these spring dimensions impact the spring constant value gives the designer an edge in creating any devices with serpentine spring structures. Figure 3-14 visually represents Table 3-1 and shows the comparison of analytical vs. simulation spring constant values for 4 and 8 spring proof mass structures. In Figure 3-14 (a), it can be seen that the spring constant values are close; moreover, the maximum difference 2.7% was between the springs with span lengths measuring 200 µm. This extremely good fit points out the reliability of the analytical model as a starting point.

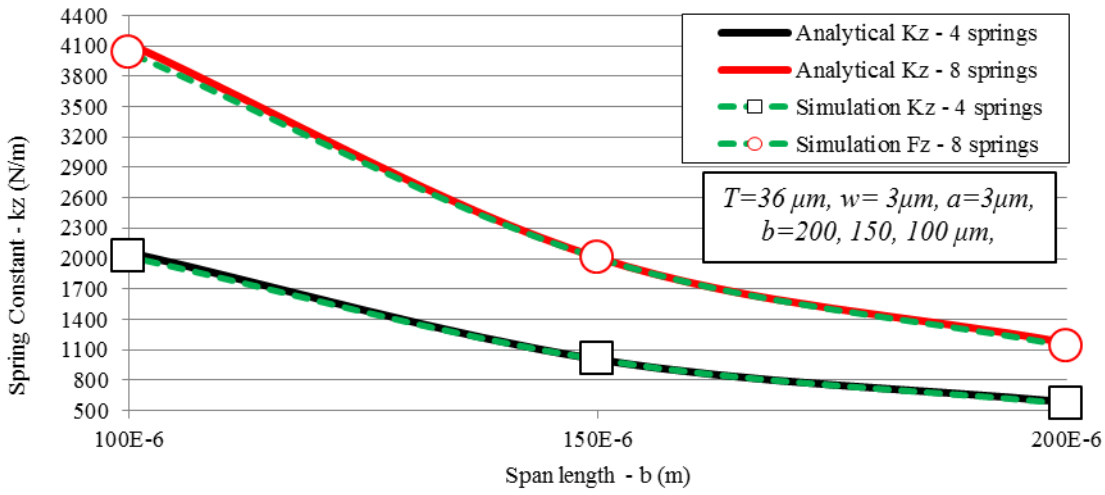

Figure 3-14: Analytical vs. Simulation spring constant comparison

From these results, the analytical model assisted greatly as a first approach method for determining the spring constant value. Furthermore, comparing both the analytical and simulation methods confirm that the data acquired was consistent and accurate. As a result, we can use the analytical data with confidence for estimating displacement versus force of the coupled SW grating accelerometer device.

3.3.2 Displacement Analysis of Serpentine Spring Structures

To evaluate the displacement of a serpentine spring for a known stiffness constant, a force is applied in the appropriate direction (z-axis) where the resulting displacement is the result of the force by the spring constant. This design analysis is substantiated by numerical calculation, mechanical simulation of the sensor structure obtained through finite-element analysis (FEA), and measuring the displacement.

In section 3.2.2, we reported the change in output intensity when the gap separation between the coupled SW grating pairs is moved further away or closer together. The referenced gap separation is displacement. When a force is applied to the proof mass with the connected springs, the spring/proof mass membrane will become displaced, thus causing the output intensity to change. From this change in output intensity, a correlation between displacement and output intensity can be inferred.

In this section, we will show displacement of the spring/proof mass membrane from analytical, simulation, and measured methods. In the previous section, the forces (F_z) were chosen based on assumed physical forces applied to the spring/proof mass structures. Knowing the spring constant and the force, the displacement can be calculated ($\delta_z = F_z / k_z$). In an ideal situation, any force that is applied to the spring/proof mass membranes will result in the same spring constant, hence the name spring

"constant". In contrast, the greater the force applied, the more displaced the spring/proof mass membranes will become. For that reason, Table 3-2 illustrates the analytical and simulated spring/proof mass displacement at different applied forces. A general observation can be realized in both the 4 and 8 spring groups; as the span length is decreased, the displacement also decreases. Additionally, as the force increases, likewise, the displacement increases.

Table 3-2: Analytical and simulated spring membrane displacement for 4 and 8 spring structures

Span Length b (m)	**Applied Forces** F_z (N)	**Analytical** 4 springs δ_z (m)	**Simulated** 4 springs δ_z (m)	**Analytical** 8 springs δ_z (m)	**Simulated** 8 springs δ_z (m)
200E-6	39.2E-6	67.2E-9	69.1E-9	33.6E-9	34.5E-9
150E-6	39.2E-6	39.1E-9	39.1E-9	19.5E-9	19.6E-9
100E-6	39.2E-6	19.0E-9	15.6E-9	9.5E-9	9.7E-9
200E-6	58.8E-6	100.8E-9	103.6E-9	50.4E-9	51.8E-9
150E-6	58.8E-6	58.6E-9	58.7E-9	29.3E-9	29.4E-9
100E-6	58.8E-6	28.6E-9	23.4E-9	14.3E-9	14.6E-9
200E-6	78.5E-6	134.4E-9	138.1E-9	67.2E-9	69.1E-9
150E-6	78.5E-6	78.1E-9	78.3E-9	39.1E-9	39.1E-9
100E-6	78.5E-6	38.1E-9	31.2E-9	19.0E-9	19.4E-9
200E-6	98.1E-6	168.1E-9	172.6E-9	84.0E-9	86.3E-9
150E-6	98.1E-6	97.7E-9	97.9E-9	48.8E-9	48.9E-9
100E-6	98.1E-6	47.6E-9	40.1E-9	23.8E-9	24.3E-9

In Table 3-2, above we observe the numerical relationship between the compared displacement values. These values are visually represented in Figure 3-15 (a-h). The analytical and simulated displacement in Figure 3-15 shows a good fit in the results. The 200 μm spring length that showed the greatest maximum displacement difference,

averaged to be less than 20%. The 100 µm and 150 µm spring lengths demonstrated are very close fit greater than 94%.

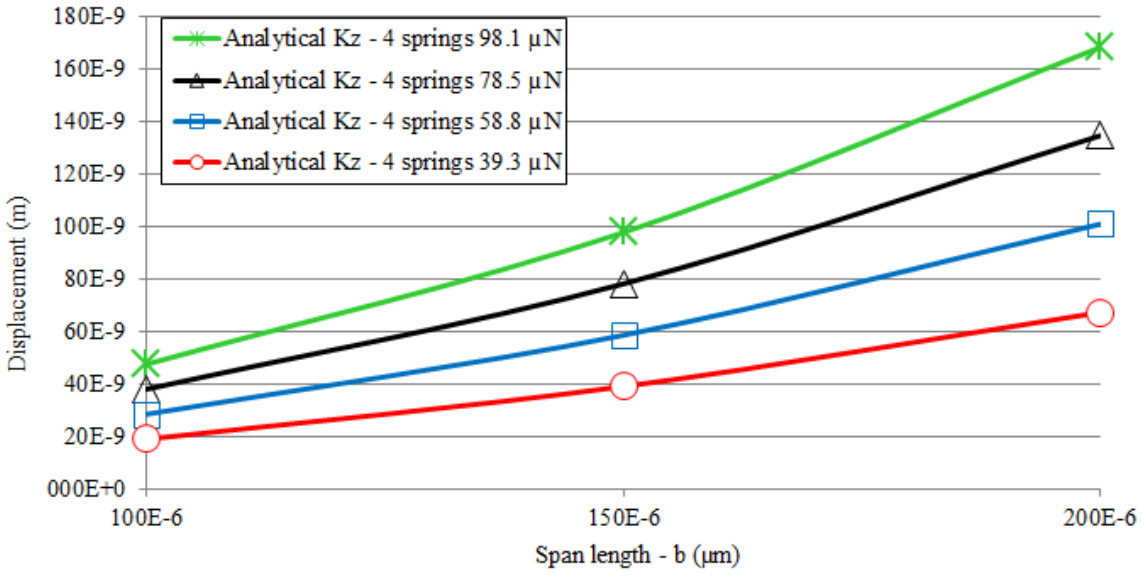

(a)

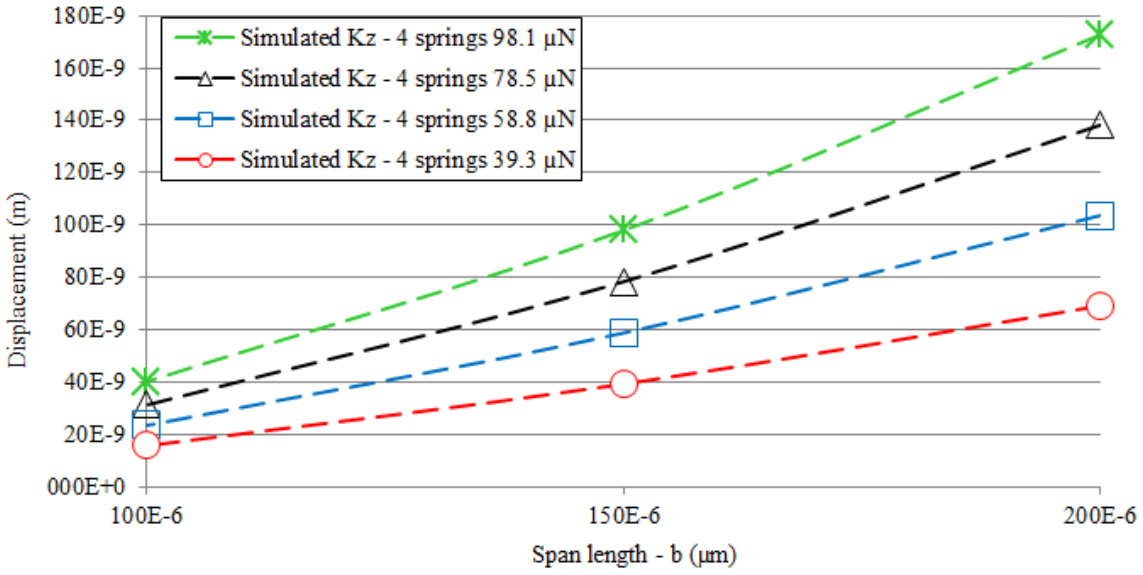

(b)

Figure 3-15: Analytical and simulation spring displacement for 4 and 8 springs at different forces and span lengths (a) analytical 4-spring (b) simulation 4-spring (c) analytical 8-spring (d) simulation 8-spring

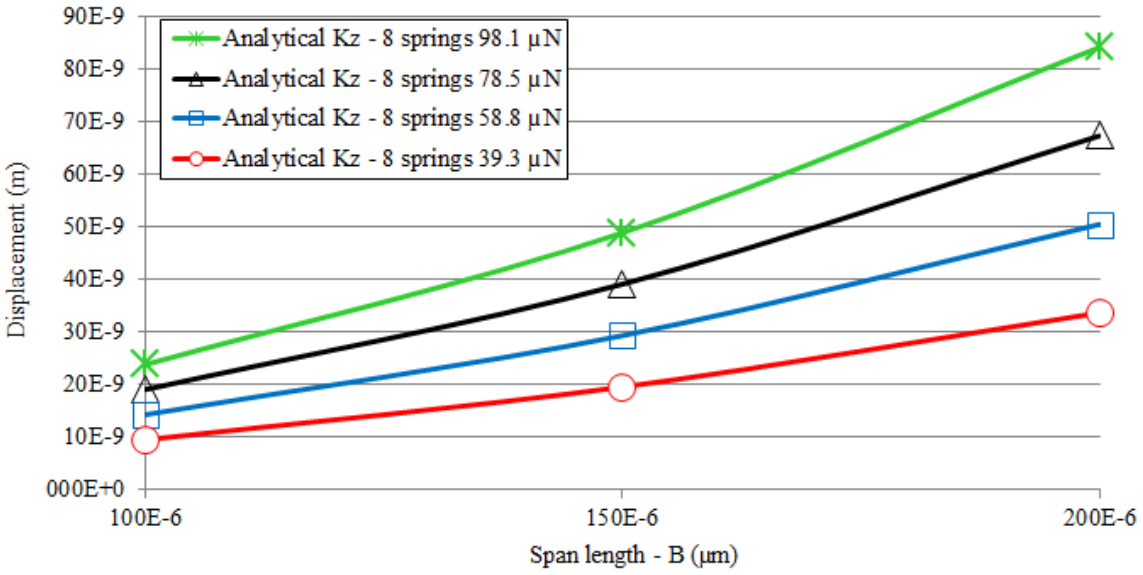

(c)

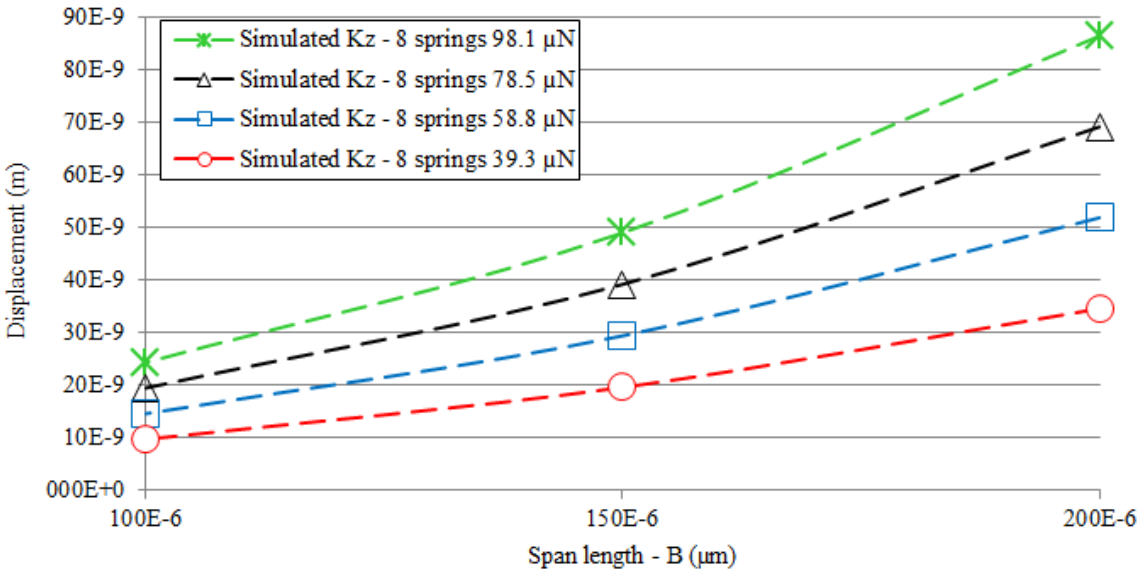

(d)

Figure 3-15 (Continued)

In this section, an analysis of the spring constant and displacement of an applied load force on different span length serpentine springs has been presented. The results from the spring parameters in Table 3-1 were analyzed, in which we were able to determine the impact of the lengths and thickness of the spring parameters have on the spring constant value. When comparing the analytical spring constant values to the simulation a greater than 94% goodness of fit was calculated. These results confirm that the two methods used to determine the spring constant are reliable.

Using these methods to substantiate the spring constant and displacement results, we can proceed with confidence, designing the masks and process fabrication of the spring/proof mass accelerometer structures, which will be described in Chapter 4.

3.4 Subwavelength Grating Fabrication

Evanescent wave coupling was first demonstrated by Gupta and Peng, where the gratings were patterned on a quartz substrate using holography and separated by a Corning glass film [10]. In the theoretical and experimental results presented by Gupta and Peng, they measured and calculated the diffraction angles from a doubly periodic structure. Their results did not consider coupling output efficiency or intensity measurement analysis from the subwavelength gratings.

To realize our accelerometer device, we have to determine the best method to fabricate SW gratings on the accelerometer. To accomplish this, several techniques were explored, including: electron-beam lithography, interference holography, and contact lithography. The techniques are summarized in the following section, with results and relative merits and drawbacks noted. Electron beam lithography was used to initially demonstrate SW grating coupling, to measure and compare the output intensity with the

simulated results. For final tested accelerometers, we used faster and more economical contact lithography to pattern all features.

3.4.1 Gratings Fabrication Using Electron Beam Lithography

The electron beam lithography (EBL) system used to write SW gratings was created by combining the JEOL JSM-5910 LV Variable Pressure scanning electron microscope (SEM) with the JC Nabity Lithography Systems software to control the electron beam. The EBL system, as shown in Figure 3-16 works as follows: a beam of electrons is generated in the electron gun and accelerated down the column by the attraction forces of the anode plate; the beam is condensed by a condenser lens and passes through an objective aperture to adjust the image resolution; the beam is deflected by magnetic scanning coils, and focused to a fine spot size for patterning on the sample coated with photoresist.

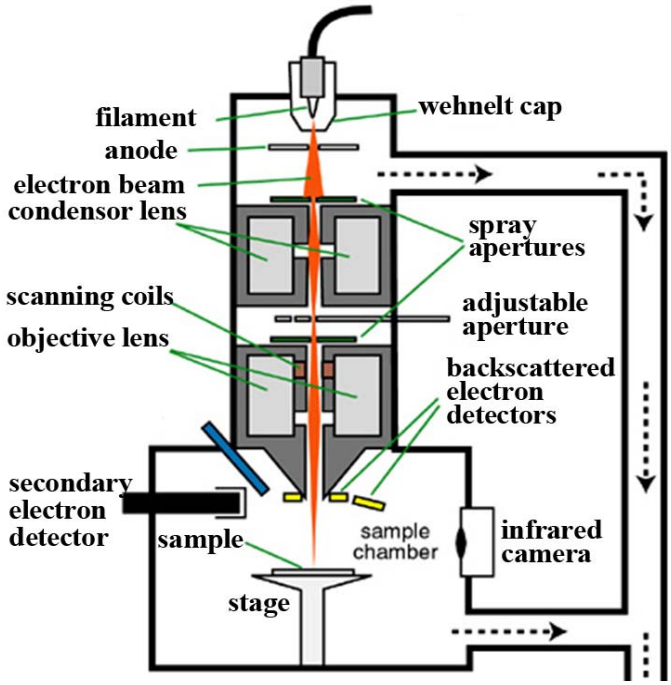

Figure 3-16: SEM/E-beam column overview [59]

The electron gun is the foundation of the EBL system. The fine pointed tip of a bent tungsten wire creates a high electric field needed to draw the electrons from the metal wire [60]. The metal anode plate has a hole in the middle of it and is extremely positively biased opposite the finely pointed tungsten wire, where this bias difference induces an attraction force that accelerates the electrons downward through the hole of the anode to the condenser lens and the rest of the EBL column. The SW gratings were patterned using a JEOL JBX-9300FS electron beam lithography (EBL) system. A silicon substrate was spin coated with ZEP-520, a high resolution e-beam resist in which 1.1 µm, 1.2 µm, and 1.3 µm period EBL gratings were patterned covering a 1 mm x 1 mm area for each grating type, as shown in Figure 3-17.

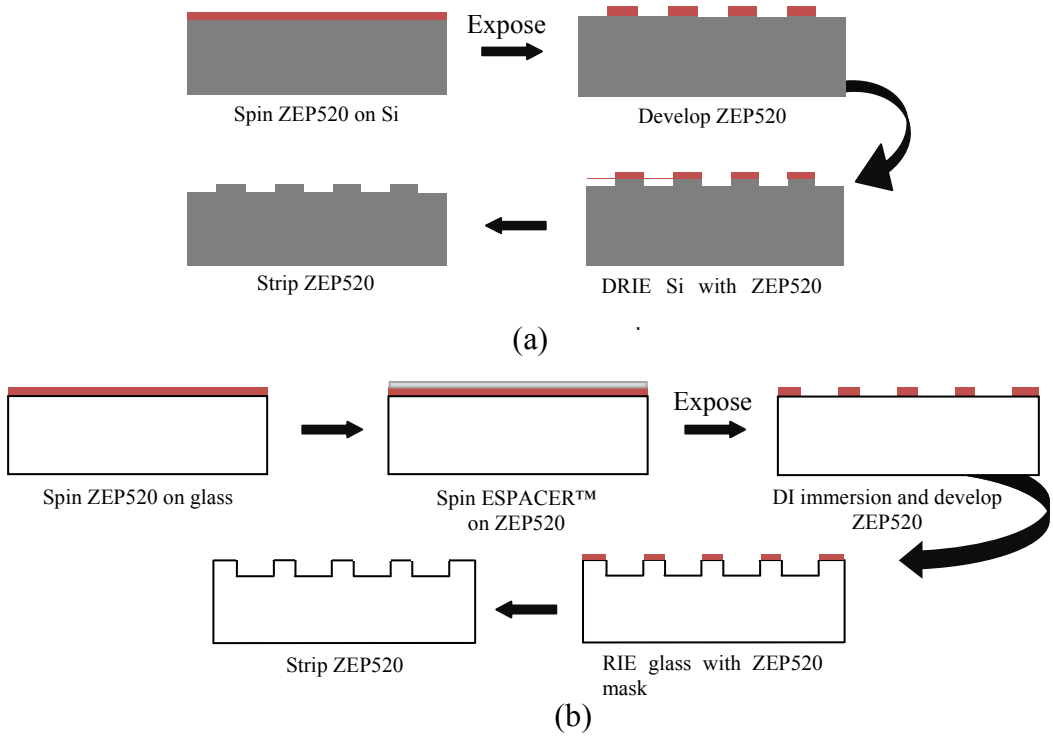

Figure 3-17: EBL grating process flow for glass and silicon (a) EBL process flow on silicon using ZEP520 (b) EBL process flow on a glass substrate with an ESPACER™ charge dissipation agent and ZEP photo resist

The substrate was developed in an ameyl-acetate solution and the patterned ZEP-520 was used as a hard mask to deep reactive ion etch (DRIE) gratings into the silicon substrate. A Pyrex substrate was similarly processed with 1.0 μm period gratings; however, there is a known surface charging issue when performing EBL on insulating substrates.

This issue has been heavily investigated and overcome in a variety of ways including by EBL writing at low pressure, and by depositing thin metal layers such as Cr and Al to dissipate charge [61-63]. In the present work, after the ZEP520 is spun on the glass substrate, a thin water soluble conductive polymer ESPACER™ (polyisothianaphthenesulfonate) is spun on the ZEP520 to dissipate the charge buildup during EBL as shown in Figure 3-17 (b). The sample is then exposed with the EBL SW grating pattern and rinsed in de-ionized water to remove the ESPACER™, and nitrogen blow dried. The sample is developed in amyl acetate to completely remove the ZEP520 that was exposed during the e-beam patterning. The glass and silicon etch depths were determined to achieve maximum coupling efficiency using the OptiWave™ software package based on a finite difference time domain (FDTD) numerical modeling approach. This optical software allowed us to simulate the optimal grating thickness for coupled SW gratings in silicon and glass substrates with a fixed gap between the two gratings, which is physically represented here in this work. The ZEP520 resist was used as a mask layer to etch the gratings 0.3 μm deep into the glass substrate using a Unaxis 790-10-RIE tool with trifluoromethane (CHF_3) and oxygen (O_2). The Si was etched 0.14 μm deep in silicon using a Unaxis SLR-7701-10R-B Bosch DRIE system. The wafers were cleaned in acetone and methanol, and in O_2 plasma. Then the wafers were anodically bonded using an EVG 501 wafer bonder with at 400 V bond voltage, 400º C temperature, 500

mTorr pressure for 20 minutes, and diced into test samples. The images in Figure 3-18 (a-d) show the gratings etched in silicon, glass, and the anodically bonded pair. Both the gratings etched in glass and the bonded pair were sputter coated with Au/Pd to dissipate the charge build up during SEM analysis.

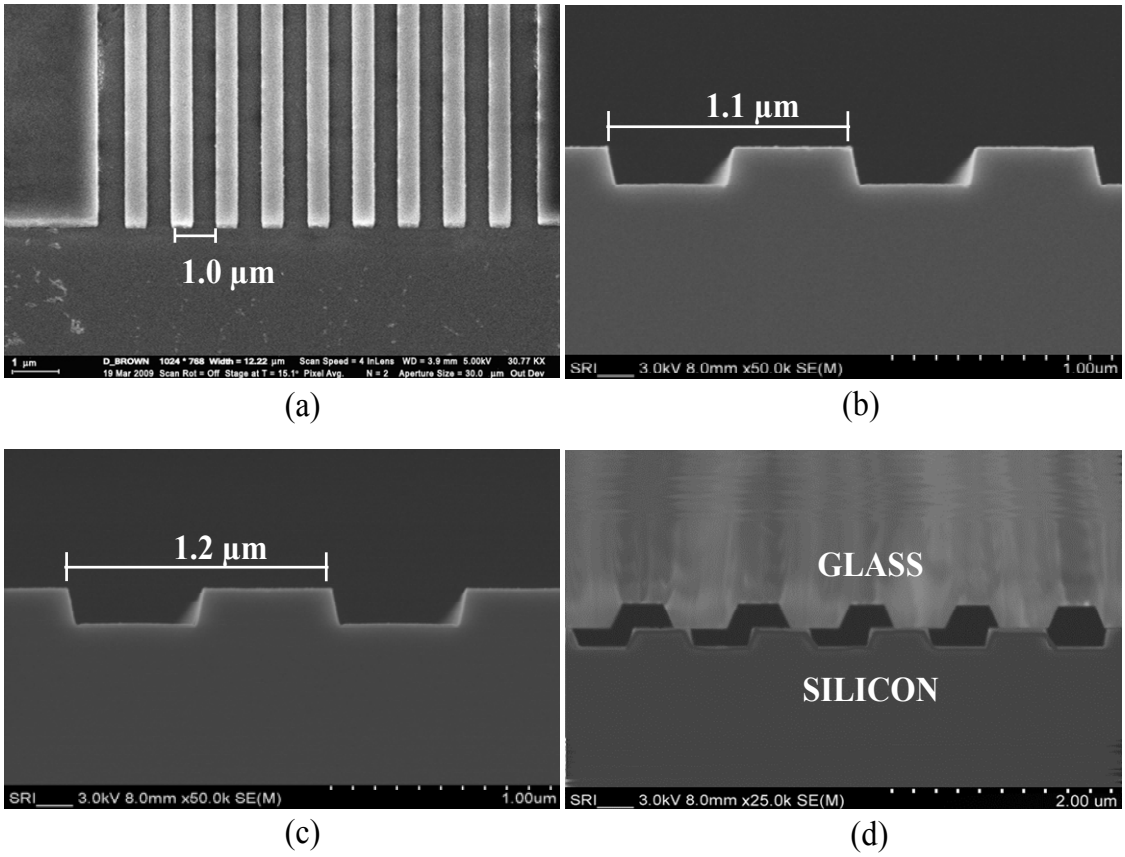

Figure 3-18: SEM images of the SW gratings (a) 1.0 µm SW gratings etched in glass (b) 1.1 µm SW gratings etched in silicon (c) 1.2 µm SW gratings etched in silicon (d) anodically bonded SW gratings

The SEM analysis revealed that the sidewalls of the SW gratings were sloped and not rectangular. Peng, et. al. demonstrated a similar behavior detailing the physical parameters of the grating configuration [64]. This trapezoidal grating profile was re-

simulated using the FDTD optical software to resemble the actual grating profile of the fabricated SW gratings, to estimate expected output intensity of light passing through the coupled gratings. The simulations were performed under the following conditions: wafer Dimensions: 8.00 µm (z-length) x 120.00 µm (x-width); mesh size = 0.02 µm (delta X) x 0.02 µm (delta Z); anisotropic perfectly matched layer (AMPL) boundary conditions; 20 µm (FWHM) 1.550 µm transverse electric (TE) polarized.

For the experimental setup a 1.55 µm IR laser beam was incident on one of the three coupled pairs and diffraction was observed in the far field, and the measured output intensity was recorded and compared with the simulation output. The measured output intensity was achieved using the setup shown in Figure 3-19.

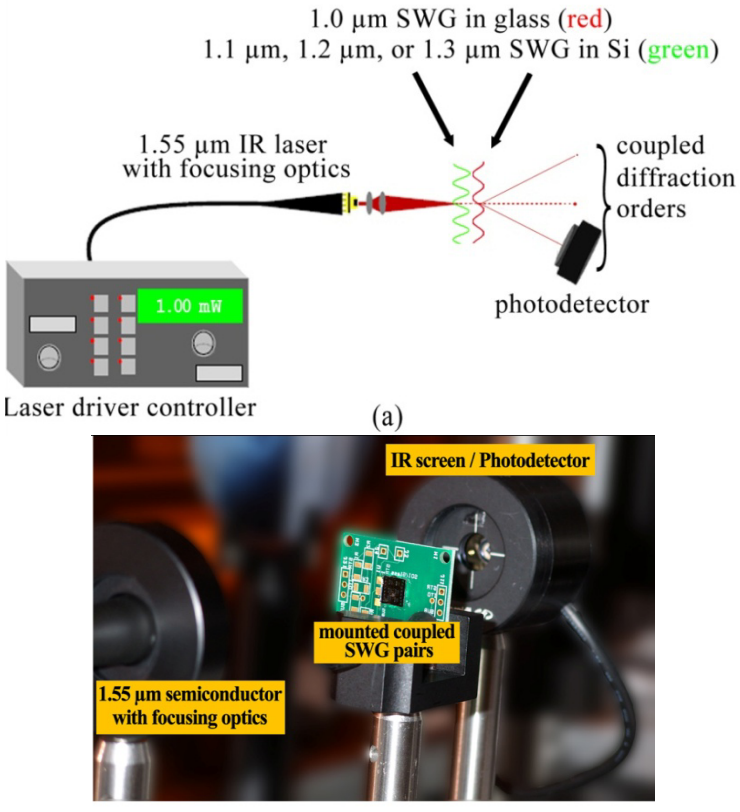

Figure 3-19: Coupled SW grating setup (a) schematic of the coupled SW grating setup (b) physical coupled SW grating setup

The setup includes a single mode 1.55 μm IR semiconductor diode laser (Mitsubishi ML925B45F) with focusing optics (Thorlabs LT230260P-C). The focusing optics is comprised of two aspheric lenses for focusing the beam to a small spot size. The first lens that the laser passes through has a numerical aperture (NA) of 0.55 to collimate the divergent beam emitted from the laser. The second lens has a NA of 0.25 to focus the light down. The lens pair is fixed within a threaded mount lens holder which allows adjustment of the lens' position to extend the beam's point of focus. The normal distance between the laser and the optic pair is 2.5 mm. The setup also includes a laser diode driver (Thorlabs DC201CU) in a constant optical power mode, a germanium IR photodetector (Newport 918D-IR-OD3) to measure the output intensity of the coupled SW grating pair, and power and energy meter (Newport 2935-C) to display the output power reading. The IR laser source and the coupled SW grating sample were separated by approximately 50 mm to focus the beam to a fine spot (approximately 15 – 20 μm) centered on the coupled SW gratings. EW coupling was observed as indicated by the higher diffraction orders seen on an IR sensitive detector screen. To measure the output intensity, we used the IR photodetector which was placed 25 mm from the coupled SW grating sample, with a 2 mm rectangular slit to block stay light and capture only a single diffraction order. To verify the accuracy of the photodetector output, the sample was removed and the laser was focused directly into the photodetector. The constant power input was set to 1.0 mW and the photodetector output showed an output value of 0.98 mW. Additionally, when the laser is normally incident upon the bonded glass and silicon interface, without gratings, the transmitted output power was measured to be 0.58 mW. This decrease in output intensity is a within 2% of the expected value due to Fresnel

reflections at the Si:air, Si:glass, and glass:air interfaces (31%, 16%, and 4% respectively). From these baseline output intensity experiments, the next section will discuss the results from the simulated and measured output intensity values.

The three anodically bonded coupled SW grating pairs (1.0 μm x1.1 μm, 1.0 μm x1.2 μm, 1.0 μm x1.3 μm), which represent having a 0 μm grating separation, were individually placed in the optical setup where IR laser was incident on the 1 mm x 1 mm coupled SW grating area. The output intensity for the three SW grating pairs was averaged over five recordings and is shown in Table 3-3. Additionally, the recorded averages are compared to the output intensity measurements from the Optiwave™ FDTD simulations, in which the constant power mode was kept the same as the input power for the measured results (1.0 mW). When comparing the output intensities of the measured data, which is measured in power (W), with the simulated data, having arbitrary units (a.u.), the units must be the same. To express the simulation results in terms of power (W), using logorithmic algebra in equation (24), the simualated data was normalized with respect to the measured data.

$$10 \cdot \log_{10}\left(\frac{P_{1st}}{P_{0th}}\right) = P_{dB} \tag{24}$$

$$10 \cdot \log_{10}\left(\frac{P_{1st,sim}}{P_{0th,mea}}\right) = P_{dB,sim} \qquad \rightarrow \qquad P_{1st,sim} = P_{0th,mea} * 10^{\frac{P_{dB,sim}}{10}} \tag{25}$$

In equation (24), P_{0th} and P_{1st} are the measured output intensities (a.u.) from the 0^{th} and 1^{st} diffraction orders, and P_{dB} is the normalized output in dB. In equation (25) the simulated 1^{st} order power and P_{dB} is taken from the FDTD simulation, and normalized to

the equivalent 0^{th} order simulated and measured powers. The simulated and measured data is represented in Table 3-3.

Table 3-3: Simulated and measured output power from the coupled SW grating pairs

Grating Pairs	**Measured** output power 0^{th} order (mW)	**Measured** output power $+1^{st}$ order (μW)	**Measured** output power $+1^{st}$ order (dB)	**Simulated** output power $+1^{st}$ order (dB)	**Simulated** output power $+1^{st}$ order (μW)
1.0 μm & 1.1 μm	0.39	9.3	-16.3	-13.2	18.2
1.0 μm & 1.2 μm	0.39	18.1	-13.3	-13.2	18.8
1.0 μm & 1.3 μm	0.38	6.6	-17.6	-16.2	9.4

The simulation of a single SW grating gave an output intensity at -66.4 dB or 89.3 pW and provided an output basline of what can be considered a background simulation noise. The results from 1.0 μm x 1.1 μm grating pair had the largest output power difference between the simulated and measured values. However, the output intensity difference for the 1.3 μm grating pair had a good fit > 70% and the 1.2 μm pair a fit of ~96 %. From our previous work [65], the noted 3.1 dB difference would result from a few nm gap between the gratings, which could arise from a particle defect being present between the anodically bonded grating surfaces. This can be noted in Figure 3-20, which shows the simulated output intensity vs. angle for a coupled 1.0 μm and 1.1 μm grating for various gaps between the gratings. Nonetheless, all three coupled SW grating pairs demonstrate significantly higher output power in the first diffracted order (53.2 dB) than the simulated intensity of a single grating, clearly demonstrating SW grating coupling.

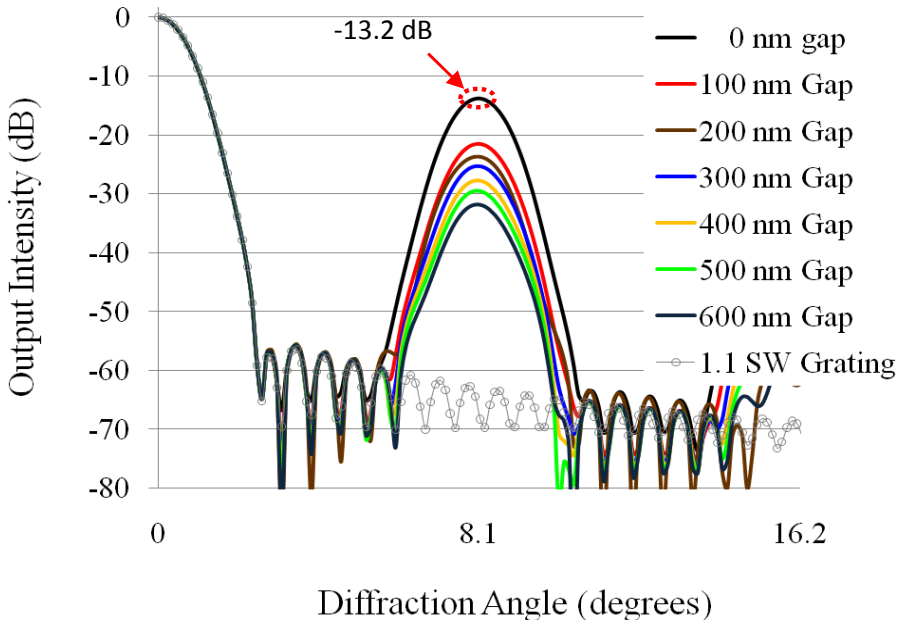

Figure 3-20: Output intensity vs. angle for 1.0 µm (etched 0.14 µm in Si) and 1.1 µm (etched 0.3 µm in glass) period gratings, separated by 0.0 µm to 0.6 µm by 0.1 µm increments

It has been shown for 1.0 µm and 1.1 µm, 1.0 µm and 1.2 µm, and 1.0 µm and 1.3 µm SW grating pairs, that EW coupling to generate propagating waves is realizable, both by calculated analysis and experimental verification. With propagating waves generated from the three SW grating pairs, the advantage of using the longer 1.0 µm x 1.3 µm SW grating pair versus the shorter 1.1 µm or 1.2 µm SW grating pairs is that the spatial separation of diffraction from the 1st order from the 0th order is larger. Additionally, fabrication of longer period gratings permits some process tolerance during fabrication. The calculated and measured output intensity of the SW grating pairs, which are in good agreement, show promise towards realization of physical MEMS sensors.

3.4.2 Gratings Fabrication Using Interference Beam Lithography

Interference beam lithography or holography is another method used in this research to fabricate SW gratings. Interference beam lithographic or holography, though not a standard microfabrication process, is capable of rapid optical exposure of a wafer, and so has the potential to be cost effective for mass manufacturing of the grating sensor. Holographic gratings are made by creating an interference pattern in a photosensitive material. This nanolithographic technique is completely maskless and creates patterns by beam superimposition.

Holography is accomplished by splitting a coherent laser beam into two paths, whereby constructively interfering the two beams at a specific angle onto a photoresist-coated substrate creates a standing wave pattern, or grating. This is be visualized in Figure 3-21 (a). The period of the grating (d) is defined by the wavelength of the illuminating laser (λ), the diffraction order (n), and the half-angle (θ) between the beams by the equation [66]:

$$n\lambda = d \cdot \sin(2 \cdot \theta) \qquad \Rightarrow \qquad d = \frac{n\lambda}{\sin(2 \cdot \theta)} \tag{26}$$

(a)

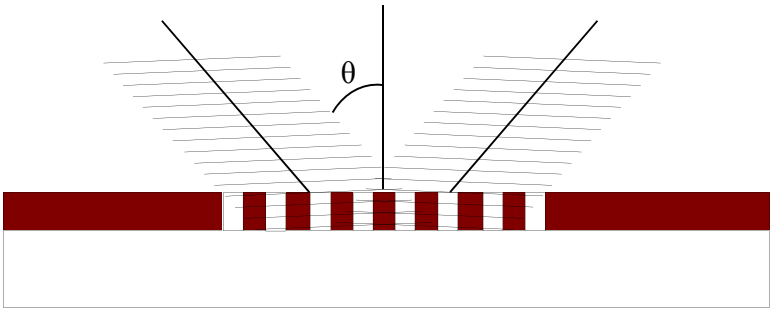

(b)

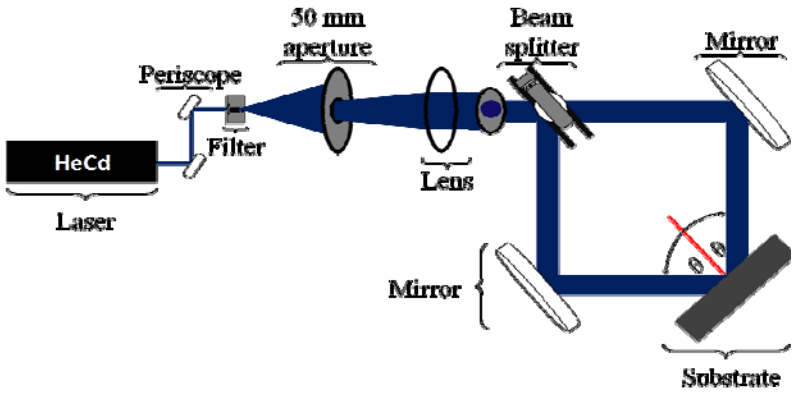

(c)

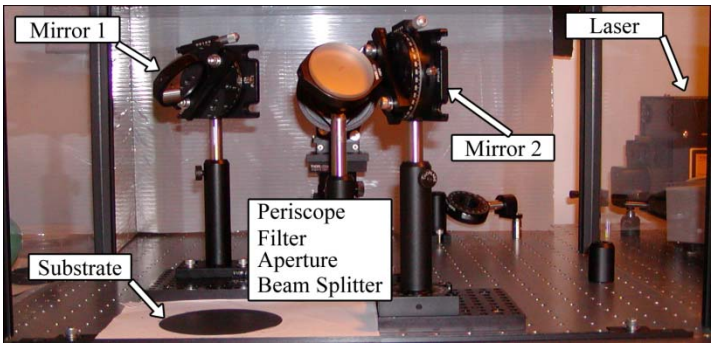

Figure 3-21: Holography exposure (a) Schematic of holographic constructive interference in photoresist material (b) representation of the holography setup for writing submicron period gratings in photoresist (c) photo of the holography setup used in this research

As shown in Figure 3-21 (b-c), the components used in holography systems include a high power laser source, filtering, collimating, splitting, and reflecting optics, and equally important, the recording media [67-73]. Our holography system was configured with the following: a 442 nm helium cadmium laser (Kimmon Corp., MA)

with 80 mW single mode polarized output power was used in this setup; an adjustable periscope with two one inch broadband mirrors to raise the incident source to a higher position; a five axis spatial filter with 10X microscope lens and 10 μm higher power pinhole used to filter, center, and expand the beam; a 50 mm aperture is inserted to minimize the beam's spot size; a plano-concave lens with 300 mm focal length is used to collimate the lens; a 25 mm aperture to make the collimated beam size smaller; a 50:50 beam splitter to split the beam into orthogonal paths; and two polished aluminum 1/20λ grade mirrors on rotating posts to direct the beams to the substrate coated with photoresist. The two beams were rotated at a specific angle to constructively interfere the two beams onto the photoresist coated substrate. The constructive interference results from the two coherent beams of the same frequency simultaneously present at the same location, thus creating a standing wave form pattern.

The photoresist commonly used for holographic patterning is Shipley's AZ 1350B [74-77]. In our experiments we used available Shipley's 1813 and Futurrex PR1-500A. In the initial experiment, both photoresists were spun on individual silicon wafers and exposed from 1 to 14 seconds in 1 second increments. The samples were developed in RD6 developer for 7 seconds. When inspected using an optical microscope, an unusual bull's eye pattern, called a moiré pattern was noticed, as seen in Figure 3-22. Moiré patterns are known to occur when there are two different grating periods present [78]. In other cases, moiré patterns occur when overlapping beams have misorientated angles [76]. An SEM image was taken to further inspect the pattern. The holography setup was checked, to verify there were not any scratches or dust particles on the optics, further investigation led to the beam-limiting aperture.

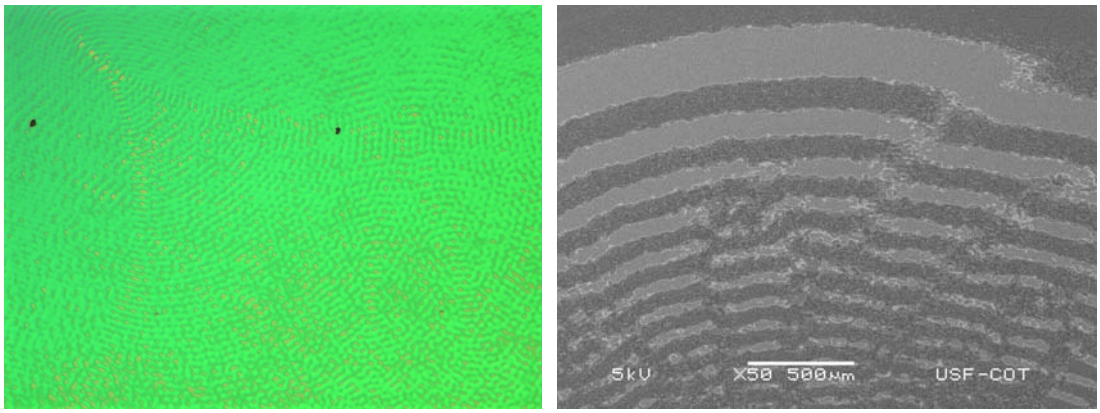

(a) (b)

Figure 3-22: Moiré Patterns (a) Moiré seen using an optical microscope (b) Moiré pattern from an SEM image

The 25 mm aperture was open 10 mm which caused aperture diffracted light to reflect through the system. The aperture should be located as close to the sample as possible to avoid diffraction effects and to shape the beam onto the exact desired exposure area. Enger and Case examined the effects of exposing thinner photoresist using holography produced uniform grating patterns [79]. Therefore, we used Futurrex PR1-500A, which could be thinned to 270-370 nm thick when spun at 5000 rpm. We used an ellipsometer to measure the resist thickness after being spun at 5000 rpm, and ~0.325 µm was recorded. The Futurrex data sheets indicated that it takes 40 mJ/ cm^2 to expose a photoresist layer 1 µm thick, so, 12 mJ/cm^2 should expose 0.325 µm thick photoresist. To determine the optimum exposure time, the exposure intensity (I = P/A) must be known, where *P* is the output power (mW) and *A* is the area (cm^2). This is established by measuring the output power as the laser beam is reflected from the Al mirrors using the Newport photodetector. The measured output power was ~9.4 mW and

the beam radius was 1.6 cm. With the output power and beam radius we can calculate the area and exposure intensity as:

$$area\,(A) = \pi \times r^2 = \pi \times \left(1.6\right)^2 = 8.05\,cm^2 \tag{27}$$

The exposure intensity was calculated to be:

$$I = \frac{P}{A} = \frac{9.4\,mW}{8.05\,cm^2} = 1.17\,\frac{mW}{cm^2}. \tag{28}$$

This gives us an exposure time of:

$$\frac{12\,\dfrac{mJ}{cm^2}}{1.17\,\dfrac{mJ/\sec}{cm^2}} = 11.0\,\sec \tag{29}$$

When the exposed samples are placed in the developer, the samples are developed extremely fast, which leave little room for process latitude. Diluting the developer significantly improves the process latitude and allowed the sample to remain in the developer longer to fully develop. The diluted developer and exposure times are shown in Table 3-4.

Table 3-4: Diluted developer comparison

RD6 : Water Solutions	Exposure Times (seconds)								
75 mL : 0 mL	9.5	10.0	10.5	11.0	11.5	12.0	12.5	13.0	13.5
75 mL : 50 mL	9.5	10.0	10.5	11.0	11.5	12.0	12.5	13.0	13.5
75 mL : 25 mL	9.5	10.0	10.5	11.0	11.5	12.0	12.5	13.0	13.5

The 13.5 second exposure, in 75 mL: 25 mL diluted developer for 18 seconds yielded the best results. After optimizing exposure and developing times, an undesirable effect, as shown in Figure 3-23, was observed during exposures. The beam splitter was generating a secondary reflection off its broadband antireflection coated surface. Increasing the propagation distance between the beamsplitter and sample removed this effect.

(a) (b)

Figure 3-23: Reflection issue in the optical setup (a) Image of multiple reflections as the beamsplitter splits the beam and reflects from the Al mirror (b) The result of multiple reflections as the beam exposes the sample

This same experiment was performed on glass, and since glass is transparent, the grating period can be determined from the diffraction angles using simple trigonometry calculations. A schematic of this can be seen in Figure 3-24 showing the diffraction orders of a grating created using holography.

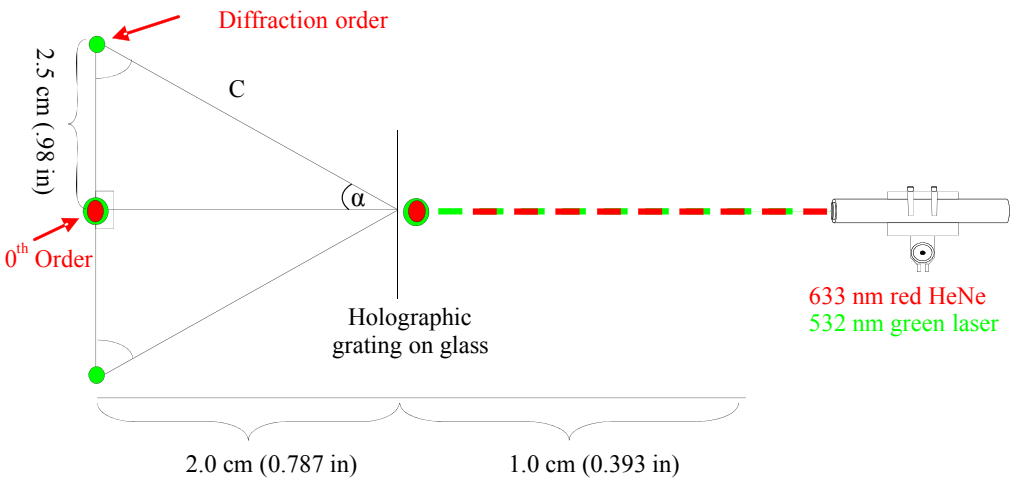

Figure 3-24: Schematic illustrating how the grating period is calculated by illuminating the SW grating with a 532 nm or 633 nm laser, and using trigonometry equations

Using the trigonometric tangent equation, defined as the opposite leg divide by the adjacent leg, the diffraction angle from the grating can be calculated, which in turn allows for calculation of the grating period.

$$\tan = \frac{opposite}{adjacent} \cdots\rightarrow \quad \alpha = \tan^{-1}\left(\frac{2.5}{2.0}\right) = 51.3^{o} \tag{30}$$

Using the grating equation (18), the grating period can be calculated as:

$$n\lambda = \Lambda \cdot \sin(2 \cdot \alpha) \quad \Rightarrow \quad \Lambda = \frac{n\lambda}{\sin(\alpha)} \quad \Rightarrow \quad \Lambda = \frac{1 \cdot 532\,nm}{\sin\left(68.9^{o}\right)} = 570\,nm \tag{31}$$

This approximated grating period can be verified by illuminating the grating in glass with two different wavelength lasers. If the grating period (Λ) is ~ 550 nm, diffraction orders should be present when illuminated with the 532 nm laser ($\lambda<\Lambda$). Conversely, there should not be any diffraction orders when the 633 nm laser is illuminated ($\lambda > \Lambda$) on the

grating, which is seen in Figure 3-25 (b). Also, we can see in Figure 3-25 (b) that the photoresist was not completely exposed during holographic patterning, perhaps due to back reflections from the substrate. An absorptive coating could help this, but was not attempted in this effort, as we were able to successfully pattern and transfer gratings with several hundred nanometer thickness into several materials of interest (Si, Si_3N_4, and glass).

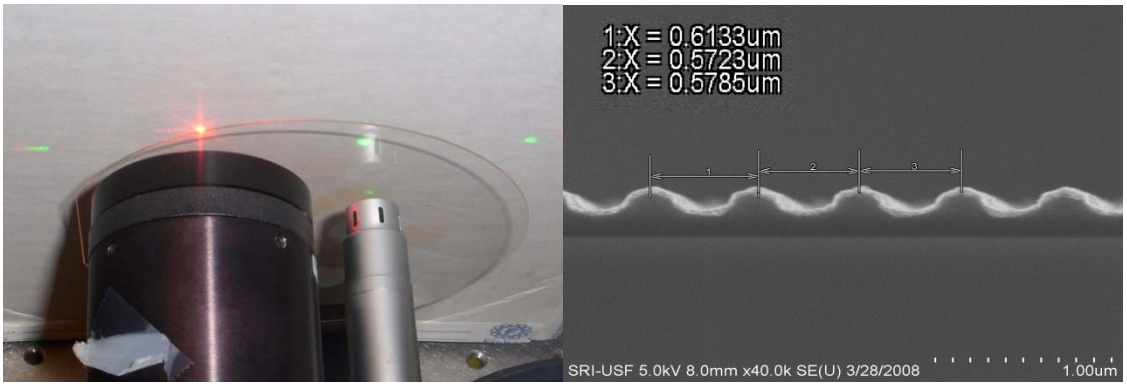

(a) (b)

Figure 3-25: Subwavelength grating diffraction and imaging (a) Setup illustrating the gratings are sub-λ to the 633nm incident source and are diffractive to the 532nm source (b) SEM image with a measured holographic grating period of ~570 nm in silicon

The exposure and development has been optimized for this holography setup, with 13.5 seconds exposure and 18 seconds development in 3:1 developer solution (RD-6: water). Although we were successful in writing gratings with a period less than 0.4 μm, we concluded to pursue additional SW grating fabrication methods. This decision was attributed to the variation is grating dimension (rounded edges) during processing.

Chapter 4

Mask Design and Accelerometer Fabrication

4.1 Accelerometer Mask Design

This section presents in detail the design of the four masks used in fabrication of the coupled SW grating MEMS accelerometer. The four masks were designed using Coventoware™ and were commercially reproduced on five inch glass plates, with a Cr metal hard mask.

The first mask, labeled INDENT is a bright field mask and contains the SW gratings for both the Si and glass substrates. The grating periods were chosen based on the simulations performed in the previous chapter and is shown in Figure 4-1. The INDENT mask was specially designed, and was created using electron-beam lithography. This was necessary because the dimensions of the designed gratings were below the minimum feature resolution of a standard mask reproducer. The mask design had three different grating periods, 1.0 μm and 1.4 μm for the gratings to be used for Si, and 1.2 μm gratings for the glass substrate. The grating design in Coventorware™ was created by first drawing a single grating and then creating an array of the line.

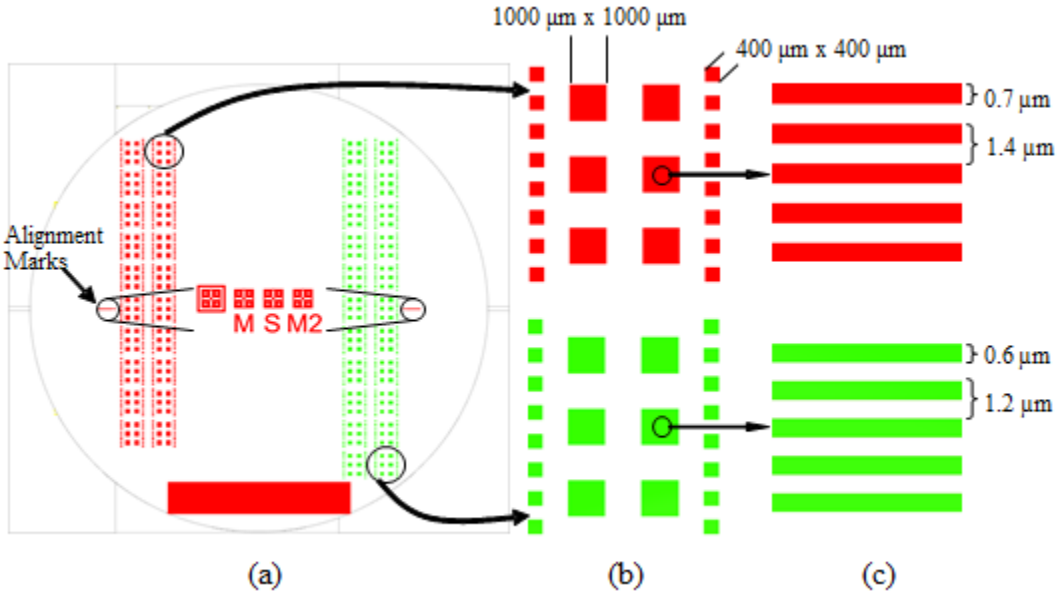

Figure 4-1: INDENT mask design (red – Si SW gratings, green – glass SW gratings) (a)The wafer scale view of the SW grating mask (b) Single chip level design of the INDENT mask (c) a magnified view showing the grating dimensions

It can be seen in Figure 4-1 that there are two different grating array sizes which measure 400 µm x 400 µm and 1000 µm x 1000 µm. Normally, Cr master glass plates are duplicated to preserve the features on it, but due to the importance of the design step, the master plate was used. This maintains the integrity of the grating dimensions, unlike the altered features caused during exposure and development that are present when a mask is duplicated. Last and a critical component are the alignment marks. The alignment marks for the remaining three masks are designed here to accurately align the features on the successive masks.

The second mask, METAL 1, is the simplest design of the four masks. METAL 1 is designed as a frame that will border the Si accelerometer device and the glass lid for the purpose of Au:Au thermocompression bonding. The Au bondframe is designed to border the SW gratings on the INDENT mask. The first bondframe that borders the 400

µm x 400 µm grating arrays measures 780 µm x 780 µm and has a 420 µm x 420 µm square cutout in the center. Additionally, the other bondframe that borders the 1000 µm x 1000 µm grating arrays measures 1900 µm x 1900 µm and has a 1100 µm x 1100 µm square cutout in the center. As well, the alignment marks are placed on both sides of the mask to align to the INDENT mask. The Au bondframe mask and its dimensions are shown in Figure 4-2.

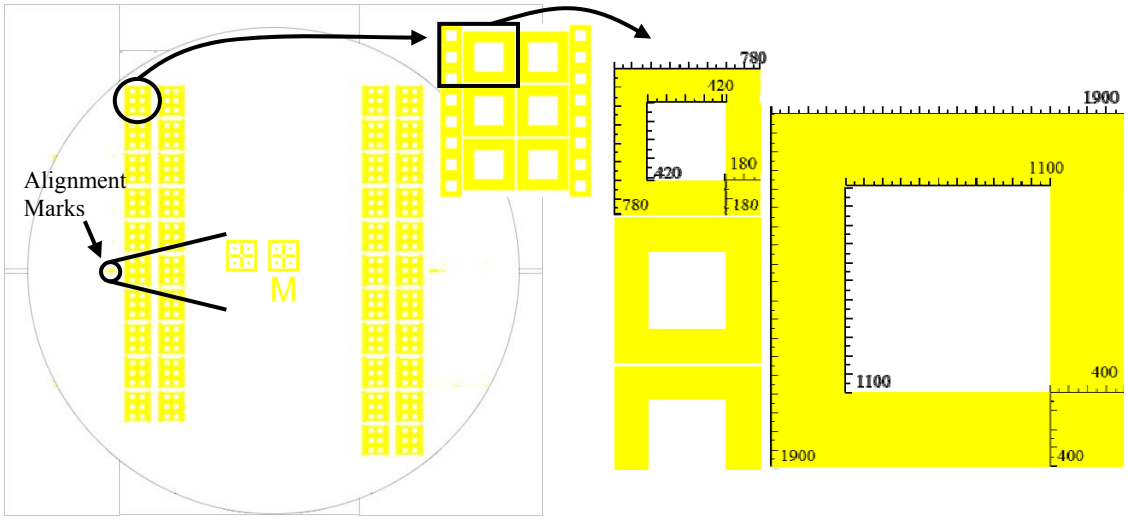

Figure 4-2: METAL 1 mask design

The METAL 2 mask is the most complex mask as it relates to processing. This is a backside alignment mask and serves as the mask to DRIE > 90% of the bulk Si from the back of the wafer. This mask serves a two-fold purpose. First, it defines the bottom portion of square proof mass for the Si accelerometer. Second, the mask defines a 100 µm open trench area that will be DRIE etched to define the areas where the springs will be released after the last mask step. Knowing that sharp corners tend to undercut during wafer processing, the 100 µm open trench is designed with rounded corners to provide

some process latitude compensation. The alignment marks are designed and placed within the view of the EVG 620 mask aligner objective lens. This will ensure proper alignment to the previous masks. This mask is shown in Figure 4-3.

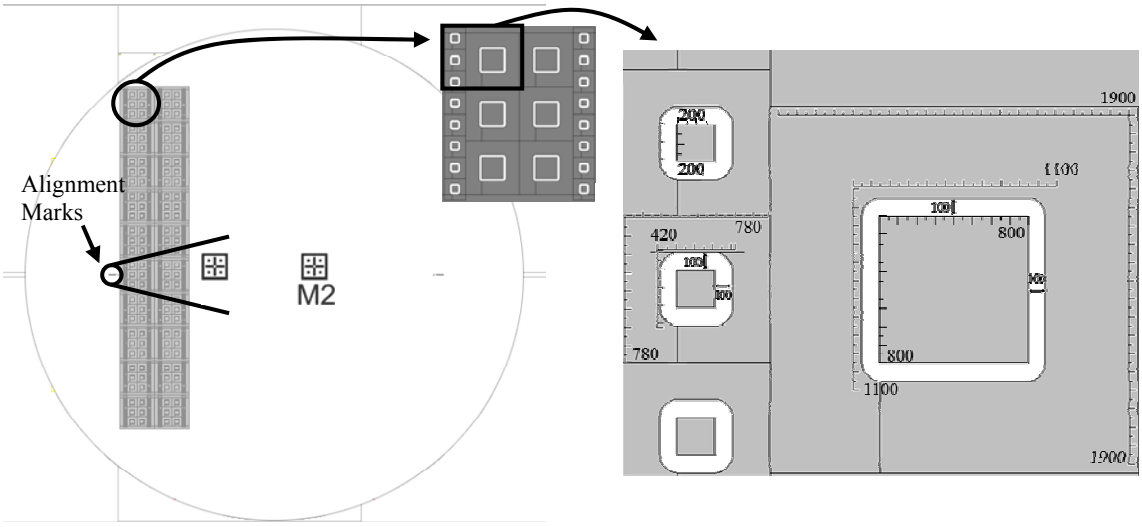

Figure 4-3: METAL 2 mask design

The final mask for the coupled SW grating accelerometer is the STRUCTURE mask. Its purpose is to define both the springs and the proof mass of the accelerometer. The dimensions of the two proof masses are 200 µm x 200 µm and 800 µm x 800 µm, which was intentionally designed smaller than the INDENT mask to ensure that the SW gratings completely cover the proof mass. Also, four and eight springs of each of the three springs styles with different span lengths (100, 150, and 200 µm) were attached to the proof mass. This mask is used as the final DRIE etch (~35 µm) to release the accelerometers.

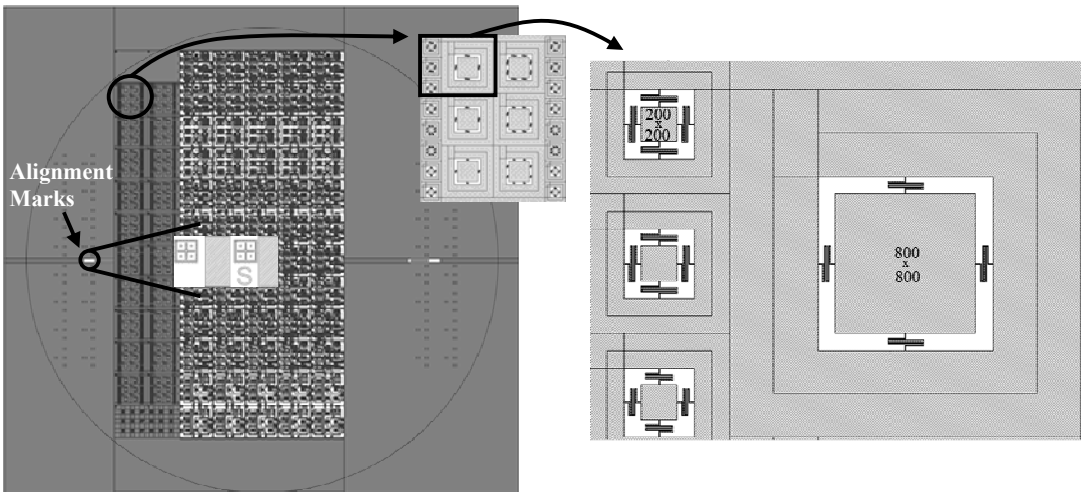

Figure 4-4: STRUCTURE mask design

4.2 Accelerometer Process Flow

This section presents in detail the fabrication steps and processes used in this research. Section 4.2.1 gives an introduction to the MEMS fabrication techniques used in these processes. Section 4.2.2 explains the fabrication of the glass lid for the accelerometer device and details structural dimensions of the glass lid. Section 4.2.3 specifies the complete fabrication process of the Si spring/proof mass accelerometer, with SW gratings. Additionally, the process explains the material layers used and details all procedural steps, as well as the chip level bonding process. The detailed process flow is in Appendix A.

4.2.1 Dry Etching

MEMS fabrication or micromaching is characterized as having dimensions that are micrometers in size. MEMS utilizes etching methods to subtract material from the

substrate or deposition methods to add material to the substrate [80]. These two methods are respectively described as bulk and surface micromachining.

Bulk micromachining was developed between 1970 and 1980, as an extension of IC technology, for fabrication of 3D structures [81]. Thus, a basis understanding of IC fabrication processes such as film growth, doping, lithography, etching, dicing, and packaging is helpful in learning MEMS fabrication processes. Bulk micromachining can be classified into two different categories depending on the medium of etchant used: dry etching and wet etching [82]. Dry etching uses plasma (high energy ionized radicals) or vapor phase etchants to etch bulk of material, typically Si, whereas wet etching uses liquid chemical solutions for etching.

Deep reactive ion etching (DRIE) is one of the most important and popular dry etching techniques used in MEMS processing. The popularity of DRIE derives from its anisotropic etch profile. The ability to obtain near vertical sidewalls with high aspect ratios and anisotropic shapes is favored among MEMS process engineers. DRIE of bulk Si is usually performed with the Bosch process. The Bosch process successively etches and deposits a passivation layer using specific gases in each step [83]. The first etch step is normally 5-10 seconds and uses SF_6 to etch the Si. The passivation is achieved by deposition of a polymer using C_4F_8 as a source gas. Concurrent with this deposition step is some ion bombardment, and this prevents the formation of polymer on the bottom of the trench. The polymer on the bottom of the trench is removed by energetic ions during the following etch step done in SF_6 [84].

To DRIE insulating substrates (glass) an extremely high plasma power would be required. Therefore, the other dry etching technique used was reactive ion etching (RIE).

RIE uses different gas chemistry (CHF_3 and O_2) than DRIE and it does not have passivation cycles. By configuring the gas chemistry, the etch rate can be increased and the glass substrate can be etched [85].

4.2.2 Accelerometer Glass Lid Process Flow

The accelerometer glass lid is fabricated using two of the four masks. The first mask defines the SW gratings and was a specialty mask produced by Photronics, Inc. It was created using electron beam lithography (EBL) to resolve the 0.6 μm line width that is required for this design. Half of this mask was created with SW gratings for the glass lid and the other half for the bulk Si structure, both of which defines the SW gratings which have different grating periods. The first step in the glass lid process consists of selecting a 100 mm diameter, 500 μm thick glass wafer. After selecting the wafer, it is cleaned using acetone and methanol, rinsed, dried using a nitrogen blow gun. The substrate is spin coated at 3000 rpm with hexamethyldisilazane (HMDS), an adhesion promoter, for 40 seconds and placed on the hotplate at 120° C for 60 seconds. Then Futurrex PR1-500A is spun at 5000 rpm, resulting in ~ 0.3 μm thick photoresist and placed on the hotplate for 120 seconds at 120° C. The normal pre-bake time is 60 seconds; however, the substrate is insulating and requires a longer bake time. The first mask (INDENT) with the SW gratings pattern is exposed onto the wafer using the EVG - 501 mask aligner for 2.9 seconds. The wafer is developed in RD6 developer solution for 12 seconds and then rinsed with DI water. After dried, the wafer is inspected in the optical microscope to verify SW grating consistency. After inspection, the wafer is post baked at 100° C for 60 seconds. Using the photoresist as a hard mask, the substrate is

RIE etched for 10 minutes using a gas mixture of CHF_3 and O_2 plasma. The resulting RIE etch depth was ~ 0.3 μm as shown if Figure 4-5.

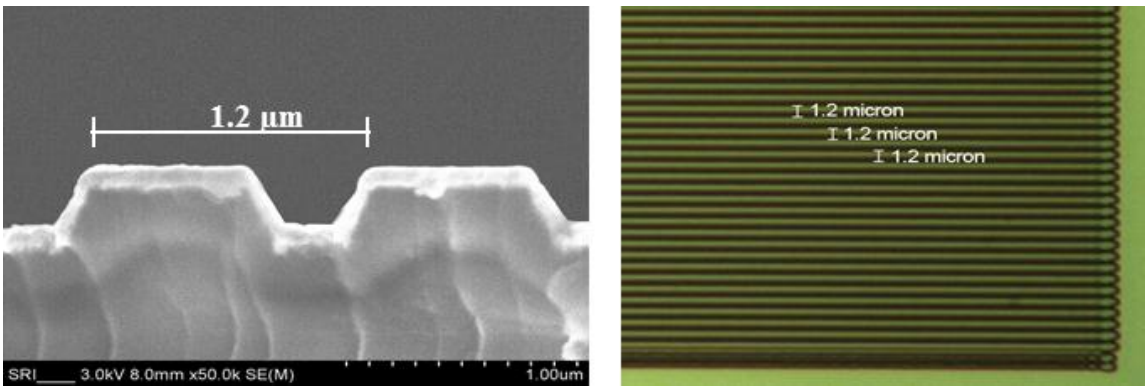

(a) (b)

Figure 4-5: SEM image of the SW gratings etched into the glass substrate coated with Au/Pd to dissipate charging (a) cross-section view (b) microscope view of the SW gratings

After removing the remaining photoresist with acetone/methanol and a 3 minute O_2 plasma in the Tepla, using the AJA-ATC1800, 300 nm Cr/Au was sputter coated on the front side of the glass wafer, covering the SW gratings. The second mask layer (METAL 1) defines the Cr/Au bond frame for Au:Au thermo-compression (TC) bonding which will be discussed further. The glass wafer was spin coated at 3000 rpm with PR1-2000 for 40 seconds and placed on the hotplate at 120° C for 60 seconds. The METAL 1 mask was exposed for 4.2 seconds and developed in RD6 developer solution for 40 seconds. After rinsing and drying, the wafer was inspected in the optical microscope to check the alignment with the previous layer. After inspection, the wafer is post baked at 100 ° C for 60 seconds. The Cr/Au layer was etched in Au etchant for 4 minutes and Cr etchant for 60 seconds, resulting in a 100 μm gold bond frame centered around the SW gratings. This can be seen in Figure 4-6.

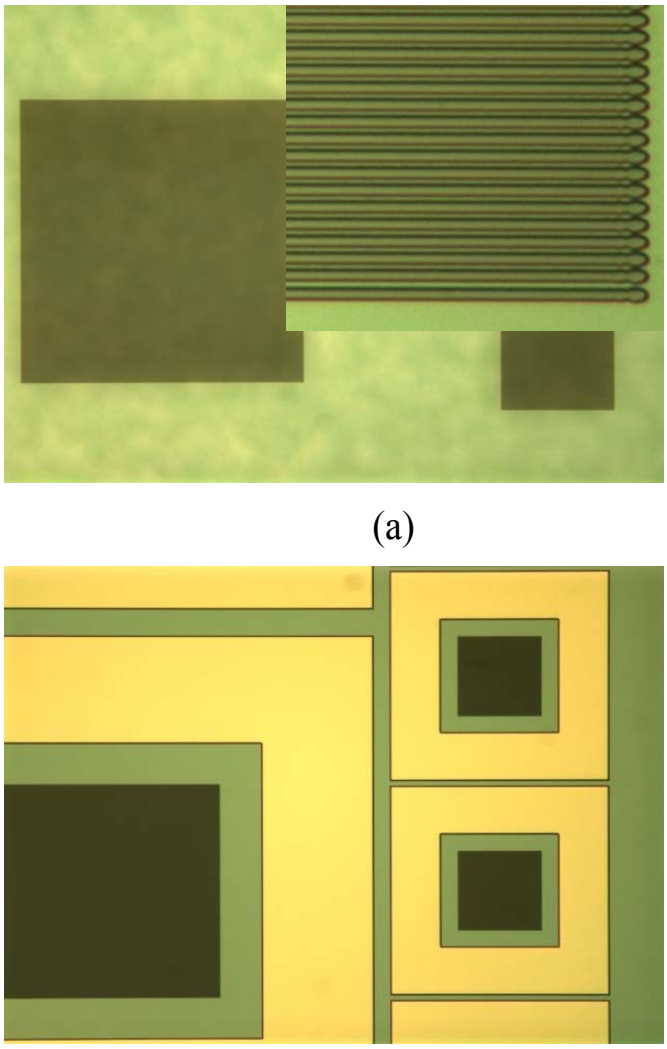

Figure 4-6: Optical image of the first two lithography steps (a) INDENT mask of the SW gratings etched into the glass substrate (b) METAL 1 mask showing the Cr/Au bond frame on the glass substrate

More photoresist was spun on the glass lid and baked at 120°C for 60 seconds to protect the wafer during the wafer dicing process. The wafer was diced to get individual glass chips (7 mm x 7 mm). After dicing, the chips were then cleaned in acetone/methanol to remove the dicing debris and photoresist, in which the chips were then placed in isopropanol (IPA). The chips were dried in an oven at 80°C for 10 minutes and are ready

to be bonded to the bulk silicon accelerometer device. The complete process flow of the glass lid for the accelerometer is shown in Figure 4-7 (a-d).

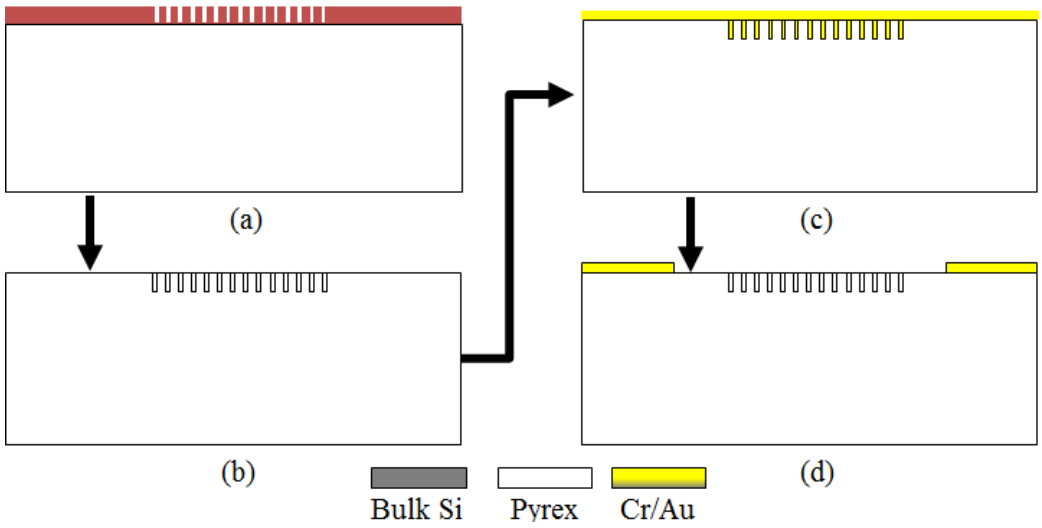

Figure 4-7: Schematic process flow of the bulk Si accelerometer device (a) INDENT mask patterned to define the SW gratings (b) SW grating etched into the Si substrate (c) Sputtered Cr/Au for Au bond frame (d) Patterning of the METAL 1 mask and wet etching the Cr/Au defining bond frame

4.2.3 Bulk Silicon Process Flow

The bulk Si accelerometer structure consists of a spring/proof mass system with SW gratings etched into the proof mass. This structure is fabricated using the four masks labeled: INDENT; METAL 1; METAL 2; STRUCTURE.

The first step in the process consists of selecting a 100 mm diameter, 340 μm thick double side polished (DSP) <100> Si wafer. The INDENT mask was almost identically prepared as the glass lid; the adhesion promoter, HMDS was applied, PR1-500A was spun at 5000 rpm, and the pre bake times were the same as the glass substrate, except the PR1-500A was baked for 60 seconds, as stated by the data sheet for Si. Etching the grating into the substrate was done using DRIE, not RIE, as RIE was used to

transfer the gratings into the glass substrate. Previously mentioned, the BOSCH process DRIE etches and deposit a passivation layer using specific gases in each step. To transfer the shallow depth gratings into Si substrate, a non-Bosch DRIE process was used. This process does not include a passivation step and is a timed etch process, whereas the Bosch process etches in cycles. A two minute and thirty second non-Bosch process resulted in SW gratings etched 0.12 μm into the Si substrate as shown in Figure 4-8.

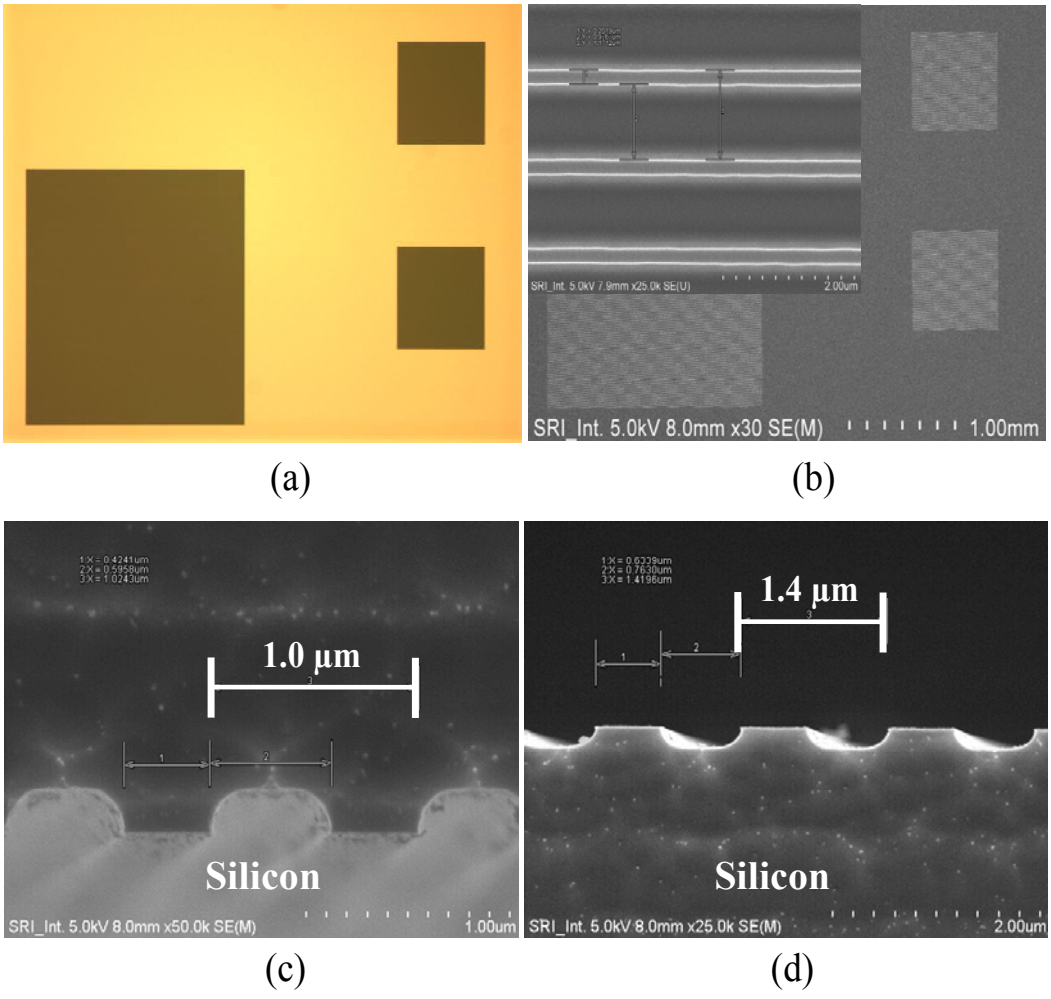

Figure 4-8: Optical and SEM images of the INDENT mask etched in Si (a) INDENT mask of the SW gratings etched into the Si substrate (b) SEM image of the SW gratings etched 0.12 μm in the Si substrate (c-d) SEM cross-section showing the grating periods of 1.0 μm and 1.4 μm respectively

Similarly, the second mask, METAL 1 was also almost processed identically to the glass substrate. The only difference was the pre-bake time for the PR1-500A was for 60 seconds, as stated by the data sheet for Si. After fully processed, the METAL 1 layer was ~ 0.3 μm thick. Figure 4-9 (a-b) shows both the INDENT and METAL 1 layers on the Si wafer.

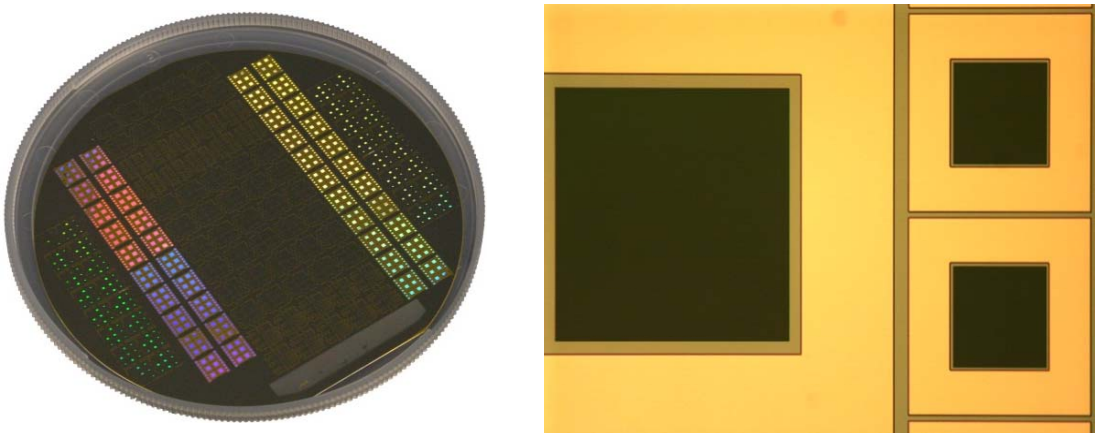

(a) (b)

Figure 4-9: Optical image of INDENT and METAL 1 photolithography steps (a) photograph of the two mask layers on the entire wafer (b) microscope image verifying the alignment of the two layers

The remaining part of this section will further detail the steps for the METAL 2 and STRUCTURE masks. The backside of the wafer is cleaned with acetone/methanol and dried. Using the AJA-ATC1800, 1.0 μm Al was sputter coated on the backside of the Si wafer. The Al layer was spin coated with PR1-2000 at 3000 rpm for 40 seconds and placed baked at 120° C for 60 seconds. The next lithography step using the METAL 2 mask is the most challenging of the four masks, which requires backside alignment. When performing a backside alignment, the patterned side is placed face down (this is done carefully not to scratch the Au bond frame) and the EVG aligner optics take a

snapshot of the backside of the wafer. This image is projected onto the monitor where the METAL 2 mask is then aligned, exposed for 4.2 seconds, and developed in RD6 developer solution for 40 seconds. After rinsing and drying, the wafer is inspected under the microscope. However, aside from checking for straight lines and pattern uniformity, the alignment cannot be checked since the backside of the wafer was un-patterned. After inspection, the wafer is post baked at 100 ° C for 60 seconds. The wafer was placed in Al etchant (Type A, Transene Inc.) at 50°C for 5 min to remove Al in all areas without PR1-2000. After visibly observing the Al was etched, the wafer was thoroughly rinsed and placed in a spin rinse dryer. The sample was inspected under the microscope and the photoresist was stripped from the Al and cleaned. The wafer was loaded and Bosch DRIE etched for 425 cycles and which, according to the etch rate should have etched ~ 315 μm for a ~ 340 μm thick wafer. Upon removing the wafer and inspecting it, visibly there was an error and further optical and SEM imaging verified this, which is shown in Figure 4-10 (a-c).

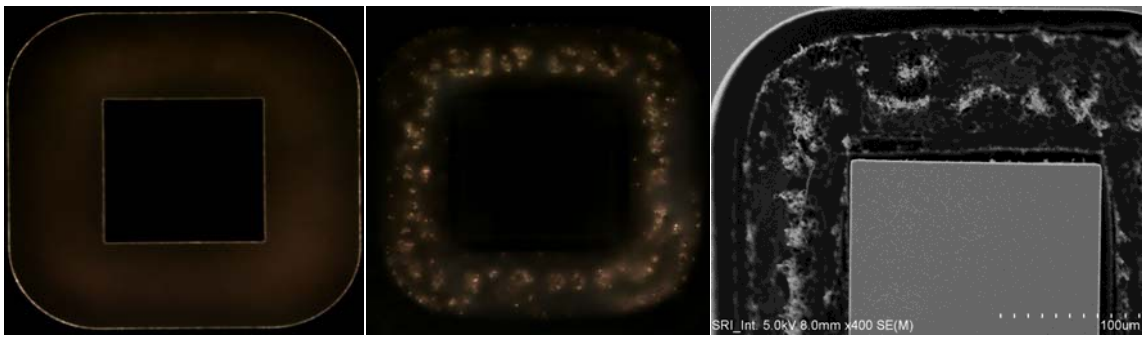

(a) (b) (c)

Figure 4-10: Inspection analysis of METAL 2 layer (a) dark field image focused on the silicon surface (b) image focused in the DRIE trench, showing non-uniform etching (c) magnified SEM image of the non-uniformed DRIE

After optical inspection and SEM analysis, there was micro-masking that resulted from incomplete etching of the Al in the DRIE trench areas. Processing several Si wafers in parallel (3 additional wafers with identical processing steps) allowed this part of the process to be repeated rather quickly, where the wafer was again placed in Al etchant for 5 minutes as before, rinsed, dried, and inspected again. After inspection, the micro-masking resulting from remaining traces of Al was confirmed. The wafer was placed back in the Al etchant for an additional 4 minutes; it was rinsed, dried, and re-inspected to show the traces of Al were completely gone. The wafer was loaded and 425 Bosch DRIE cycles were ran which etched the backside Si ~ 315 μm. The etch approximation is coarsely determined by measuring the micrometer revolutions on an optical microscope. This technique is illustrated in Figure 4-11 (a-b), where the top surface in focus and when the focus is rotated ~ 315 μm the bottom of the DRIE trench comes into focus. The wafer was placed in Al etchant for 10 minutes to completely remove the Al hard mask, rinsed, and dried in the cascade dryer.

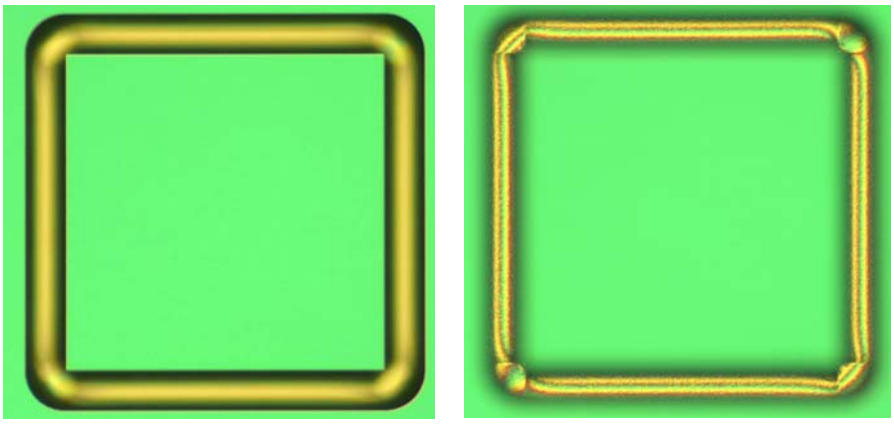

(a) (b)

Figure 4-11: 425 cycle Bosch DRIE (a) DRIE trench focused on the top surface (b) DRIE trench focused on the bottom surface after ~ 315 μm micrometer revolutions on the optical microscope

The last photolithography step uses the STRUCTURE mask to define and etch the spring/proof mass structures on the front-side of the wafer. Currently, on the front side of the wafer are the SW gratings and the Au bond frame, and on the backside are ~ 315 μm deep trenches. This mask will DRIE etch the remaining silicon from the front of the wafer until the spring/proof mass structures are completely release.

The front side of the wafer was spin coated at 3000 rpm with PR1-2000 for 40 seconds and placed on the hotplate at 120° C for 60 seconds. The STRUCTURE mask was exposed for 4.2 seconds and developed in RD6 developer solution for 50 seconds. After rinsing and drying, the wafer was inspected in the optical microscope to check the alignment with the previous layers as shown in Figure 4-12 (a). After inspection, the wafer is post baked at 100° C for 60 seconds. Given the selectivity of photoresist mask in the DRIE and the number of cycles needed to etch completely through the remaining 25 μm of Si, it will be used as the hard mask layer. The next step placed the patterned wafer onto a Si carrier wafer with Cool-Grease™ and loaded for the final Bosch DRIE process of 75 cycles. Upon completion, the wafer was unloaded and it could clearly be seen that the wafer etched completely through the wafer. The Cool-Grease™ carrier wafer was removed and the substrate was soaked in acetone/methanol, IPA, and DI water baths. After this thorough cleaning, the wafer was inspected with the optical microscope and the SEM seen in Figure 4-12 (a-d). In Figure 4-12 (c-d), there appears to be patterns on the proof mass, but, these are artifacts of aliasing of the short period gratings called moiré fringes.

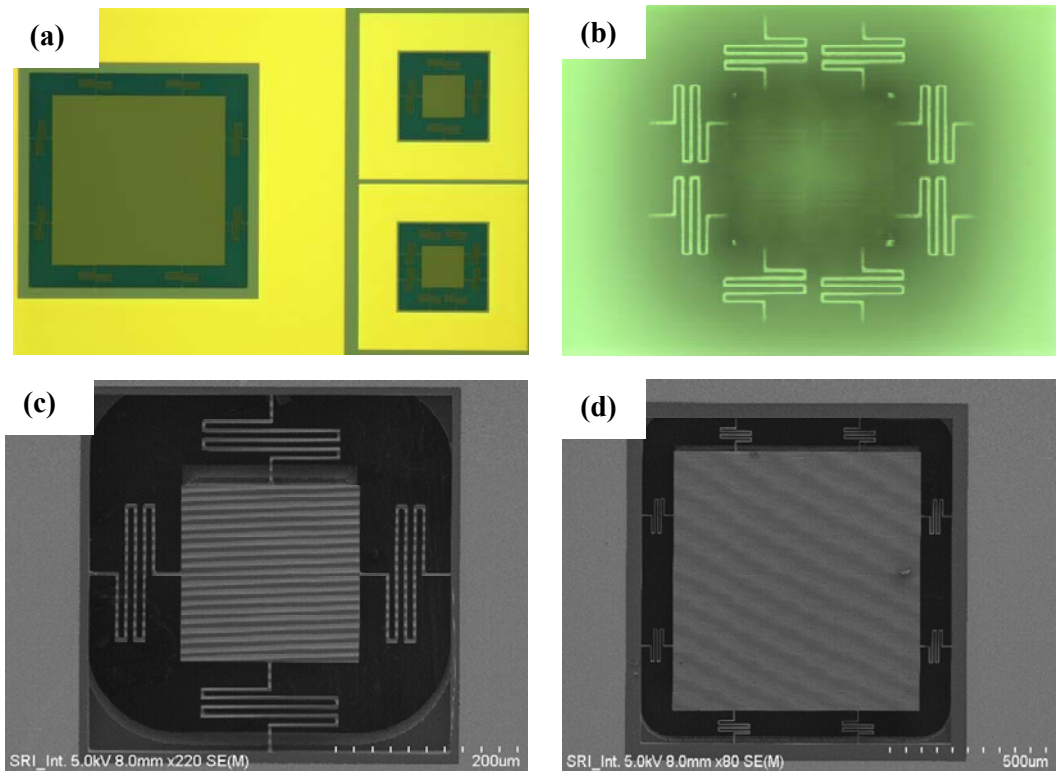

Figure 4-12: Inspection analysis of STRUCTURE layer (a) Optical image of the spring/proof mass layer before DRIE (b) Optical image in dark field mode clearly showing the through wafer DRIE with defined springs and membrane (c) SEM image of a completely released accelerometer (d) SEM image of another released accelerometer

To protect the accelerometer devices during dicing, photoresist was manually applied with a dropper onto the complete micromachined MEMS accelerometer parts and oven baked at 80°C for 10 min. The wafer was diced into the same 7 mm x 7 mm chip sizes as the glass lids. The chips were then soaked in acetone/methanol to remove the dicing debris and photoresist. The individual chips were placed on a bare Si wafer and descummed for 10 minutes in O_2 plasma in the Tepla and then in IPA. Then, the chips were dried in an oven at 80°C for 10 minutes and prepared for chip level bonding. A schematic view of the complete bulk Si accelerometer process flow is shown in Figure 4-13 (a-h).

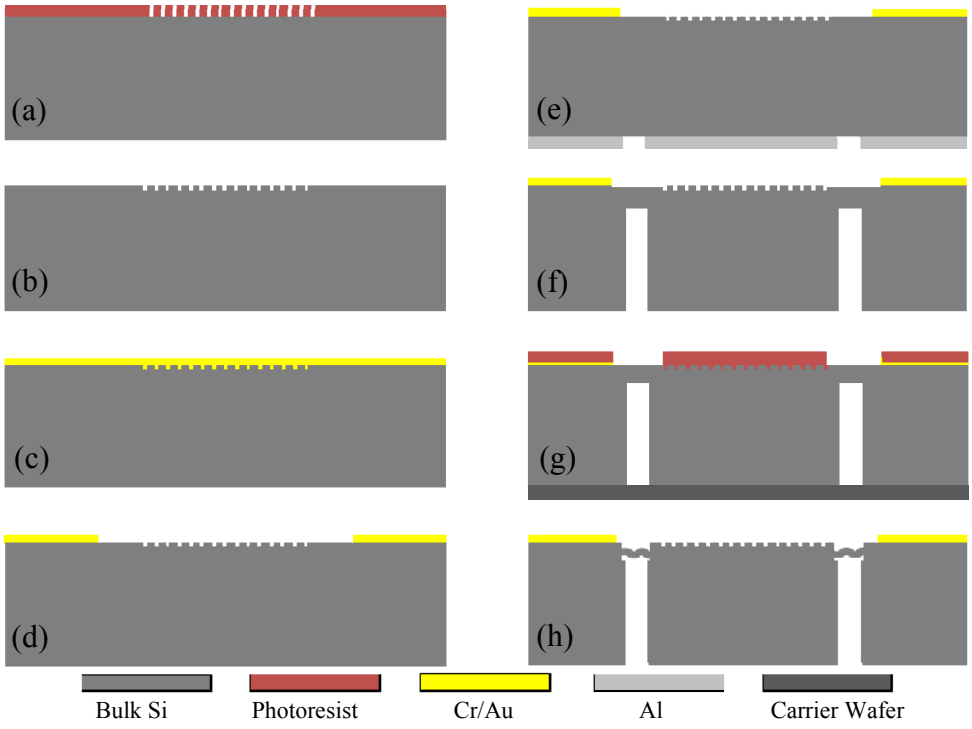

Figure 4-13: Schematic process flow of the bulk Si accelerometer device (a) INDENT mask patterned to define the SW gratings (b) SW grating etched into the Si substrate (c) Sputtered Cr/Au for Au bond frame (d) Patterning of the METAL 1 mask and wet etching the Cr/Au defining bond frame (e) Backside sputtering, patterning of METAL 2 mask, and wet etching of Al for bulk Si DRIE etch (f) Al strip and DRIE etch (g) STRUCTURE mask to define the spring/proof mass (h) DRIE of STRUCTURE mask

The last step to fabricating the coupled SW grating is to bond the glass lid and the bulk Si accelerometer chips together. This is done using a Finetech flip chip bonder. The first step in this Au:Au theromcompression bonding procedure is aligning chips together. The glass lid is carefully placed downward on the bond tool's air chuck and the vacuum lever is lowered picking up the chip. The Si accelerometer chip is carefully placed on the chuck and the lever with the glass chip is lowered. This engages the microscope objectives to allow for aligning the bond frames. This alignment is a tedious procedure, where X, Y, θ adjustment knobs are used for fine movements. When the chips are aligned the lever is lowered and the vacuum switch is disengaged and the glass lid is

aligned to and resting on the bulk Si accelerometer chip. Next, 80 N of force is applied on the sample and the chips are bonded the chips together at 320 ºC bonding temperature for 10 minutes. The fully processed glass lids, the bulk Si accelerometer chips, and the effective grating period of the coupled SW gratings are shown in Figure 4-14 (a-d).

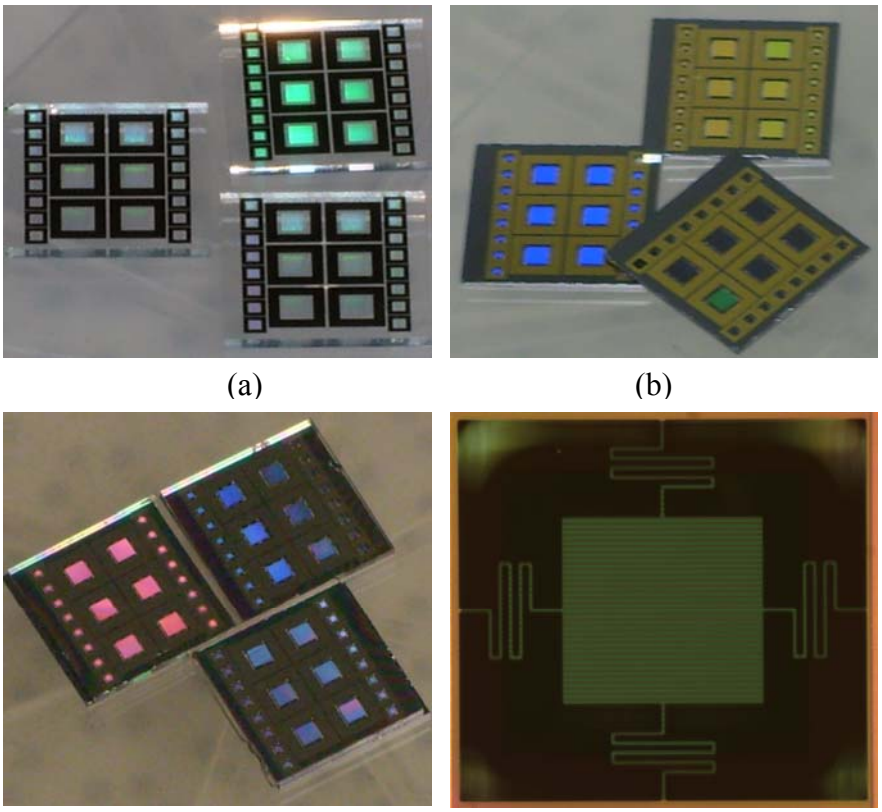

(a) (b)

(c) (d)

Figure 4-14: 7 mm x 7 mm square accelerometer components (a) Optical image of the glass lid with SW gratings before bonding (b) Optical image of the bulk Si accelerometer (c-d) Complete coupled SWG accelerometer after Au:Au TC bonding

On the completed grating accelerometer devices, the RIE-etched grating thickness on the glass wafer was 0.3 μm, with a 1.2 μm period. The DRIE-etched grating in Si was 0.12 μm deep with both 1.0 and 1.4 um period gratings used. The Cr/Au bonding metal thicknesses on Si and glass wafers was ~0.30 μm, yielding an estimated inter-grating gap

during zero acceleration of ~0.60 μm. Optical images of a completed Si spring/proof mass structures, glass lids, and bonded accelerometers are shown in Figure 4-14 (a-d)

The total system signal and noise analysis, the accelerometer testing setup, and testing the coupled SW grating will be detailed in Chapter 5.

Chapter 5

System Analysis, Test Setup, and Accelerometer Testing

5.1 Introduction

Sensors are only as good as their performance. This performance is directly related to the noise and signal quality of the device and the total system. In this chapter we will present the results of the total system analysis of the coupled SW grating accelerometer. Using the optical simulations and spring force analysis from Chapter 3, the total system noise, including the noise generated from the germanium photodiode, sensitivity, and displacement detection resolution of the couple SW grating MEMS accelerometer is calculated.

Our approach to testing the accelerometer system uses the simulation concepts introduced in Chapter 3, where the gap separation is varied between the SW gratings. The foundation of the accelerometer testing requires correlation of the output intensity from the simulation results, with the measured output intensity. We configured a test setup, where the accelerometer device is enclosed in a rigid cage system and placed on a subwoofer speaker. The assembly components will be discussed in more detail later in this chapter.

Additionally, the testing results of the coupled SW grating MEMS accelerometer are presented. The manually configured test setup consists of a rigid cage system

assembly mounted on the center of a 12" subwoofer. A known signal is applied to the subwoofer and using simple algebra, the signal is converted to a force. The coupled SW grating accelerometer is mounted inside the cage assembly on the subwoofer, where the force applied to the accelerometer device causes it to move, thus inducing evanescent wave coupling and increasing the output intensity as the gratings become closer. The testing and simulation results will be compared, where the overall total system assessment will be described in detail.

5.2 Accelerometer System Analysis

The optical simulations performed in Chapter 3 were completed varying the following parameters: grating thickness and period (to determine efficiency of various designs), the gap separation between the gratings (to determine sensitivity), and the incident laser source beam width (to determine the optimum spot size that interacts with the coupled gratings). These parameters were obtained to achieve the highest output intensity in the 1st diffraction order. The simulation results were normalized to 1 mW (the actual input) and used to calculate the signal to noise ratio and estimate the sensitivity of the coupled SW grating accelerometer. There are two types of noises that are attributed with photodiodes, Johnson noise (I_{jn}) and shot noise (I_{sh}). We used noise figures from commercially-available Ge photodiodes (Thorlabs S122C). The Johnson noise in photodiodes is attributed to the shunt resistance in the photodiode, which is used to determine the noise current. The Johnson noise is determined by:

$$I_{jn} = \sqrt{\frac{4 \cdot k \cdot T \cdot B}{R_{sh}}} \tag{32}$$

where k = 1.38 x 10^{-23} J/K is the Boltzmann Constant, T = 303.15 K is the temperature, B = 15 Hz is the noise measurement bandwidth, R_{sh} = 3.0 kΩ is the shunt resistance of the photodiode and receiver, and R_λ = 0.98 A/W is the responsivity, which measures the effectiveness of the conversion of light power into electrical current. The shot noise (I_{sh}) is noise generated from random fluctuations and is determined by:

$$I_{sh} = \sqrt{2q \cdot (I_d + I_{ph}) \cdot B} \tag{33}$$

where q = 1.6 x 10^{-19} C is an electron's charge, I_d = 0.5 μA is the photodiode dark current, I_{ph} = 980 μA is the generated photocurrent (diffracted light power * R_λ), and B = 15kHz is the noise measurement bandwidth. When the gap separation changes between the coupled gratings, the shot noise value is calculated at each grating gap separation because the output intensity is different at each gap separation. However, the output intensity units from the simulations are in arbitrary units (a.u.), and are normalized to 1.0 mW input to reflect the output intensity in power (W). The total noise of the photodiode is the root squared sum of the Johnson and shot noise:

$$I_{ph_{tot}} = \sqrt{I_{sh}^{\,2} + I_{jn}^{\,2}} \tag{34}$$

From the calculations in Table 5-1, it was concluded that the majority of the total system noise results from shot noise from the commercial germanium photodiode (Thorlabs S122C).

Table 5-1: Noise related calculations

		Output intensity (W)	Photocurrent I_{ph} (A)	Shot noise I_{sh} (A/√Hz)	Johnson noise I_{in} (A/√Hz)	Total noise $I_{sh(tot)}$ (A/√Hz)
		1.0 E-3	980E-6	68.6E-12	8.6E-12	69.1E-12
Gap Noise	0 nm gap	227.7E-6	223.1E-6	32.8E-12	11.2E-12	33.9E-12
	100 nm gap	101.3E-6	99.3E-6	21.9E-12		23.5E-12
	200 nm gap	46.4E-6	45.5E-6	14.9E-12		17.2E-12
	300 nm gap	43.0E-6	42.2E-6	14.3E-12		16.7E-12
	400 nm gap	25.6E-6	25.1E-6	11.1E-12		14.0E-12
	500 nm gap	16.9E-6	16.5E-6	9.0E-12		12.5E-12
	600 nm gap	12.2E-6	12.0E-6	7.7E-12		11.6E-12

The sensor sensitivity is calculated as the derivative of the 1.0 mW-normalized output power vs. grating separation in Figure 5-1(a). The values of the gap separation were substituted into the derivative of the curve fit equation, ($dy/dx=1.5346*e^{-0.004}*$gap separation$*-0.004$) where Figure 5-1 (b) shows the sensor sensitivity for the simulations summarized in Figure 5-1 (a) (curve fit equation is shown). The sensitivity and S/N ratio in Figure 5-1 (b-c) are highest at the zero grating separation, but this would be an ineffective sensor, as it would not allow any mechanical movement about this bias point. This point would be when the gratings are touching, so in practice a non-zero gap is required.

Selecting a 300 nm initial gap, where sensitivity is approximately 420.94E-9 W/nm and using the Thorlabs *S122C Ge* photodiode's noise figures, 40.5 pm/√Hz minimum detectable signal is predicted in Table 5-2.

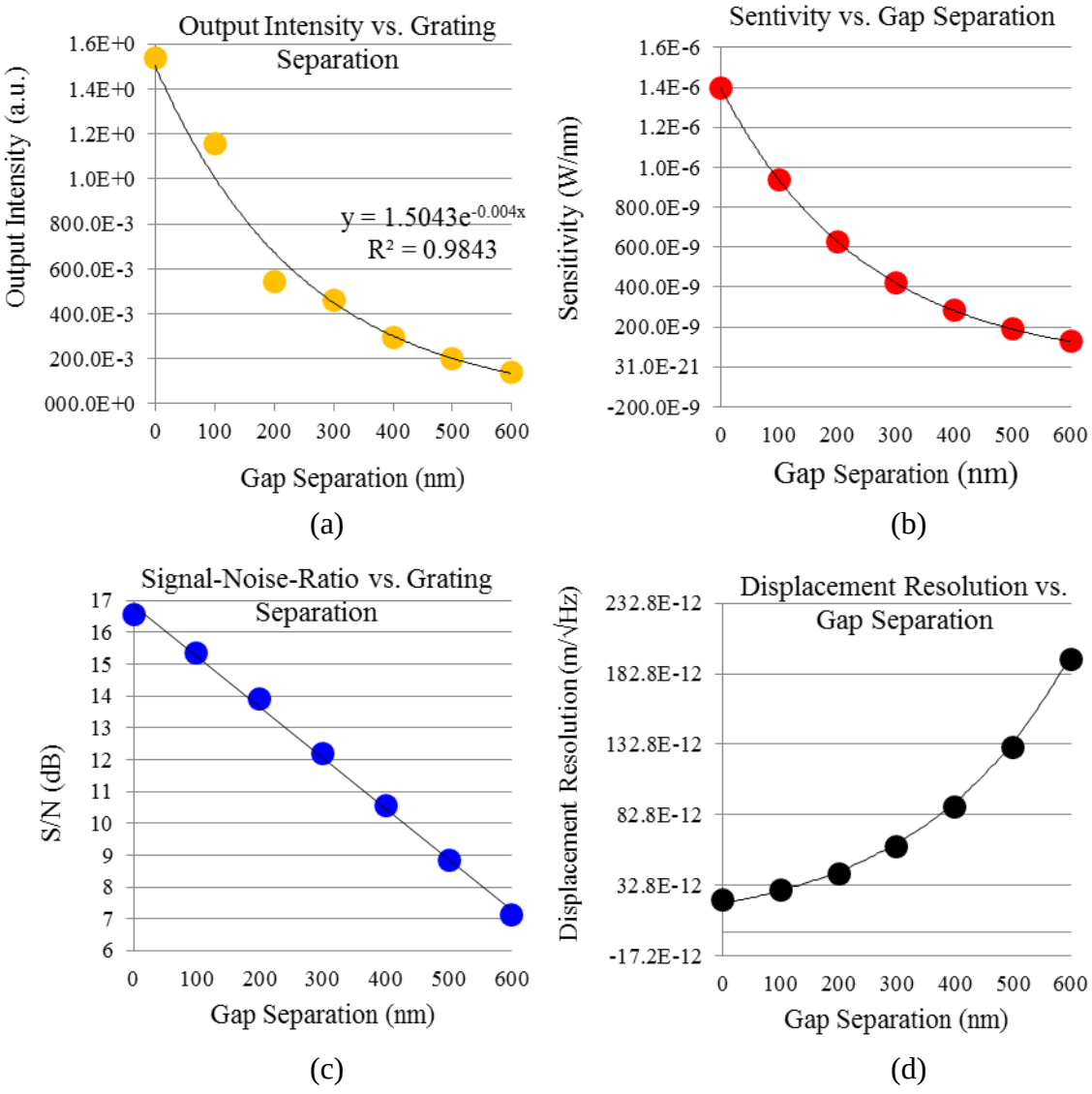

Figure 5-1: System analysis of 1.2 µm x 1.0 µm coupled pairs (0.4 µm thick in glass and 0.21 µm grating in Si) (a) 1st D.O. output intensity versus grating separation (b) Plot of sensitivity (change in optical output versus nm deflection) of coupled-grating sensor calculated at various grating gaps (c) S/N ratio at different grating separations (d) Calculated displacement resolution which shows the smallest detection at the 0 nm gap

Table 5-2: Signal-to-noise and minimum displacement sensitivity estimates based on comparison of sensor sensitivity and photocurrent-induced noise.

Gap (nm)	**d_{out}/d_{gap}** (a.u./nm)	**sensitivity** (W/nm)	**sensitivity** (A/nm)	**noise** (A/√Hz)	***S/N Ratio***	**dB**	**Displacement Resolution** (m/√Hz)
0	6.1E-3	1.4E-6	1.4E-6	33.9E-12	40.4	46.1	24.7E-12
100	4.1E-3	936.8E-9	918.1E-9	23.5E-12	39.0	45.9	25.6E-12
200	2.8E-3	628.0E-9	615.4E-9	17.2E-12	35.9	45.5	27.9E-12
300	1.8E-3	420.9E-9	412.5E-9	16.7E-12	24.7	43.9	40.5E-12
400	1.2E-3	282.2E-9	276.5E-9	14.0E-12	19.7	42.9	50.7E-12
500	830.7E-6	189.1E-9	185.4E-9	12.5E-12	14.9	41.7	67.3E-12
600	556.9E-6	126.8E-9	124.2E-9	11.6E-12	10.7	40.3	93.1E-12

This figure of merit is similar to the state-of-the-art tunneling and capacitive readout type sensors [13, 35], but with the benefit of electromagnetic interference rejection and fast readout rates offered by our optical devices. In comparison to other optical accelerometer devices [29, 31], our detectable signal is three orders of magnitude less. This is a result of the increased noise from the available detector used. Initial estimations using an OSI *FCI-InGaAs 55* photodiode's noise figures, 10 fm/√Hz minimum detectable signal was predicted. Using a different detector will allow or minimum signal detection to be comparable with the similar to the state-of-the-art optical devices.

5.3 Accelerometer Test Setup

Stability was the primary consideration in designing the test setup. We wanted to ensure that the test fixture was rigid enough and when a force is applied the system it would not move around or rattle.

There were several components that were obtained from Thorlabs, Inc. to create the cage system for the accelerometer device. The image in Figure 5-2 shows the cage system components.

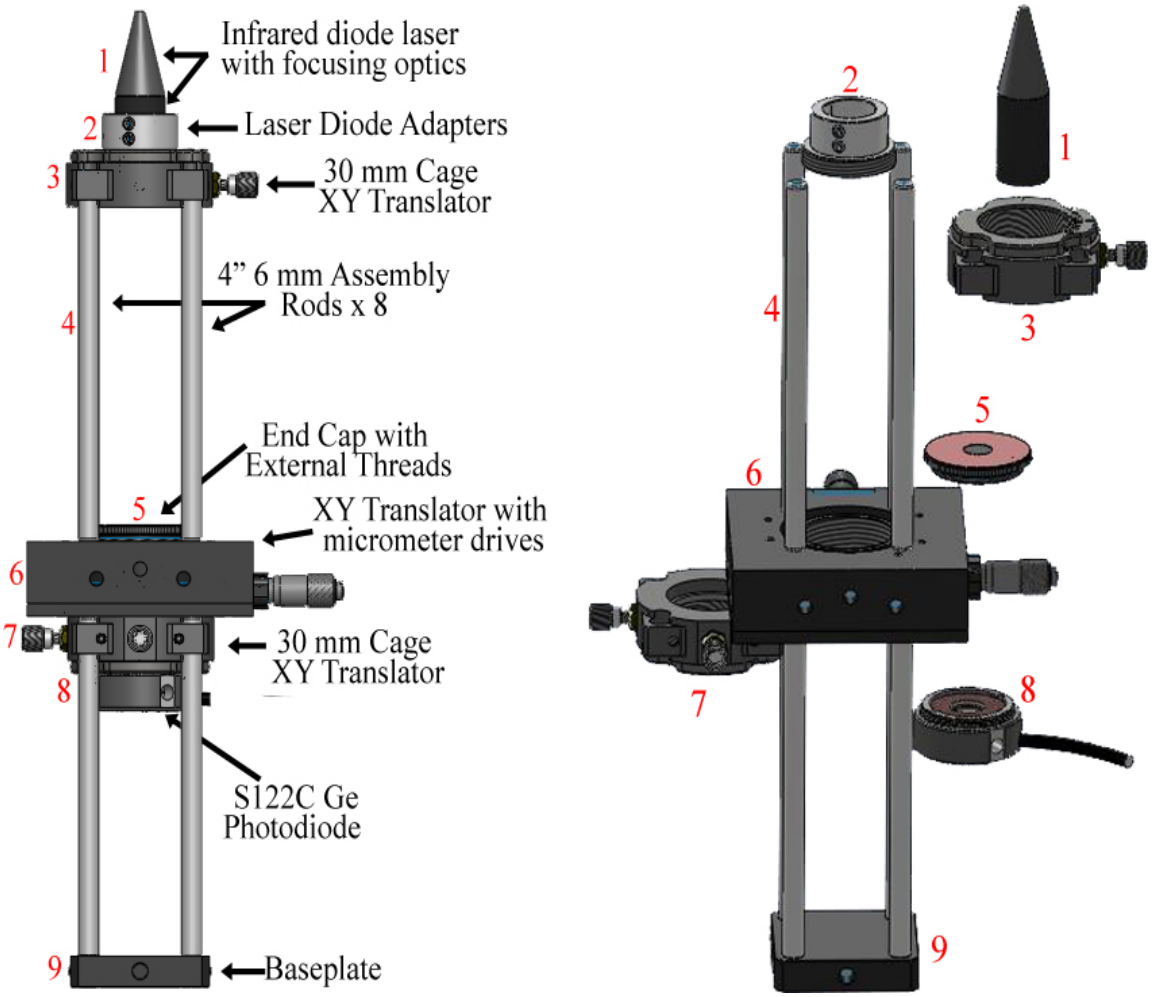

Figure 5-2: Cage system for accelerometer test setup (a) completely assembled cage system with component labels (b) Exploded 3D view of the cage system

The skeleton of the cage assembly is supported by eight 4" rods with #4-40 studs that screw into the XY Translator with micrometer drives. A hole, approximately 8.5

mm in diameter was drilled in the center of the end cap, where the accelerometer was mounted, and was screwed into the threaded side of the XY translator with micrometer drives. This micrometer drives offers ± 6.4 mm of XY travel manipulated by 0.5 mm per revolution fine pitch adjusters, which allows the entire accelerometer device to move to the incident location of the laser as shown in Figure 5-3.

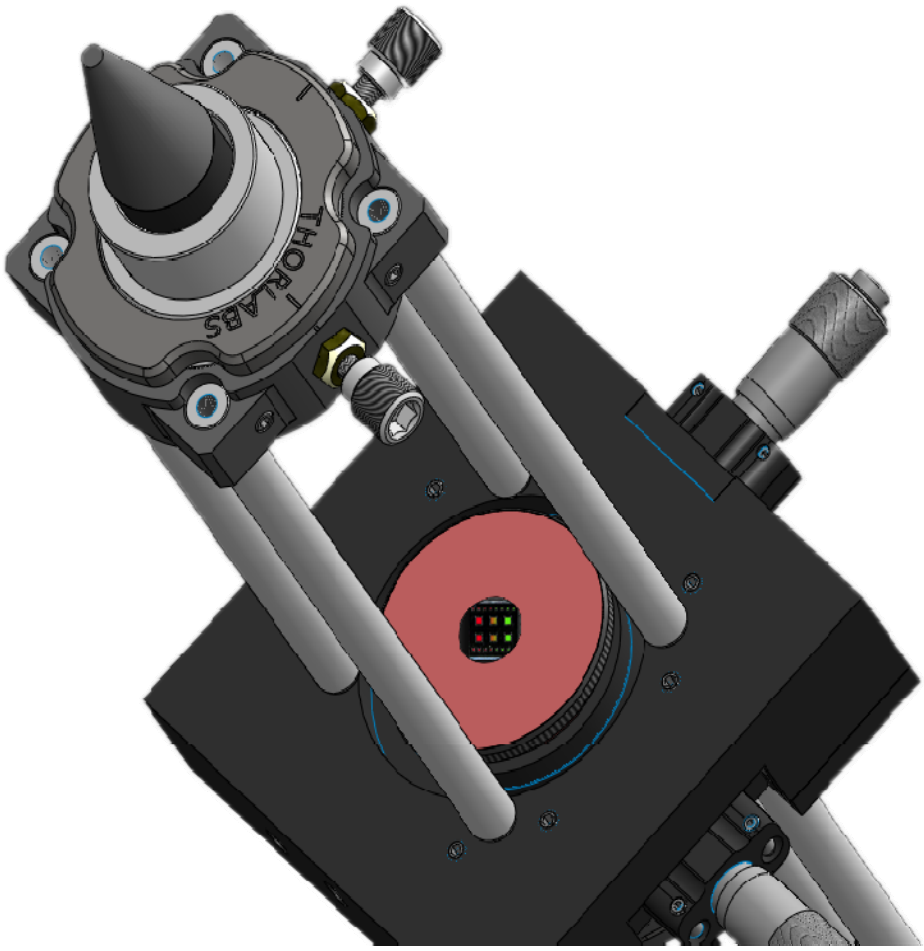

Figure 5-3: Cage system showing the mounted accelerometer device on the XY translation stage that moves the accelerometer to the specific accelerometer locations

Next, the bottom half of the cage is assembled. The threaded germanium IR photodetector (Thorlabs S122C) is screwed into the threaded side of the 30 mm cage XY

translator, which provides ±1 mm of travel perpendicular to the optical axis of a cage system, and is slid through the 4" rods. This XY translator allows movement of the photodiode to the location of maximum output intensity produced from the laser. The bottom base plate is then slid through the four bottom 4" rods and tightened. With the base stable, the top portion of the cage was configured by screwing the threaded adaptor into the other 30 mm cage XY translator, which is used to position the laser. The single mode 1.55 μm IR semiconductor diode laser (Mitsubishi ML925B45F) with focusing optics (Thorlabs LT230260P-C) was then fitted and tightened into the adaptor. The focusing optics is comprised of two aspheric lenses for focusing the beam to a small spot size. The first lens that the laser passes through has a numerical aperture (NA) of 0.55 to collimate the divergent beam emitted from the laser. The second lens has a NA of 0.25 to focus the light down. The lens pair is fixed within a threaded mount lens holder which allows adjustment of the lens' position to extend the beam's point of focus. The normal distance between the laser and the optic pair is 2.5 mm.

The instrumentation associated with the cage assembly setup includes a laser diode driver (Thorlabs LDC201CU) operating in a constant optical power mode and two power and energy meters (Thorlabs PM320E and PM100USB) which converts the signal from the photodetector and transfers it to the connected PC using a high-speed USB 2.0 connection to display the output power reading. They both have a selectable bandwidth of 15 Hz for photodiodes, but the PM320E has an analog output to connect to an oscilloscope. Lastly, the commercial accelerometer (ADXL204-EB), was mounted to the final cage assembly, was used as a reference. The part of the test setup that applies the force to the accelerometer device is the subwoofer assembly. This part of the setup

consists of the following: a 10” subwoofer (10" - 300 Watt - 35 - 1000 Hz - 4 Ohm - Sony XS-GTX110LW); a 300W MOSFET Class D subwoofer amplifier (Infinity REF311A); 10 MHz DDS function generator (Wavetek Model 29); a DC power supply (HP-E3612A); a digital phospor oscilloscope (Tektronix TDS 3052). This equipment is shown in Figure 5-4.

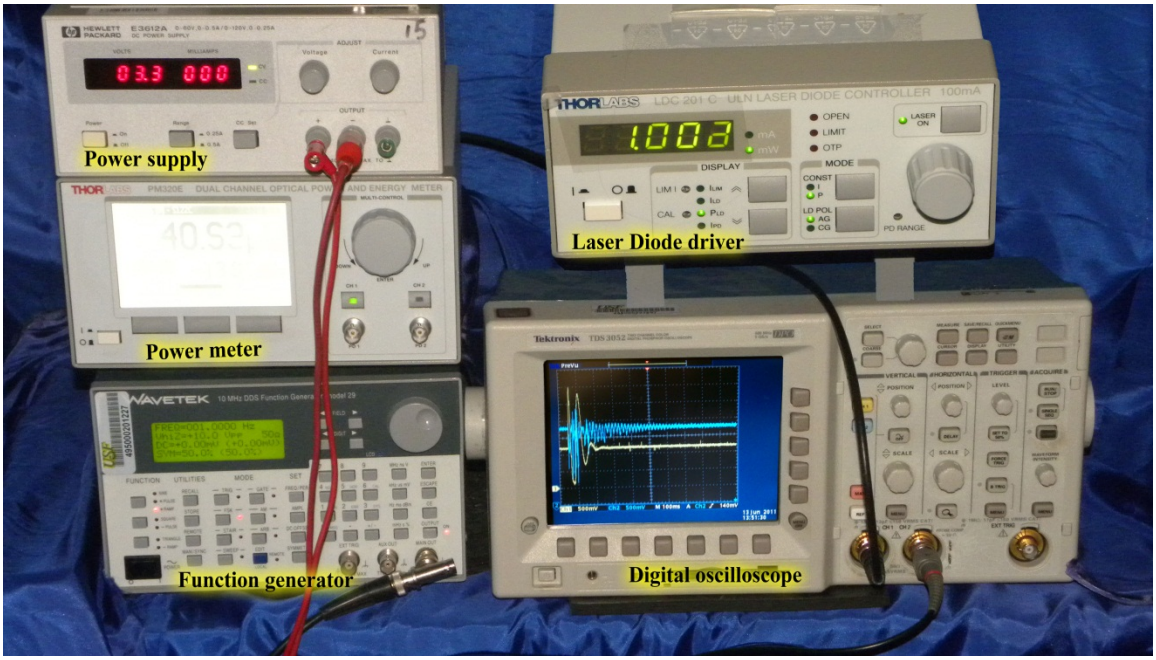

Figure 5-4: Electronic equipment used for accelerometer test setup

The power supply was used to apply 3.3 V to the commercial accelerometer; the photodiode was connected to the power meter to convert the photodiode signal and transfers it to the computer; the laser diode was connected to the laser diode driver to control the input power; the function generator supplied a sinusoidal frequency and amplitude voltage input to the subwoofer amplifier, which was then routed to the subwoofer; and a coaxial cable was connected from the power meter to the oscilloscope

to view the signal generated from the coupled SW grating accelerometer and from the commercial accelerometer. The completed assembly is shown in Figure 5-5.

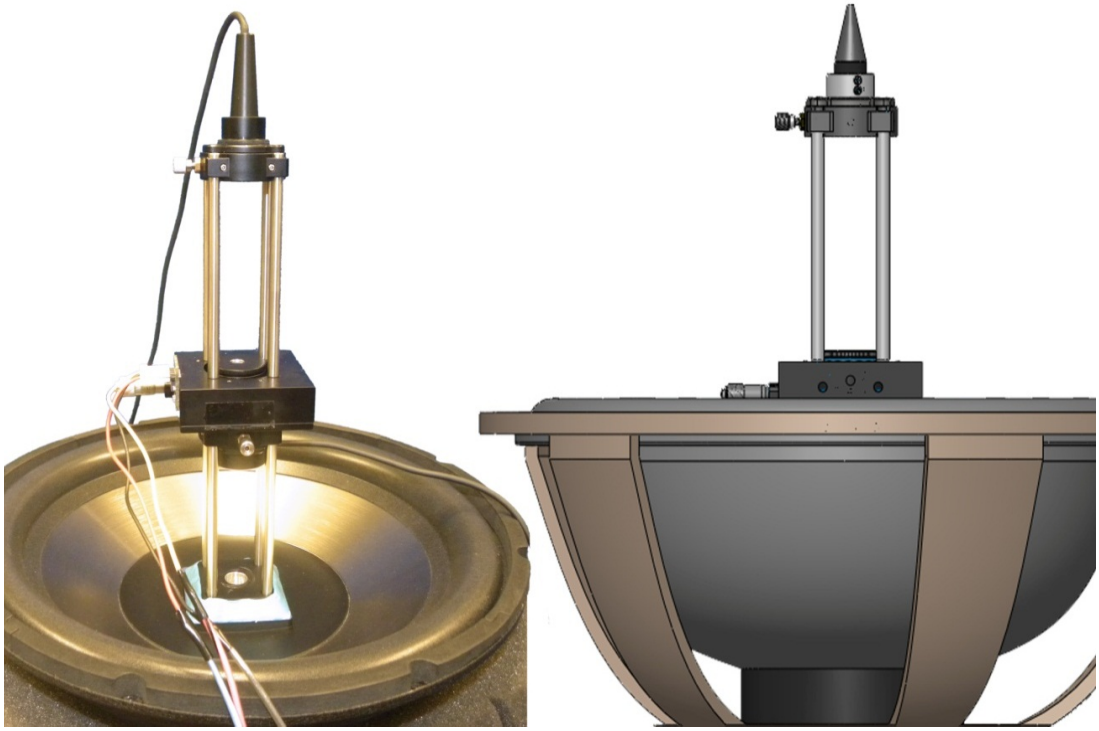

(a) (b)

Figure 5-5: Completed test setup (a) actual assembly with mounted commercial accelerometer (b) 3D rendering of the test setup

5.4 Coupled SW Grating Accelerometer Testing

The test setup is assembled, both the commercial and the coupled SW grating accelerometers are mounted to the cage system, and the simulations in Chapter 3 provide the baseline for the expected output intensity. First, we connected the instruments described in section 5.3 and confirmed the subwoofer's response to the sinusoidal input from the function generator. Second, using the commercial accelerometer as a reference, the acceleration was calculated by taking the second derivative of the input signal from the function generator (d^2x/dt^2).

$$input\ signal: \quad x = A \cdot \cos(2\pi \cdot f \cdot t)$$
$$acceleration: \frac{d^2x}{dt^2} = -A \cdot 4\pi^2 \cdot f^2 \cdot \cos(2\pi \cdot f \cdot t) \tag{35}$$

where A is the amplitude and f is the frequency at some time t. Afterwards, the commercial accelerometer was mounted on the cage system and the IR laser was incident on the coupled SW grating device to show diffraction from EW coupling. In the cage setup, the IR laser source and the coupled SW grating device were separated by approximately 50 mm to focus the beam to a fine spot (approximately 15 – 20 μm) centered on the coupled SW gratings. The output intensity was measured by the IR photodetector and was placed 25 mm from the coupled SW grating sample, with a 2 mm rectangular slit to block stay light and capture only the single 1st diffraction order. The EW coupled diffraction and the rectangular slit are shown in Figure 5-6 (a, b).

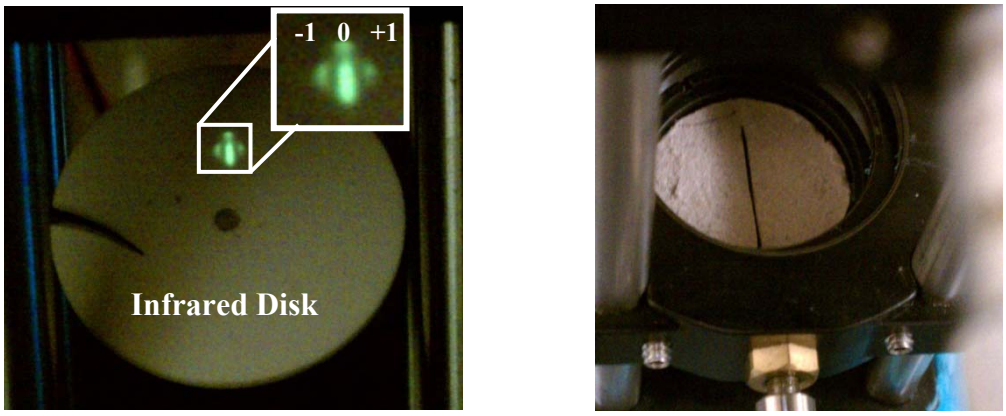

(a) (b)

Figure 5-6: (a) EW coupled diffraction shown on an IR card (b) 2 mm rectangular slit used to isolate individual diffraction orders

To verify the accuracy of the photodetector output, the coupled grating accelerometer was removed and the laser was focused directly into the photodetector. A constant power input was set to 1.0 mW and the photodetector output showed an output value of 0.98 mW. Additionally, when the laser is normally incident upon the bonded glass and silicon

interface, without gratings, the transmitted output power was measured to be 0.58 mW. This decrease in output intensity is a within 2% of the expected value due to Fresnel reflections at the Si:air, Si:glass, and glass:air interfaces (31%, 16%, and 4% respectively). The six different SW grating accelerometers (4spring and 8 spring- 100 µm, 150 µm, 200 µm length spans) were tested by applying a 10 and 20 Hz sinusoidal waveform with voltage amplitudes of 2V: 2V: 10V using the function generator, for fifteen total tests on each accelerometer device. As each device was tested, the photodetector connected to the power meter recorded the output intensity before the subwoofer was enabled (at rest), when the speaker was on (applied force), and after the speaker stopped (at rest). The output intensity recorded by the photodetector is output to the digital phosphor oscilloscope and the data is logged to the computer via USB connection computer shown in Figure 5-7.

The USB data logger interface controls several parameters which include the sampling rate, bandwidth, and averaging. The sampling rate was set to record 100 data

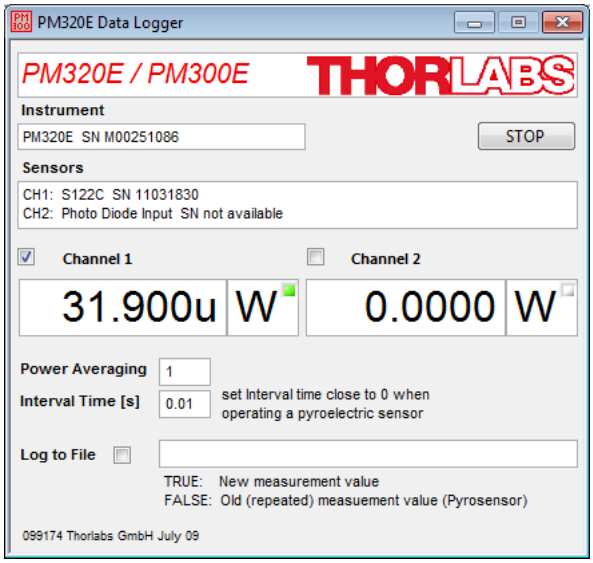

Figure 5-7: (a) USB data logging interface

points per second (100 Hz). There are two available bandwidth settings for all the power meter models from Thorlabs, Inc., low (15 Hz) and high (100 kHz), where the manufacturer's suggestion to use the low setting for continuous wave power.

Lastly, the logged data was individually recorded and not averaged. These parameters were set and the six accelerometer spring designs were tested using the subwoofer, where the results are shown in Figure 5-8.

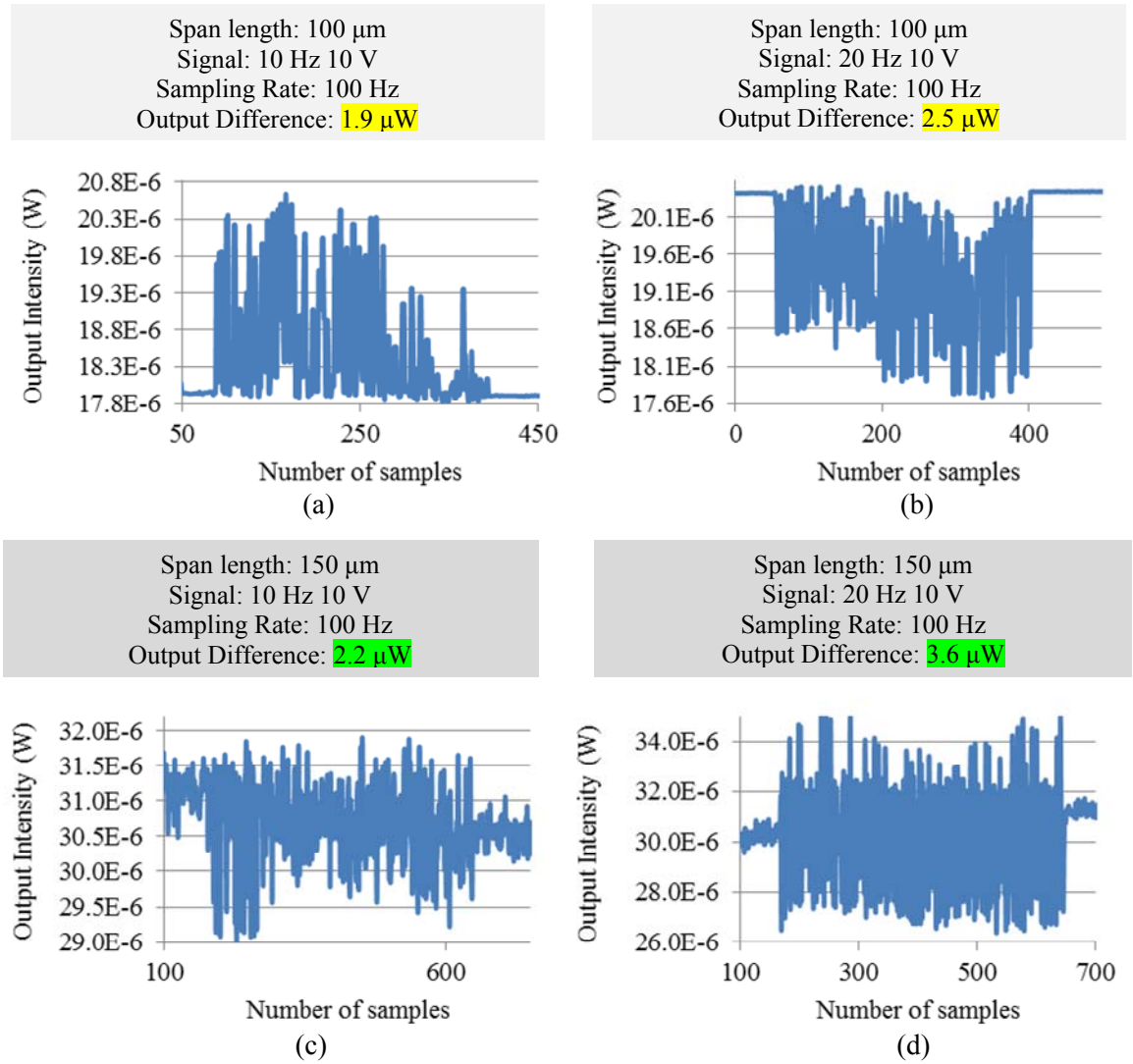

Figure 5-8: Output intensity difference of the 4-spring/proof mass membrane using a 10 and 20 Hz 10 V sinusoidal signal sampled at 100 Hz (a) 100 µm span length at 10 Hz (b) 100 µm span length at 20 Hz (c) 150 µm span length at 10 Hz (d) 150 µm span length at 20 Hz (e) 200 µm span length at 10 Hz (f) 200 µm span length at 20 Hz

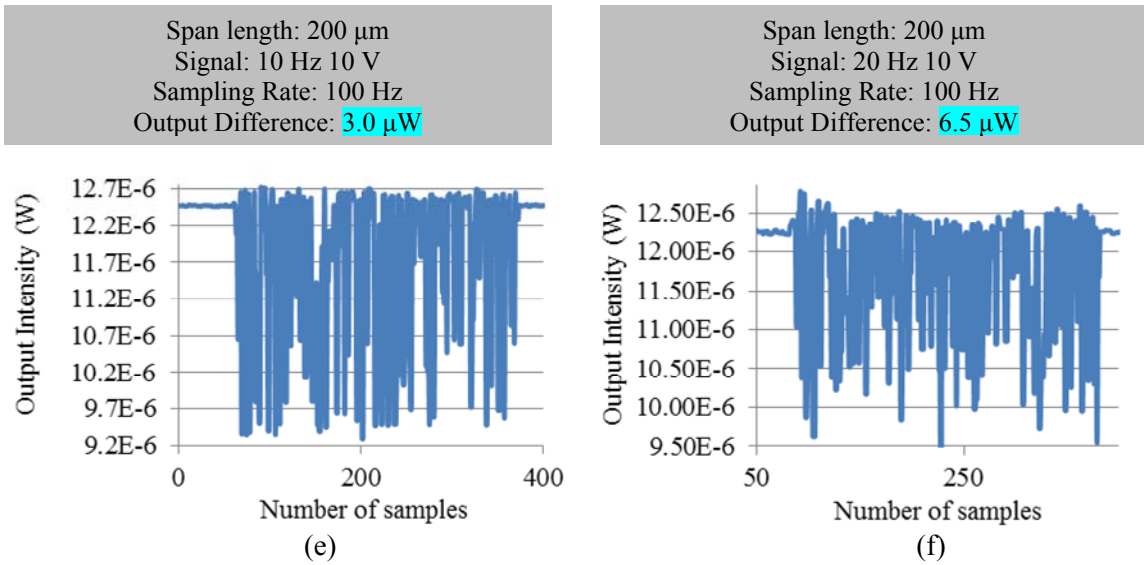

Figure 5-8 (Continued)

In Figure 5-8 (a-f) the output intensity difference was observed from the applied 10 Hz and 20 Hz sinusoidal wave with a 10 V amplitude signal. It can be seen in Figure 5-8 when the speaker is on and off. In each graph you can see a straight line at the beginning and towards the end; this indicates when the speaker is off. In contrast, there is a large signal that is in the center; this indicates when the speaker is operating at the specified frequency with 10 V amplitude input. Furthermore, when Figure 5-8 is analyzed, a consistent trend can be seen. With the 4 spring/proof mass accelerometers, it can be seen that the output intensity increases as the spring length becomes larger and when the frequency increases, which denotes a greater applied force. The same results are observed for the 8 spring/proof mass accelerometers in Figure 5-9.

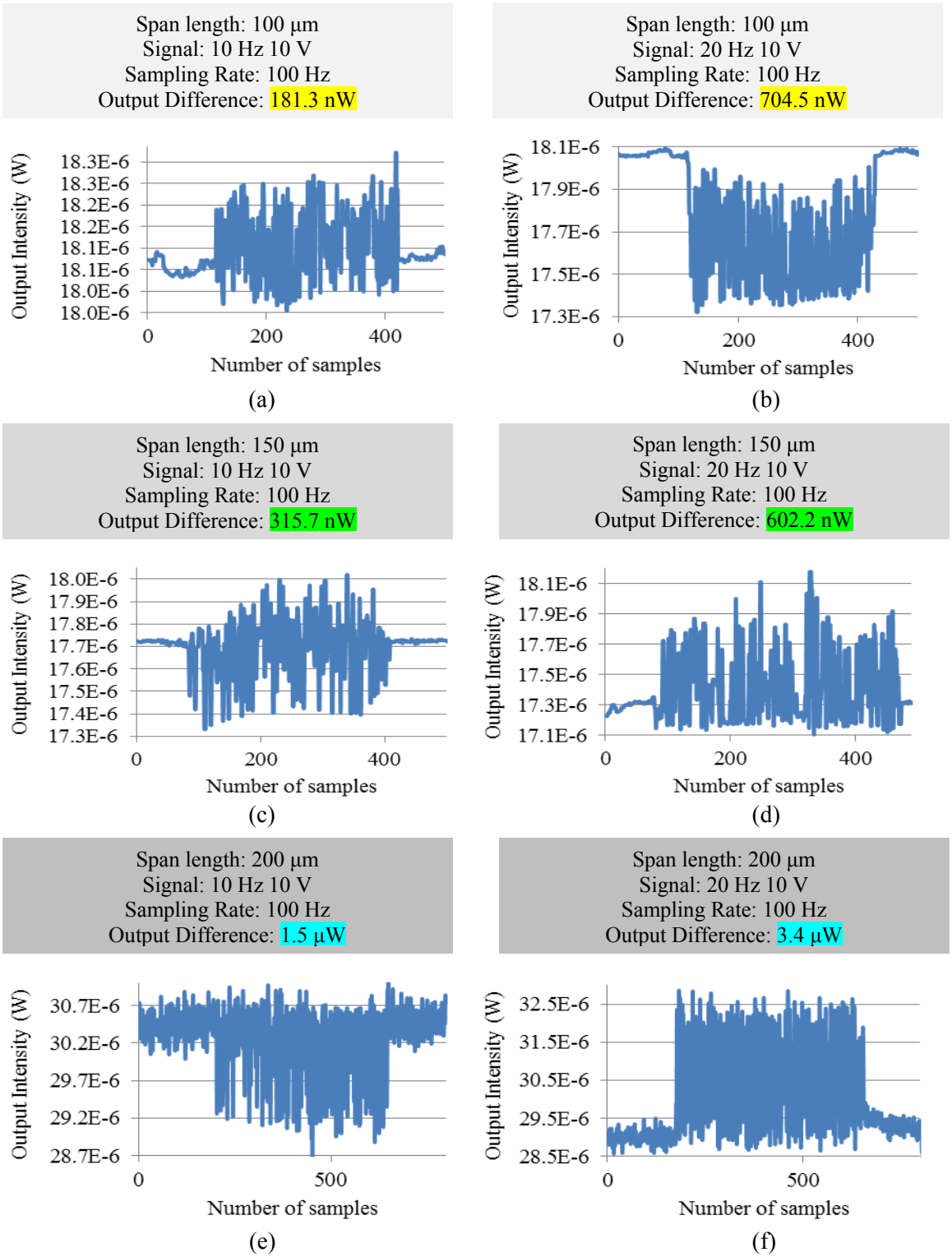

Figure 5-9: Output intensity difference of the 8-spring/proof mass membrane using a 10 and 20 Hz 10 V signal sampled at 100 Hz (a-b) 100 µm span length at 10 and 20 Hz respectively (c-d) 150 µm span length at 10 and 20 Hz respectively (e-f) 200 µm span length at 10 and 20 Hz respectively

As previously mentioned, there were two power meters that were used in which results from both are illustrated in Figure 5-8 and Figure 5-9. In order to utilize the analog output and monitor the real time output on the oscilloscope, the PM320E was used. Figure 5-9 (c-d) and Figure 5-9 (e-f) are results from the PM320E and the remaining graphs are from the PM100USB meter. Although the PM320E power meter is is a higher end meter and has many more functions (use for a variety of different sensors and operation modes), the PM100USB power meter results were just as accurate.

Again, the output intensity shown in Figure 5-8 and Figure 5-9 is obtained by taking the difference when the speaker is off (averaged on both sides) to when the speaker is on (averaged high point). The output intensity from the other tested devices using 10 Hz and 20 Hz frequencies with the varying amplitude voltage is included in Appendix B. To visually compare and contrast the coupled SW grating accelerometer, it was compared with a commercial device (Analog Devices ADXL-204CE) as seen in Figure 5-10. The signal used to apply a force to the speaker was a square waveform having a 0.25 Hz frequency and 5 V amplitude. The square waveform clearly provides an optical output response; however, a square waveform generates an infinite number of higher order harmonics and determining the maximum output intensity would be subjected to error.

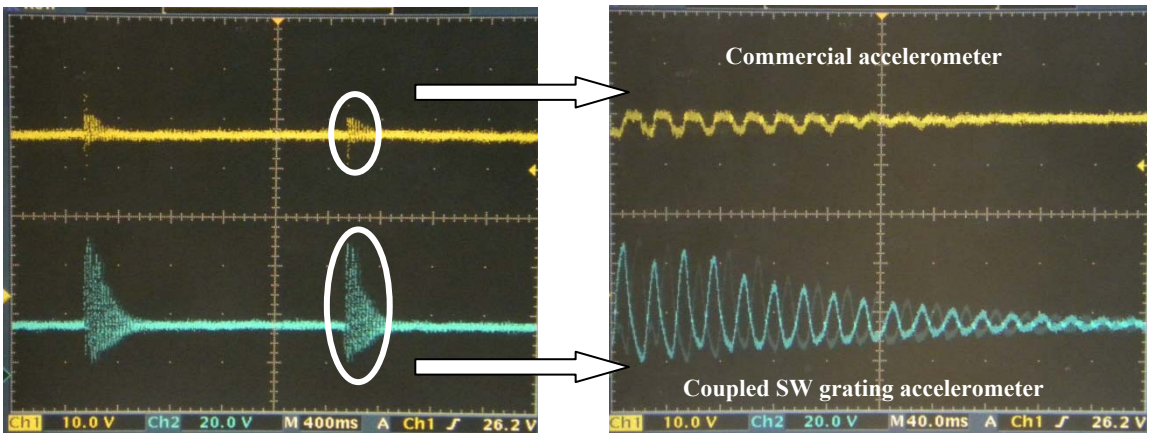

(a) (b)

Figure 5-10: Square waveform optical output response from a 0.25 Hz 5 V signal (a) screenshot of two responses (b) magnified view showing harmonic oscillation of coupled SW grating (bottom) and commercial (top)

The displacement obtained in Table 5-3 and Table 5-4 are referenced from the coupled SW grating simulations in Chapter 3, where the expected output intensity was determined from the simulated gap separations (0 nm to 1.0 μm). We know that as the gap separation changes, the output intensity changes. Specifically, when the gap separation becomes closer, the output intensity increases. Assuming the gap separation is 600 nm (the thickness of the bonded gold layers); the output intensity at that gap separation is known from the simulation results. This correlation between the simulations and measured output intensity enable estimation of the displacement versus change in output intensity. The estimated displacement from the 10 and 20 Hz signal with 2 V, 4 V, 6 V, 8V, and 10V amplitude is shown in Table 5-3 and Table 5-4.

Table 5-3: Measured output intensity and estimated displacement of the coupled SW gratings from the 4 spring/proof mass

4 springs at 10 Hz

100 µm span length

	2V	4V	6V	8V	10V
MAX (W)	17.9E-6	20.4E-6	20.4E-6	18.9E-6	19.8E-6
MIN (W)	17.9E-6	20.6E-6	20.6E-6	17.9E-6	17.9E-6
OUT Difference (W)	**26.9E-9**	**126.7E-9**	**188.3E-9**	**1.0E-6**	**1.9E-6**
Displacement (m)	**160.0E-12**	**3.9E-9**	**5.0E-9**	**33.0E-9**	**59.0E-9**

150 µm span length

	2V	4V	6V	8V	10V
MAX (W)	30.2E-6	30.1E-6	29.9E-6	29.1E-6	29.1E-6
MIN (W)	30.6E-6	31.1E-6	31.0E-6	31.2E-6	31.3E-6
OUT Difference (W)	**367.1E-9**	**863.7E-9**	**1.0E-6**	**2.0E-6**	**2.2E-6**
Displacement (m)	**11.5E-9**	**27.0E-9**	**32.0E-9**	**63.0E-9**	**69.0E-9**

200 µm span length

	2V	4V	6V	8V	10V
MAX (W)	11.5E-6	10.0E-6	10.1E-6	9.8E-6	9.4E-6
MIN (W)	12.1E-6	12.0E-6	12.3E-6	12.2E-6	12.4E-6
OUT Difference (W)	**692.4E-9**	**2.0E-6**	**2.2E-6**	**2.4E-6**	**3.0E-6**
Displacement (m)	**20.3E-9**	**61.5E-9**	**69.0E-9**	**76.5E-9**	**95.3E-9**

4 springs at 20 Hz

100 µm span length

	2V	4V	6V	8V	10V
MAX (W)	20.5E-6	20.2E-6	18.5E-6	18.4E-6	17.8E-6
MIN (W)	20.5E-6	20.5E-6	18.0E-6	20.1E-6	20.2E-6
OUT Difference (W)	**61.3E-9**	**339.5E-9**	**548.1E-9**	**1.7E-6**	**2.4E-6**
Displacement (m)	**1.9E-9**	**10.4E-9**	**17.2E-9**	**54.8E-9**	**77.0E-9**

150 µm span length

	2V	4V	6V	8V	10V
MAX (W)	29.8E-6	29.4E-6	29.3E-6	28.4E-6	27.1E-6
MIN (W)	30.4E-6	30.9E-6	31.0E-6	30.9E-6	30.8E-6
OUT Difference (W)	**563.9E-9**	**1.6E-6**	**1.8E-6**	**2.5E-6**	**3.6E-6**
Displacement (m)	**17.8E-9**	**50.0E-9**	**55.8E-9**	**79.0E-9**	**105.0E-9**

200 µm span length

	2V	4V	6V	8V	10V
MAX (W)	10.9E-6	10.5E-6	10.0E-6	7.8E-6	6.1E-6
MIN (W)	12.4E-6	12.5E-6	12.1E-6	12.6E-6	12.5E-6
OUT Difference (W)	**1.5E-6**	**2.0E-6**	**2.2E-6**	**4.8E-6**	**6.4E-6**
Displacement (m)	**45.9E-9**	**62.5E-9**	**67.9E-9**	**221.1E-9**	**229.6E-9**

Table 5-4: Measured output intensity of the coupled SW gratings from the 20 Hz signal with 2V: 2V: 10V amplitude

8 springs at 10 Hz

100 µm span length

	2V	4V	6V	8V	10V
MAX (W)	18.11E-6	18.09E-6	18.31E-6	18.31E-6	18.29E-6
MIN (W)	18.18E-6	18.22E-6	18.17E-6	18.15E-6	18.11E-6
OUT Difference (W)	**67.6E-9**	**127.2E-9**	**133.9E-9**	**159.9E-9**	**181.3E-9**
Displacement (m)	**2.1E-9**	**4.0E-9**	**4.2E-9**	**5.0E-9**	**5.1E-9**

150 µm span length

	2V	4V	6V	8V	10V
MAX (W)	17.63E-6	17.18E-6	16.96E-6	16.80E-6	17.40E-6
MIN (W)	17.65E-6	17.21E-6	17.21E-6	17.09E-6	17.72E-6
OUT Difference (W)	**20.3E-9**	**25.3E-9**	**248.4E-9**	**291.5E-9**	**315.7E-9**
Displacement (m)	**630.50E-12**	**795.00E-12**	**7.60E-9**	**9.10E-9**	**9.90E-9**

200 µm span length

	2V	4V	6V	8V	10V
MAX (W)	30.15E-6	30.00E-6	29.40E-6	29.10E-6	29.00E-6
MIN (W)	30.41E-6	30.36E-6	30.30E-6	30.36E-6	30.46E-6
OUT Difference (W)	**263.0E-9**	**357.2E-9**	**900.7E-9**	**1.3E-6**	**1.5E-6**
Displacement (m)	**8.1E-9**	**11.2E-9**	**28.1E-9**	**39.9E-9**	**46.0E-9**

8 springs at 20 Hz

100 µm span length

	2V	4V	6V	8V	10V
MAX (W)	17.95E-6	17.71E-6	17.45E-6	17.46E-6	17.34E-6
MIN (W)	18.07E-6	18.04E-6	17.99E-6	18.03E-6	18.04E-6
OUT Difference (W)	**130.0E-9**	**325.0E-9**	**543.5E-9**	**568.6E-9**	**704.5E-9**
Displacement (m)	**4.1E-9**	**10.1E-9**	**17.1E-9**	**17.9E-9**	**22.1E-9**

150 µm span length

	2V	4V	6V	8V	10V
MAX (W)	17.38E-6	17.38E-6	17.21E-6	17.84E-6	17.93E-6
MIN (W)	17.37E-6	17.34E-6	17.33E-6	17.34E-6	17.33E-6
OUT Difference (W)	**13.7E-9**	**44.0E-9**	**117.3E-9**	**503.5E-9**	**602.2E-9**
Displacement (m)	**425.00E-12**	**1.31E-9**	**3.92E-9**	**15.90E-9**	**18.80E-9**

200 µm span length

	2V	4V	6V	8V	10V
MAX (W)	28.90E-6	29.17E-6	30.50E-6	32.10E-6	32.30E-6
MIN (W)	29.56E-6	30.03E-6	29.15E-6	29.18E-6	28.94E-6
OUT Difference (W)	**661.2E-9**	**860.8E-9**	**1.4E-6**	**2.9E-6**	**3.4E-6**
Displacement (m)	**20.7E-9**	**26.8E-9**	**42.3E-9**	**75.0E-9**	**92.0E-9**

Using the simulations as a reference, the change in output intensity correlates to the change in the gap separation between the gratings (how close the gratings become). Thus, we can estimate the distance the SW gratings moved from their rested position and knowing the spring constant force and the measured displacement, the *g-force* acceleration was calculated and is plotted on a secondary axis as shown in Figure 5-11.

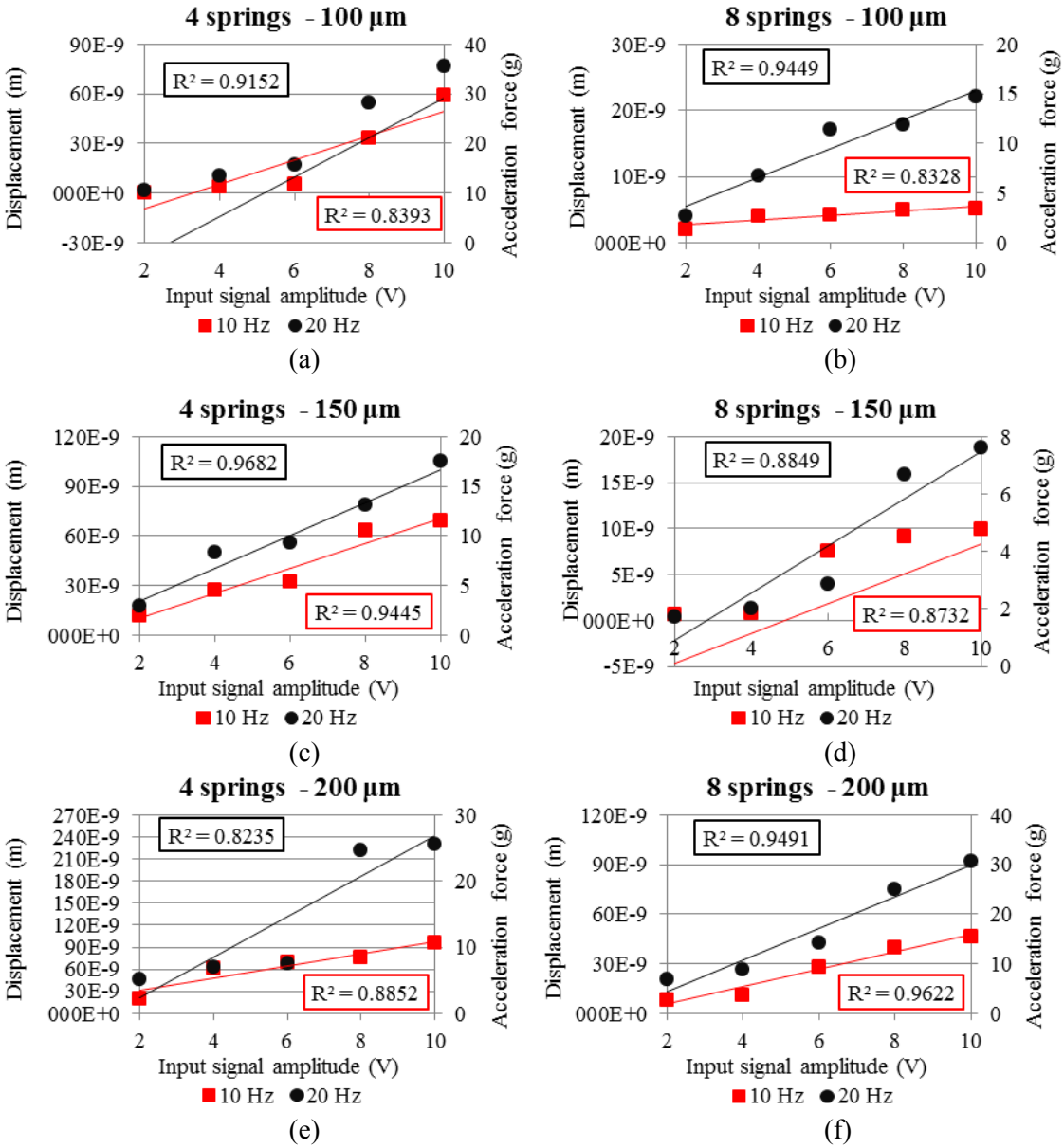

Figure 5-11: Displacement and *g-force* acceleration from the accelerometer spring designs

Ideally, in Figure 5-11, we would want to see the 10 Hz and 20 Hz curves in each graph to follow a linear trend, and both the displacement and *g-force* doubled as the frequency doubles, with 10 Hz results on the bottom and 20 Hz results on the top, an indication that the force increases (doubles) as the frequency increases. However, the curves in Figure 5-11 have some variance in the measured displacement and *g-force*. The data points of each graph were fit to a linear trend line, where the R-squared value is displayed, which represents a good fit of the line to the data. From the results, the least curve fit is 83% and the best curve fit is 97%.

An additional observation was noted in Figure 5-11 (d, e); the displacement and *g-force* was greater for the 10 Hz signal than the 20 Hz signal when a 6 V amplitude signal is applied, thus giving the lowest curve fit results. The non-linear displacement and *g-force* output in Figure 5-11 can be attributed to the exponentially decreasing nature of evanescent waves. From the simulation results in Chapter 3, the output intensity per change is gap separation decreased exponentially. Therefore, as the force from the subwoofer is applied to the accelerometer, if the output intensity change is great enough, it would be expected that the displacement would also considerably change, resulting in non-linear output.

In this chapter, we successfully calculated the total system noise, system sensitivity, and displacement resolution. In addition, designing and assembling the test setup, and testing the coupled SW grating accelerometers, we were able to achieve the estimated picometer resolution. The simulation results proved to be the reference point for determining both analytical and measured results. The signal-to-noise ratio was estimated to be 10.7 at a gap separation of 600 nm for the coupled SW gratings. Because

this is the maximum separation between the gratings this S/N works well for what we are doing.

Applying a known signal to the subwoofer increased the output intensity, measured by the photodiode, and caused the EW to couple as the gratings became closer. The gap displacement was determined by referencing the coupled SW grating simulations, where the simulated grating separations (0 nm to 600 nm) produced a specific output intensity value at the respective gap separations. Thus, the displacement was determined from the output intensity difference before and after the applied force from the speaker. In the final Chapter 6, the results and discussion will be presented.

Chapter 6

Results and Discussion

6.1 Evanescent Wave Coupling Modeling and Simulation

Far field diffraction was observed from evanescent wave coupling of two SW gratings with different grating periods in glass and Si substrates. The grating dimensions were optimized to achieve maximum output in the ±1 diffraction order. From SEM analysis in Chapter 4, we noticed the grating dimensions had changed from the profile of the simulated gratings. This was a result of process fabrication steps, (i.e., photolithography, RIE, DRIE etching). Figure 6-1 shows the re-simulated grating dimensions obtained from the SEM inspection.

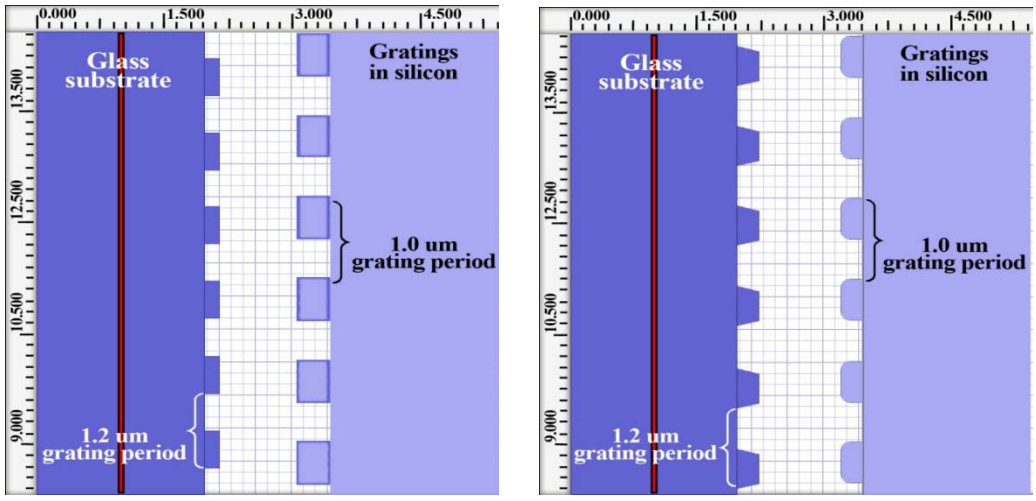

Figure 6-1: Simulation schematic of the coupled SW gratings (a) original simulation layout (b) re-simulation layout from SEM analysis

There was also a change in output intensity. As the gap separation increased, the output intensity decreased in the original simulation. The re-simulated output showed instances where larger gap separations (600 nm and 700 nm) had greater output intensity than the closer (500 nm) gap separation as seen in Figure 6-2.

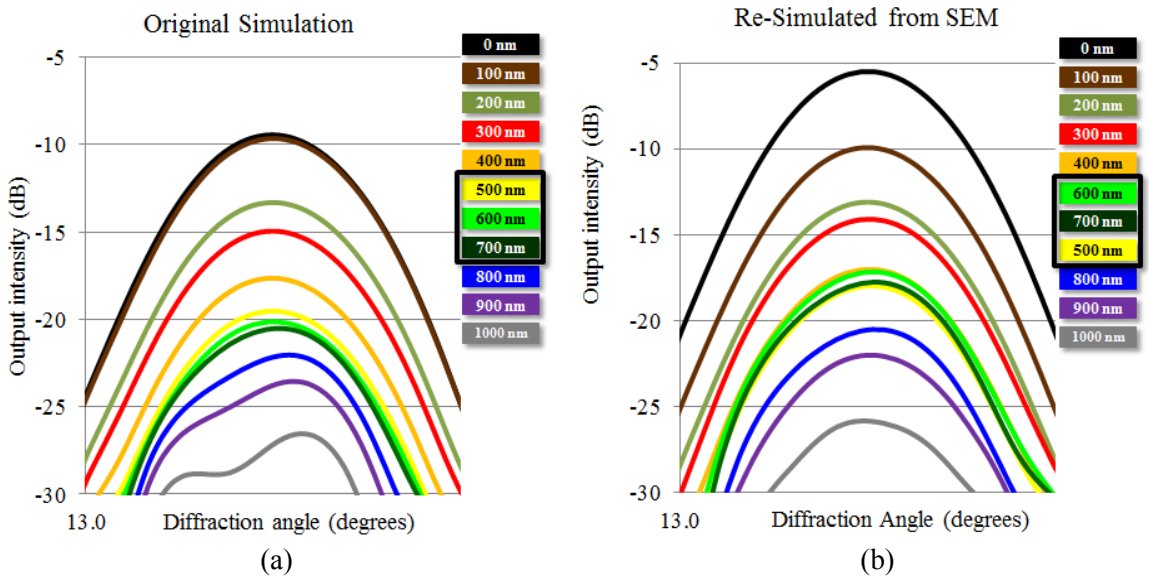

Figure 6-2: Simulation output intensity results (a) original simulation layout (b) re-simulation layout from SEM analysis

The reason for the increase in output intensity at the larger gap separations is not directly known. However, we do know that the grating dimensions play a significant role is the output intensity, thus, the rounded and trapezoidal shapes of the gratings are likely the cause. Furthermore, when the SW gratings are separated by 600 nm, the normalized output intensity from the original simulations was 12.26 µW. When the gratings were re-simulated, the output intensity measured 18.98 µW.

6.2 Measured Displacement and Spring Constant Comparison

The measured displacement ($\delta z = Fz/kz$) was obtained by applying a force (Fz) across the spring/proof mass using a Tencor P-10 profilometer, where maximum membrane displacement was observed. As the profilometer stylus was scanned across the membrane, the maximum and minimum of the curve was averaged, resulting in an estimated deflection. Table 6-1 compares the measured displacement of the spring/proof mass membrane with the analytical and simulated values.

Table 6-1: Analytical, simulated, and measured displacement comparison

Span length *b* (m)	**Applied Forcs** F_z (N)	**Analytical** 4 springs δ_z (N/m)	**Simulated** 4 springs δ_z (N/m)	**Measured** 4 springs δ_z (N/m)	**Analytical** 8 springs δ_z (N/m)	**Simulated** 8 springs δ_z (N/m)	**Measured** 8 springs δ_z (N/m)
200E-6	39.2E-6	67.2E-9	69.1E-9	67.2E-9	33.6E-9	34.5E-9	39.2E-9
150E-6	39.2E-6	39.1E-9	39.1E-9	41.8E-9	19.5E-9	19.6E-9	20.1E-9
100E-6	39.2E-6	19.0E-9	15.6E-9	17.2E-9	9.5E-9	9.7E-9	9.6E-9
200E-6	58.8E-6	100.8E-9	103.6E-9	97.4E-9	50.4E-9	51.8E-9	58.1E-9
150E-6	58.8E-6	58.6E-9	58.7E-9	54.0E-9	29.3E-9	29.4E-9	29.2E-9
100E-6	58.8E-6	28.6E-9	23.4E-9	30.8E-9	14.3E-9	14.6E-9	14.3E-9
200E-6	78.5E-6	134.4E-9	138.1E-9	136.3E-9	67.2E-9	69.1E-9	65.8E-9
150E-6	78.5E-6	78.1E-9	78.3E-9	79.6E-9	39.1E-9	39.1E-9	43.6E-9
100E-6	78.5E-6	38.1E-9	31.2E-9	40.7E-9	19.0E-9	19.4E-9	18.0E-9
200E-6	98.1E-6	168.1E-9	172.6E-9	178.0E-9	84.0E-9	86.3E-9	93.1E-9
150E-6	98.1E-6	97.7E-9	97.9E-9	99.4E-9	48.8E-9	48.9E-9	50.4E-9
100E-6	98.1E-6	47.6E-9	40.1E-9	51.6E-9	23.8E-9	24.3E-9	22.5E-9

In Figure 6-3 the analytical, simulated, and measured spring/proof mass displacement values are illustrated. The maximum difference between the analytical and

measured displacement was 11%, and the maximum difference between the simulated and measured displacement was 24%.

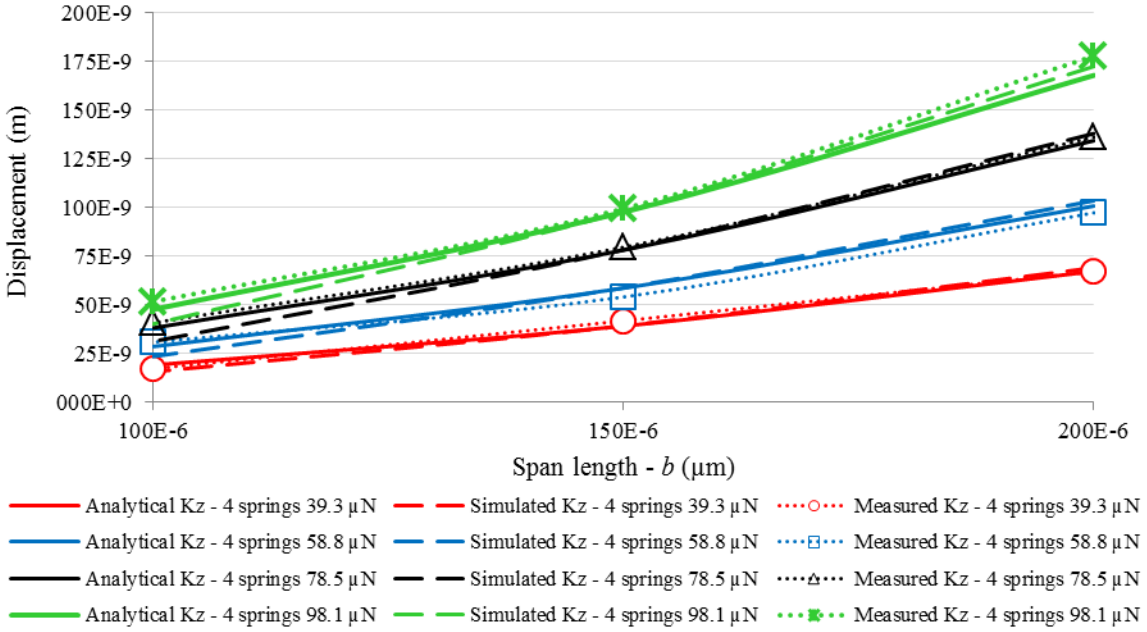

(a)

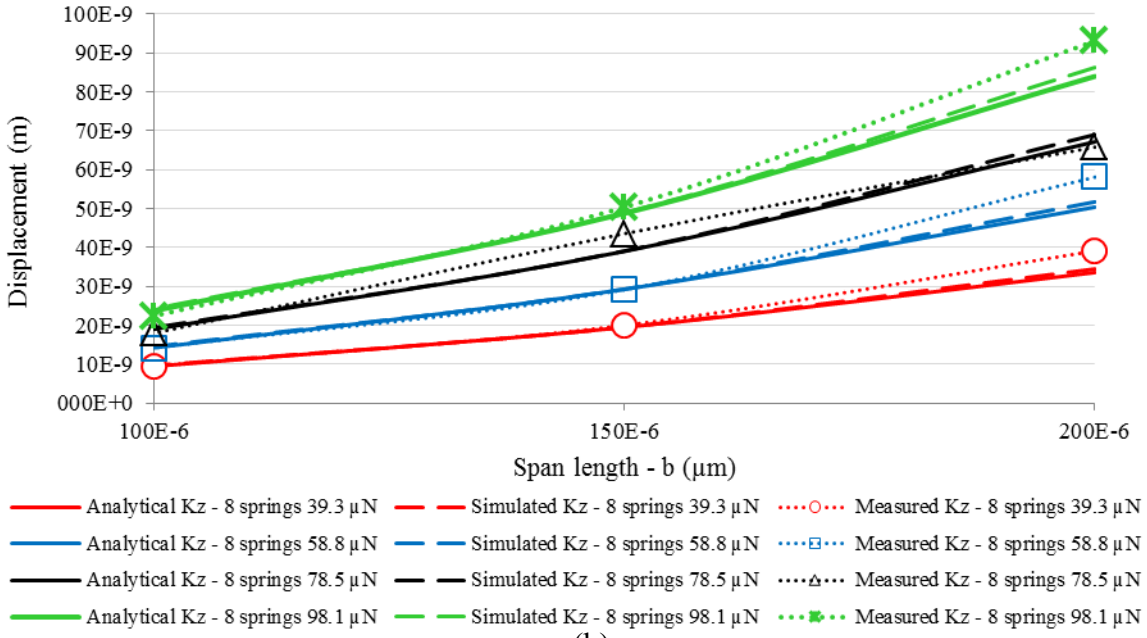

(b)

Figure 6-3: Spring/proof mass displacement comparison (a) analytical vs. measured (b) simulated vs. measured

The measured spring constant (kz = Fz / δz) was determined from the force to the proof mass of the accelerometer devices and the measured membrane displacement. Table 6-2 numerically compares the spring constant from the three springs and Figure 6-4 visually shows the comparison of the analytical, simulated, and measured spring constant measurements.

Table 6-2: Analytical, simulated, and measured spring constant force comparison

	8 springs 200 µm (N/m)	8 springs 150 µm (N/m)	8 springs 100 µm (N/m)	4 springs 200 µm (N/m)	4 springs 150 µm (N/m)	4 springs 100 µm (N/m)
Analytical	1167.0	2008.5	4120.3	583.5	1004.2	2060.1
Simulated	1136.0	2003.9	4034.9	568.0	1002.0	2017.5
Measured (avg)	1064.7	1929.1	4235.6	578.7	999.9	2006.0

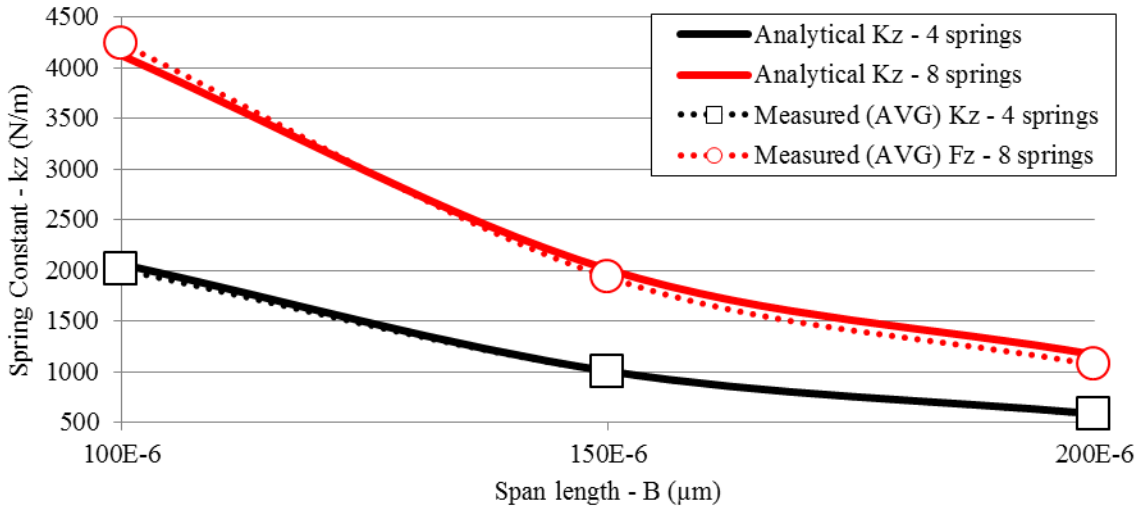

(a)

Figure 6-4: Spring constant comparison (a) analytical vs. measured (b) simulated vs. measured

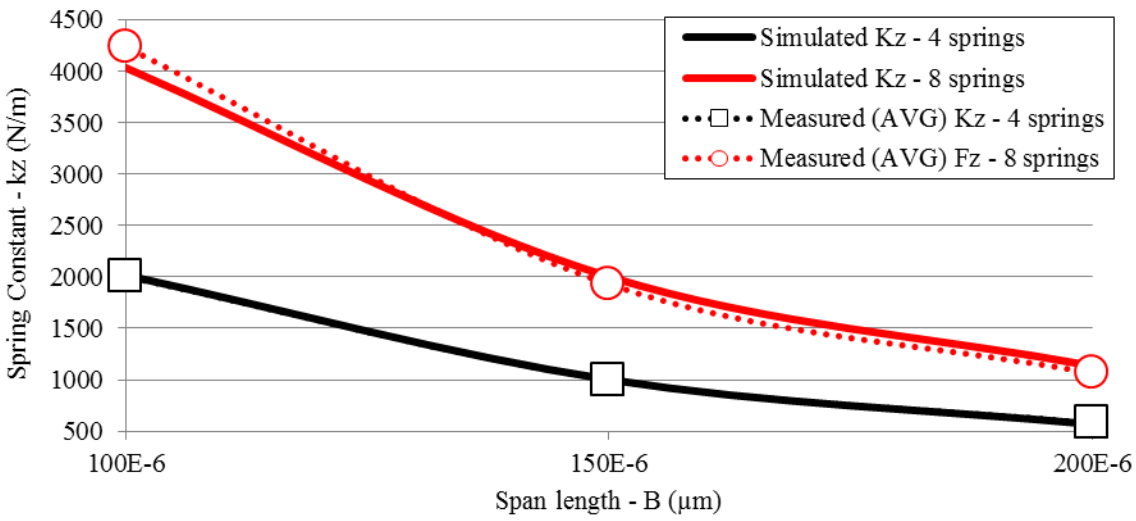

(b)

Figure 6-4 (Continued)

In Table 6-2, the spring constant for the measured values was averaged at the different applied force. After comparing the spring constant values for all the spring lengths, the difference for both four and eight springs was less than 10 %. Comparing the analytical versus measured constant, the maximum difference was 8.8 %, and the simulated versus measured was 6.3 %. It was concluded that the spring that had micro cracks or became broken during handling, thus causing the spring to be softer. These devices were not used for testing the accelerometer.

6.3 Surface Micromachining and Testing

A surface micromachined MEMS accelerometer with SW gratings etched in the spring/proof mass membrane was fabricated in silicon, its coupled grating pair was gratings etched in glass. The gratings were paired using Au:Au theromcompression bonding. The gold thickness on both the Si and glass chips is what determines the static grating separation. Also, the gold thickness on both chips had to be thick enough bond

strongly, resulting in 0.3 μm gold thickness on glass and silicon, having a total grating separation of 0.6 μm.

The bonded accelerometer was mounted on a testing apparatus where an acceleration force applied to the sensor from a 10 and 20 Hz sinusoidal input, with varying voltage amplitude (with 2V: 10V) caused the gap separation to change, resulting in an increase in output intensity. The fabricated small form factor (7 mm x 7 mm × 1 mm) sensor detects picometer displacement with the photodetector used in the setup, where a more sensitive photodetector estimates detecting femtometer resolution. By applying a force, the sensor detects small output intensity changes without amplification circuitry to increase the signal. Such a micro-sensor system will find many applications requiring high sensitivity, rapid readout rates, or operation in extreme thermal or electromagnetic environments where in-situ electronics are impractical.

6.4 Future Work

The picometer displacement resolution, demonstrated in this work shows potential in investigating non-destructive bonding integrity evaluation using SW gratings. The advantage of using this technology arises from the challenges in device testing, primarily after complete process fabrication and packaging. This concept would be implemented during the iterative processing steps. Moreover, on the research side of R&D, chip level integrity is essential to achieve fast throughput and high production yields, and this technology would be a key contributor to realizing chip level integrity. The two sub-wavelength periodic gratings are fabricated on the substrate and on the 3D MEMS package. When a packaged MEMS device is bonded to a substrate with sub-wavelength gratings and light is incident on the two sub-wavelength periodic gratings, evanescent

wave coupling occurs. In this, the propagation and enhanced transmission of evanescent waves allows precise measurement of distances between surfaces, thus evaluating the bonding integrity of the 3D MEMS package to the substrate. This concept is visually illustrated in Figure 6-5.

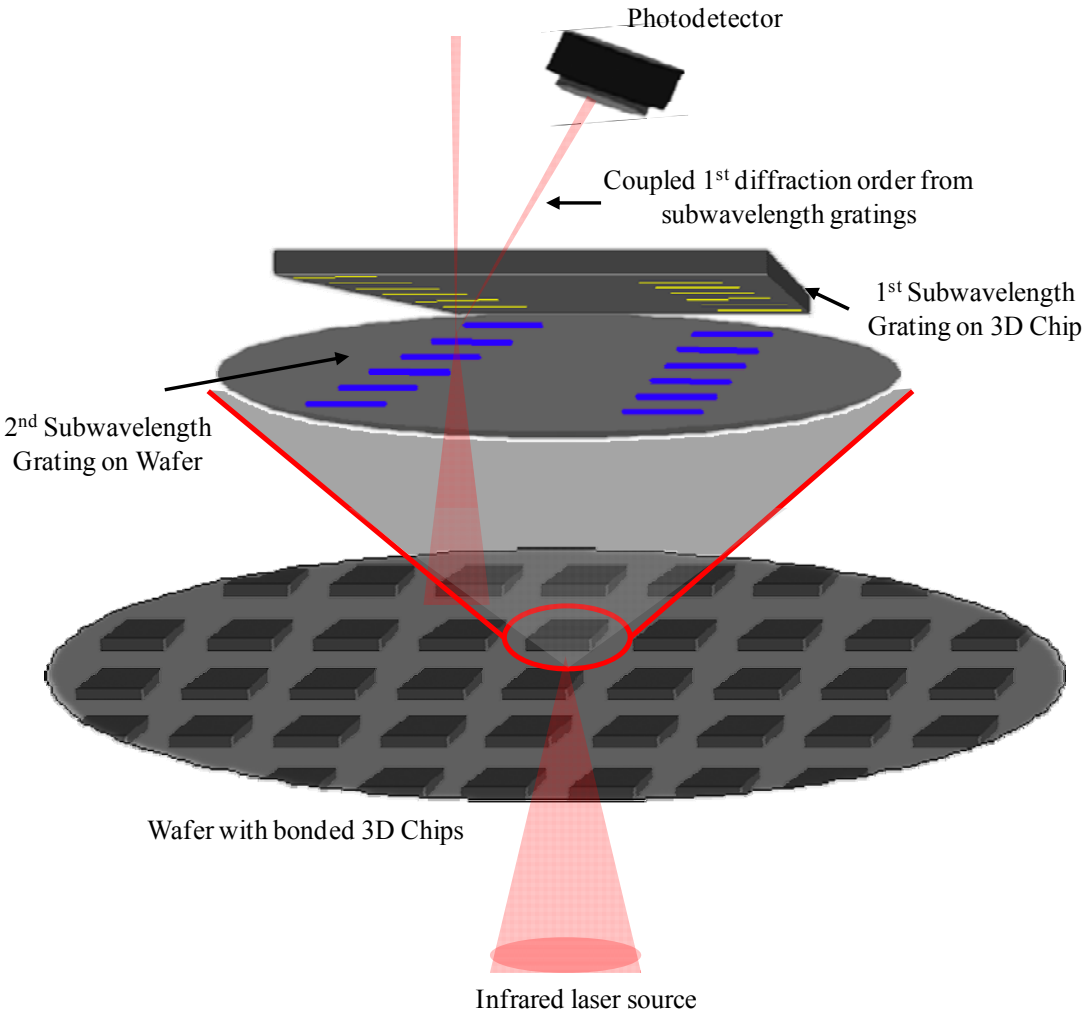

Figure 6-5: Schematic of using coupled SW gratings for evaluating bonding integrity

6.5 Conclusions

A working optical accelerometer was demonstrated in this dissertation. It was demonstrated to respond by its increase in output intensity from the evanescent wave coupling of the different SW gratings as a force is applied to it. It was successfully verified that the output intensity recorded, was directly referenced to the simulated results with a good fit.

Various SW grating fabrication methods were employed during this work. SW gratings measuring 100 nm were successfully demonstrated using electron beam lithography and SW gratings measuring 150 nm using holography.

Analytical models were used as a first approach to determining the spring constant forces and accelerometer displacements. This approach was compared to the simulation and measured results, where the consistency of the results verified using the analytical model.

Near-field evanescent wave coupling of various SW grating pairs, using a 1.55 μm infrared semiconductor laser was the first to be demonstrated measuring output intensity for use as an optical MEMS accelerometer. A novel coupled SW grating accelerometer was designed, fabricated, and tested, where picometer displacement resolution has been realized.

References

1. Loewen, E.G. and E. Popov, *Diffraction gratings and applications*. illustrated ed. Vol. 58. 1997: CRC Press.

2. Groner, P.K., M. Neviere, and E. Popov, *Light Propagation in Periodic Media: Differential Theory and Design*. 2003: CRC Press.

3. Porter, R., *The biographical dictionary of scientists*. 1994, New York: Oxford University Press.

4. Greenslade, J.T.B., *Wire Diffraction Gratings.* The Physics Teacher, 2004. 42(2): p. 76-77.

5. Girard, C. and A. Dereux, *Near-field optics theories.* Reports on progress in physics., 1996. 59(5): p. 657.

6. Walter, P.L., *The History of the Accelerometer.* Sound and Vibration, 2007. 41(1): p. 84-93.

7. Zengerle, R., *Light propagation in singly and doubly periodic planar waveguides.* Journal of modern optics 1987. 34(12): p. 1589.

8. Brazas, J.C., L. Li, and A.L. McKeon, *High-efficiency input coupling into optical waveguides using gratings with double-surface corrugation.* Appl. Opt., 1995. 34(4): p. 604-609.

9. Tomita, M., *Thin-film waveguide with a periodic groove structure of finite extent.* J. Opt. Soc. Am. A, 1989. 6(9): p. 1455-1464.

10. Gupta, M.C. and S.T. Peng, *Diffraction of a light beam by doubly periodic structures.* Opt. Lett., 1991. 16(17): p. 1301-1303.

11. Connolly, T., *SENSOR - TECHNOLOGY AND DESIGN - Variable Capacitance Accelerometers: Design and Applications - Micromachined silicon variable-capacitance accelerometers are designed for easy manufacture and demanding applications.* Sensors., 2002. 19(5): p. 55.

12. Lynch, J.P., et al., *Design of Piezoresistive MEMS-Based Accelerometer for Integration with Wireless Sensing Unit for Structural Monitoring.* Journal of Aerospace Engineering, 2003. 16(3): p. 108-114.

13. Liu, C.H. and T.W. Kenny, *A High-Precision, Wide-Bandwidth Micromachined Tunneling Accelerometer.* Journal of Microelectromechanical Systems, 2001. 10: p. 425-433.

14. Abbaspour-Sani, E., H. Ruey-Shing, and K. Chee Yee, *A novel electromagnetic accelerometer.* Electron Device Letters, IEEE, 1994. 15(8): p. 272-273.

15. Waters, R.L. and M.E. Aklufi, *Micromachined Fabry--Perot interferometer for motion detection.* Applied Physics Letters, 2002. 81(18): p. 3320-3322.

16. Kunz, K., P. Enoksson, and G. Stemme, *Highly sensitive triaxial silicon accelerometer with integrated PZT thin film detectors.* Sensors and Actuators A: Physical, 2001. 92(1-3): p. 156-160.

17. Li, G.X. and F.A. Shemansky, *Drop test and analysis on micro-machined structures.* Sensors and Actuators A: Physical, 2000. 85(1-3): p. 280-286.

18. Abdolvand, R., B. Vakili Amini, and F. Ayazi, *Sub-Micro-Gravity In-Plane Accelerometers With Reduced Capacitive Gaps and Extra Seismic Mass.* Journal of microelectromechanical systems : a joint IEEE and ASME publication on microstructures, microactuators, microsensors, and microsystems., 2007. 16(5): p. 1036.

19. Texas_Instruments. *Accelerometers and How They Work*. 2007; Available from: http://www2.usfirst.org/2005comp/Manuals/Acceler1.pdf.

20. Nintendo of America Inc., *"Annual Financial Report"*. 2008.

21. Kristoff, S., *"An Introduction to Accelerometers Using Sensors to Measure Acceleration, Using Sensors to Measure Acceleration"*. 2008.

22. Apple Inc., *"Quarter 3 Earnings"*. 2008.

23. Reedy, S., *MEMS the Word*, in *Light Reading* 2010.

24. Honeywell, *Sensotec Accelerometers*

25. Valoff, S. and W.J. Kaiser. *Presettable micromachined MEMS accelerometers*. in *Micro Electro Mechanical Systems, 1999. MEMS '99. Twelfth IEEE International Conference on*. 1999.

26. Sawada, R., E. Higurashi, and T. Itoh. *An accelerometer incorporating a micro-laser encoder for a wide measurable range [for earthquake detection]*. in *Optical MEMS, 2000 IEEE/LEOS International Conference on*. 2000.

27. Todd, M.D., et al., *Flexural Beam-Based Fiber Bragg Grating Accelerometers.* IEEE Photonics Technology Letters, 1998. 10(11): p. 1605-1607.

28. Tien, N.C. *Micro-optical inertial sensors using silicon MEMS*. in *Aerospace Conference, 1998. Proceedings., IEEE*. 1998.

29. Keeler, B.E.N., G.R. Bogart, and D.W. Carr, *Laterally deformable optical NEMS grating transducers for inertial sensing applications.* Proceedings- SPIE the International Society for Optical Engineering, 2004. 5592: p. 306-312.

30. Carr, D.W., J.P. Sullivan, and T.A. Friedmann, *Laterally deformable nanomechanical zeroth-order gratings: anomalous diffraction studied by rigorous coupled-wave analysis.* Optics Letters, 2003. 28: p. 1636-1638.

31. Carr, D.W., et al., *Measurement of a laterally deformable optical NEMS grating transducer [5346-06]*. Proceedings- SPIE the International Society for Optical Engineering, 2004(5346): p. 56-63.

32. Loh, N.C., M.A. Schmidt, and S.R. Manalis, *Sub-10 cm^3 interferometric accelerometer with nano-g resolution.* Microelectromechanical Systems, Journal of, 2002. 11(3): p. 182-187.

33. De Vlaminck, I., et al., *Integrated nanomechanical motion detection by means of optical evanescent wave coupling [6464-13]*. Proceedings- SPIE The International Society For Optical Engineering, 2007. 6464: p. 64640E.

34. Lee, W., et al., *Fabrication and Characterization of a Micromachined Acoustic Sensor With Integrated Optical Readout.* IEEE Journal of Selected Topics in Quantum Electronics, 2004. 10(3): p. 643-651.

35. Hall, N.A., L. Wook, and F.L. Degertekin, *Capacitive micromachined ultrasonic transducers with diffraction-based integrated optical displacement detection.* IEEE transactions on ultrasonics, ferroelectrics, and frequency control, 2003. 50(11): p. 1570-80.

36. Karabacak, D., et al., *Optical knife-edge technique for nanomechanical displacement detection.* Applied physics letters., 2006. 88(19): p. 193122.

37. Karabacak, D., T. Kouh, and K.L. Ekinci, *Analysis of optical interferometric displacement detection in nanoelectromechanical systems (9 pages).* Journal of Applied Physics, 2005. 98(12): p. 124309.

38. Loewen, E.G. and E. Popov, *Diffraction Gratings and Applications* Optical Science and Engineering. 1997 CRC Press. 630.

39. Ishimori, M., et al., *Subwavelength Antireflection Gratings for Light Emitting Diodes and Photodiodes Fabricated by Fast Atom Beam Etching.* The Japan Society of Applied Physics, 2002. 21(Part 1, No. 6B): p. 4346-4349.

40. Lee, H.S., et al., *Color filter based on a subwavelength patterned metal grating.* Optics express, 2007. 15(23): p. 15457-63.

41. Barbara, A., et al., *Optical transmission through subwavelength metallic gratings.* Physical Review B, 2002. 66(16): p. 161403.

42. Cao, H. and A. Nahata, *Influence of aperture shape on the transmission properties of a periodic array of subwavelength apertures.* Optics express, 2004. 12(16): p. 3664-72.

43. Voros, J., et al., *Optical grating coupler biosensors.* Biomaterials., 2002. 23(17): p. 3699-3710.

44. Quidant, R., et al., *Near-field observation of evanescent light wave coupling in subwavelength optical waveguides.* Europhysics Letters, 2002. 57: p. 191-197.

45. Cheben, P., et al., *Subwavelength waveguide grating for mode conversion and light coupling in integrated optics.* Optics express, 2006. 14(11): p. 4695-702.

46. Cho, G.C., et al., *Apertureless terahertz near-field microscopy.* Semiconductor science and technology., 2005. 20(7): p. S286-S292.

47. Taniguchi, K. and Y. Kanemitsu, *Development of an Apertureless Near-Field Optical Microscope for Nanoscale Optical Imaging at Low Temperatures.* Japanese Journal of Applied Physics, 2005. 44(1B): p. 575-577.

48. Goodman, J.W., *Introduction to Fourier optics*. 2005, Englewood, Colo.: Roberts & Co.

49. Yee, K., *Numerical solution of initial boundary value problems involving maxwell's equations in isotropic media.* Antennas and Propagation, IEEE Transactions on, 1966. 14(3): p. 302-307.

50. OptiFDTD, O., *Optiwave OptiFDTD - Finite Difference Time Domain Photonics Simulation Software Technical Background and Tutorials,*.

51. Courant, R., Friedrichs, K., and Lewy, H. , *On the partial difference equations of mathematical physics.* IBM Journal, 1967. 11: p. 215-234.

52. Baidya, R., S.K. Gupta, and T. Mukhcrjee. *MEMS Component Extraction*. in *Int'l Conf. Modeling and Simulation of Microsystems, Semiconductors, Sensors, and Actuators* 1999. San Juan, Puerto Rico.

53. Giuseppe, B., et al., *Analysis, simulation and relative performances of two kinds of serpentine springs.* Journal of Micromechanics and Microengineering, 2005. 15: p. 736-746.

54. Hao, L., et al., *A post-CMOS micromachined lateral accelerometer.* Microelectromechanical Systems, Journal of, 2002. 11(3): p. 188-195.

55. Lishchynska, M., et al., *Spring Constant Models for Analysis and Design of MEMS Plates on Straight or Meander Tethers.* Sensor Letters, 2006. 4(2): p. 200-205.

56. Fedder, G.K., *Simulation of microelectromechanical systems*, in *Dept. of Electrical Engineering and Computer Science*. 1994, Univ. of California at Berkeley.

57. Rouabah, H.A., C.O. Gollasch, and M. Kraft. *Design optimization of an electrostatic MEMS actuator with low spring constant for an 'Atom Chip*. in *Proc. NSTI Nanotech*. 2005. Anaheim, CA, USA.

58. Cho, Y.-H. and A.P. Pisano. *"Optimum Structural Design of Micromechanical Crab-Leg Flexures with Microfabrication Constraints",*. in *Proc. ASME, DSC v. 19, Microstructures, Sensors and Actuators*. 1990. ASME Winter Annual Meeting.

59. *Electron Beam Lithography Instrumentation*. 2006; Available from: http://www4.nau.edu/microanalysis/Microprobe-SEM/Instrumentation.html.

60. Rai-Choudhury, P., et al., *Handbook of microlithography, mircomachining, and microfabrication*. SPIE Press monograph, PM39-PM40. 1997, Bellingham, Wash. : London: SPIE ; IEE.

61. Aktary, M., et al., *High-resolution pattern generation using the epoxy novolak SU-8 2000 resist by electron beam lithography.* Journal of Vacuum Science & Technology B: Microelectronics and Nanometer Structures, 2003. 21(4): p. L5-L7.

62. Myers, B.D. and V.P. Dravid, *Variable Pressure Electron Beam Lithography (VP-eBL): A New Tool for Direct Patterning of Nanometer-Scale Features on Substrates with Low Electrical Conductivity.* Nano letters., 2006. 6(5): p. 963.

63. Puetz, P. and K. Jacobs. *E-Beam SIS Junction Fabrication Using CMP and E-Beam Defined Wiring Layer*. in *Proceedings of the Tenth International Symposium on Space Terahertz Technology*. 1999. University of Virginia, Charlottesville, VA USA.

64. Peng, S.T., T. Tamir, and H.L. Bertoni, *Theory of Periodic Dielect Waveguides.* Microwave Theory and Techniques, IEEE Transactions on, 1975. 23(1): p. 123-133.

65. Rogers, A.-A.A., S. Samson, and S. Kedia, *Far-field evanescent wave propagation using coupled subwavelength gratings for a MEMS sensor.* Journal Optical Society of America A, 2009. 26(12): p. 5.

66. Palmer, C., *Diffraction Grating Handbook*. 6th ed. 2005: Newport Corporation

67. Chuang, W.-C., C.-T. Ho, and W.-C. Wang, *Fabrication of a high-resolution periodical structure using a replication process.* Optics Express, 2005. 13(18): p. 8.

68. Chen, T.T. and D.H.-M. Hawang, *Grating Fabrication by Interference of Laser Beams.* Chinese Journal of Physics, 1977. 15(1): p. 4.

69. Zaidi, S.H. and S.R.J. Brueck, *High aspect-ratio holographic photoresist gratings.* Applied Optics, 1998. 27(14): p. 4.

70. Boyd, R.D., et al., *High-efficiency metallic diffraction gratings for laser applications.* Applied Optics, 1995. 34(10).

71. Walsh, M.E. and H.I. Smitha, *Method for reducing hyperbolic phase in interference lithography.* Journal of Vacuum Science & Technology B, 2001. 19(6).

72. Chen, C.G., et al. *Nanometer-accurate Grating Fabrication with Scanning Beam Interference Lithography*. in *SPIE's International Symposium on Smart Materials, Nano-, and Micro- Smart Systems*. 2002. Melbourne, AUSTRALIA.

73. Fernandez, A., et al., *Use of interference lithography to pattern arrays of submicron resist structures for field emission flat panel displays.* Journal of Vacuum Science & Technology B, 1997. 15(7).

74. Willie, W.N., H. Chi-Shain, and A. Yariv, *Holographic interference lithography for integrated optics.* Electron Devices, IEEE Transactions on, 1978. 25(10): p. 1193-1200.

75. Bryan, D.A. and J.K. Powers, *Improved holography for chirped gratings.* Opt. Lett., 1980. 5(9): p. 407-409.

76. Austin, S. and F.T. Stone, *Fabrication of thin periodic structures in photoresist: a model.* Appl. Opt., 1976. 15(4): p. 1071-1074.

77. Bartolini, R.A., *Characteristics of Relief Phase Holograms Recorded in Photoresists.* Appl. Opt., 1974. 13(1): p. 129-139.

78. Dos Santos, P.A.M., *Moiré-like patterns as a spatial beat frequency in photorefractive sinusoidal phase gratings superposition.* Optics Communications, 2002. 212(4-6): p. 211-216.

79. Enger, R.C. and S.K. Case, *High-frequency holographic transmission gratings in photoresist.* J. Opt. Soc. Am., 1983. 73(9): p. 1113-1118.

80. Madou, M.J., *Fundamentals of Microfabrication: The Science of Miniaturization*. 2nd ed. 2002: CRC Press.

81. Petersen, K.E., *Silicon as a mechanical material.* Proceedings of the IEEE, 1982. 70(5): p. 420-457.

82. Kovacs, G.T.A., N.I. Maluf, and K.E. Petersen, *Bulk micromachining of silicon.* Proceedings of the IEEE, 1998. 86(8): p. 1536-1551.

83. Richter, M., et al. *A chemical microanalysis system as a microfluid system demonstrator*. in *Solid State Sensors and Actuators, 1997. TRANSDUCERS '97 Chicago., 1997 International Conference on*. 1997.

84. Helvajian, H., *Microengineering Aerospace Systems*, American Institute of Aeronautics and Astronautics/Aerospace Press.

85. Geschke, O., H. Klank, and P. Telleman, *Microsystem Engineering of Lab-on-a-Chip Devices*. 2008: Wiley-VCH.

Appendices

Appendix A: Process Flows

The process flow for the bulk accelerometer and the glass lid with SW gratings are described in Table A-1 and Table A-2.

Table A-1: Bulk silicon accelerometer process flow

000		Get wafer		
005		Measure wafer thickness		excel spreadsheet to measure thickness and weight
010		Spin adhesion promoter	HMDS	3K 40sec; 120C 60sec
015		Spin photoresist	PR1-500	5K 40sec; 120C 120sec
020	INDENT	Expose	MASK1: INDENT	2.9 sec-*has the gratings on the mask CRUCIAL*
025		Develop	PR1-500	RD6; 10-15sec
030		wafer inspection		optical microscope
035		Etch Silicon	NonBosch1	*etch 200 nm for gratings in Si- 3min 7sec*
040		Strip Resist		Acetone/Methanol - 15min
045		wafer inspection		optical microscope
050		Descum	300_0_0_400_3	3min
055		wafer inspection		SEM
070		Sputter Cr	2 minutes	adhesion layer for the gold (adds to gap thickness)
080		Sputter Au	3 minutes	*gold thickness to determine gap seperation after bond*
105		Spin	PR1-200A	3K 40sec; 120C 60sec-
110	METAL(Au:Au)	expose	MASK2: METAL	4.2 sec
115		Develop	RD6	RD6 40sec
120		Descum	PRETCH3	1min
125		wafer inspection		inspect for resist removal
130		Au etch	gold etchat	Etch until cleared + 30% - 90 sec
135		Cr etch		Etch until cleared + 30% - 35 sec
140		Cascade rinse	thorough rinse	
145		Strip Resist		Acetone/Methanol

Appendix A (Continued)

Table A-1 (Continued)

155		Descum	300_0_0_400_10	10min
160		wafer inspection		inspect for resist removal
200		Sputter Al	*BACKSIDE*	5 minutes
210		Spin - *BACKSIDE*	PR1-200A	3K 40sec; 120C 60sec-
220	METAL 2 MOD	expose	MASK4:METAL 2	3.0 sec
230		Develop	RD6	RD6 40sec
240		wafer inspection		optical microscope inspection
245		Descum	300_0_0_400_3	3 min
250		Al etch	Transene Al	Etch until cleared + 30%
260		Inspect		Look carefully for isolated Al areas
270		DRIE etch wafer	Bosch 425 um	mostly through wafer etch
280		Inspect		Look carefully for isolated Al areas
285		Strip Resist		Acetone/Methanol
290		Descum	300_0_0_400_3	3 min
300	STRUCTURE	Spin - *FRONTSIDE*	PR1-2000A	3K 40sec; 120C 60sec- *thick enough to use as a hard mask for DRIE*
305		expose	MASK3: STRUCTURE	4.2 sec
310		Develop	RD6	RD6; 50sec
315		Descum	300 0 0 400 3	3 min
320		wafer inspection		optical microscope
325	**********	Place on Carrier Wafer		*place on carrier wafer with cool grease*
330		Etch Silicon	Bosch45	*etch ~30 or the remaining through the wafer*
335		Manually apply Resist		*Manually apply PR1-2000 for dicing and bake @ 120C for 10min*
340		Dice Wafer		
345		Strip Resist		Acetone/Methanol
350		Descum chips	300_0_0_400_10	10min
355		wafer inspection		optical microscope
360		Au/Au TC Bonding	Thermal Compression Au/Au USF-04	320 C temperature /80 N force/

Appendix A (Continued)

Table A-2: Glass lid process flow

000		Get wafer		
005		Measure wafer thickness		excel spreadsheet to measure thickness and weight
010		Spin adhesion promoter	HMDS	3K 40sec; 120C 60sec
015		Spin photoresist	PR1-500	5K 40sec; 120C 120 sec
020	INDENT	Expose	MASK1: INDENT	**2.9** sec-*has the gratings on the mask CRUCIAL*
025		Develop	PR1-500	RD6; 10-15sec
030		wafer inspection		optical microscope
035		Etch Pyrex	S_Etch	*etch 300 nm for gratings in pyrex 10 min*
040		Strip Resist		Acetone/Methanol - 15min
045		wafer inspection		optical microscope
050		Descum	300_0_0_400_3	3min
055		wafer inspection		SEM
060		Sputter Cr	3 minutes	adhesion layer for the gold (adds to gap thickness)
100		Sputter Au	4 minutes	*gold thickness to determine gap seperation after bond*
105		Spin	PR1-200A	3K 40sec; 120C 60sec-
110	METAL(Au:Au)	expose	MASK2: METAL	4.2 sec
115		Develop	RD6	RD6 40sec
120		Descum	300_0_0_400_1	1min
125		wafer inspection		inspect for resist removal
130		Au etch	gold etchat	Etch until cleared + 30% - 90 sec
135		Cr etch		Etch until cleared + 30% - 35 sec
140		Cascade rinse	thorough rinse	
145		Strip Resist		Acetone/Methanol
150		Descum	300_0_0_400_10	10min
155		wafer inspection		inspect for resist removal
360		Au/Au TC Bonding		320 C temperature /80 N force/

Appendix B: Output Intensity from Accelerometer Devices

The output intensity from the 100 µm, 150 µm, and 200 µm spring length accelerometers with four and eight springs attached to the proof mass are shown in Figure B-1 - B-12 and numerically represented in Table B-1 - B-12.

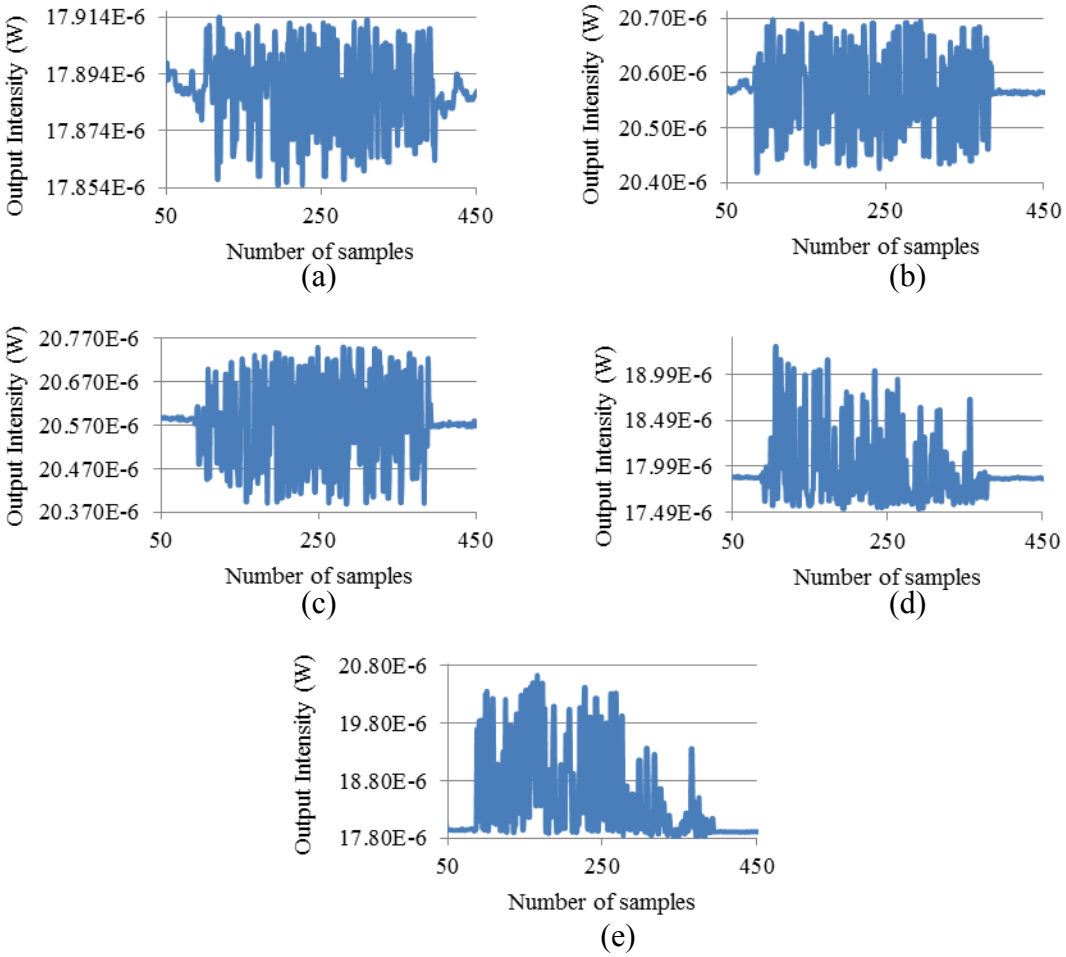

Figure B-1: 4 Springs 100 µm at 10 Hz accelerometer graphs

Table B-1: Output intensity difference from the 4 Springs 100 µm at 10 Hz graphs

	B-1 (a)	**B-1 (b)**	**B-1 (c)**	**B-1 (d)**	**B-1 (e)**
Signal and amplitude	10 Hz 2 V	10 Hz 4 V	10 Hz 6 V	10 Hz 8V	10 Hz 10 V
Output Intensity Difference	26.9 nW	126.8 nW	188.3 nW	1.03 µW	1.88 µW

Appendix B (Continued)

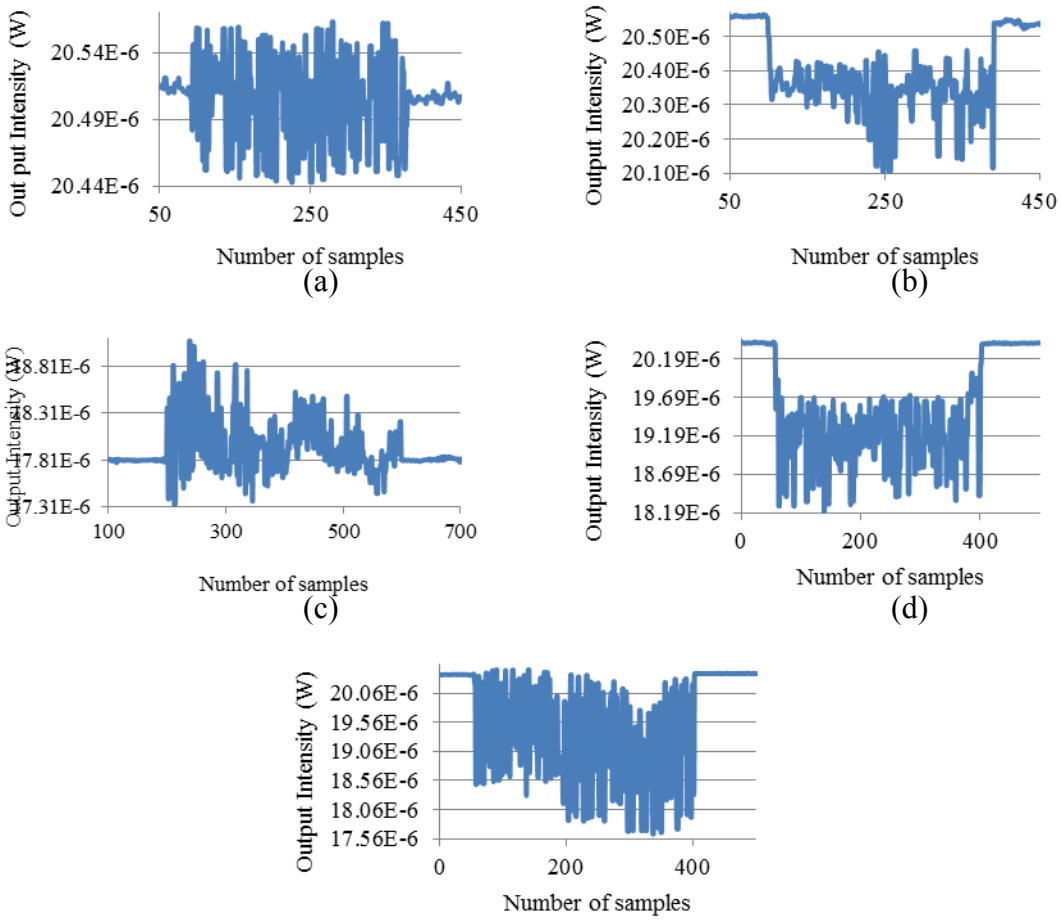

Figure B-2: 4 Springs 100 µm at 20 Hz accelerometer graphs

Table B-2: Output intensity difference from the 4 Springs 100 µm at 20 Hz graphs

	B-2 (a)	**B-2 (b)**	**B-2 (c)**	**B-2 (d)**	**B-2 (e)**
Signal and amplitude	20 Hz 2 V	20 Hz 4 V	20 Hz 6 V	20 Hz 8V	20 Hz 10 V
Output Intensity Difference	61.3 nW	339.5 nW	548.1 nW	1.74 µW	2.45 µW

Appendix B (Continued)

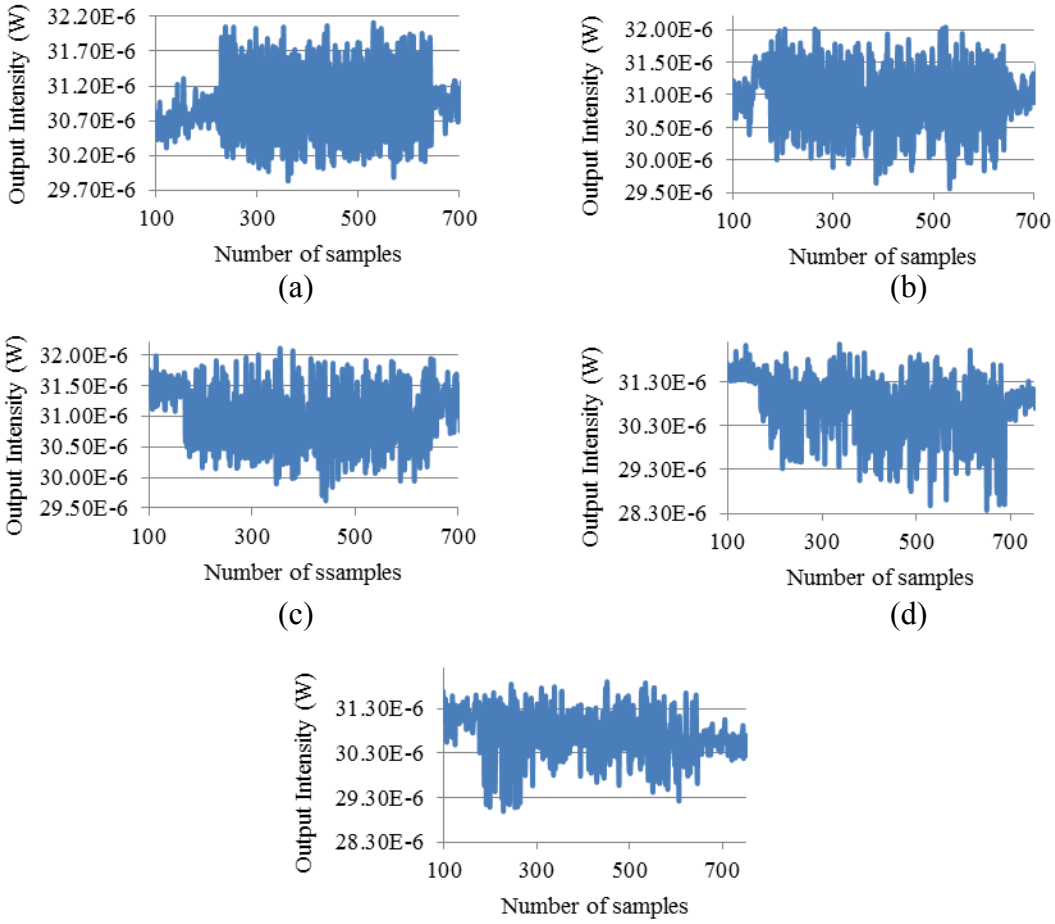

Figure B-3: 4 Springs 150 µm at 10 Hz accelerometer graphs

Table B-3: Output intensity difference from the 4 Springs 150 µm at 10 Hz graphs

	B-3 (a)	**B-3 (b)**	**B-3 (c)**	**B-3 (d)**	**B-3 (e)**
Signal and amplitude	10 Hz 2 V	10 Hz 4 V	10 Hz 6 V	10 Hz 8V	10 Hz 10 V
Output Intensity Difference	367.1 nW	863.7 nW	1.04 µW	2.02 µW	2.20 µW

Appendix B (Continued)

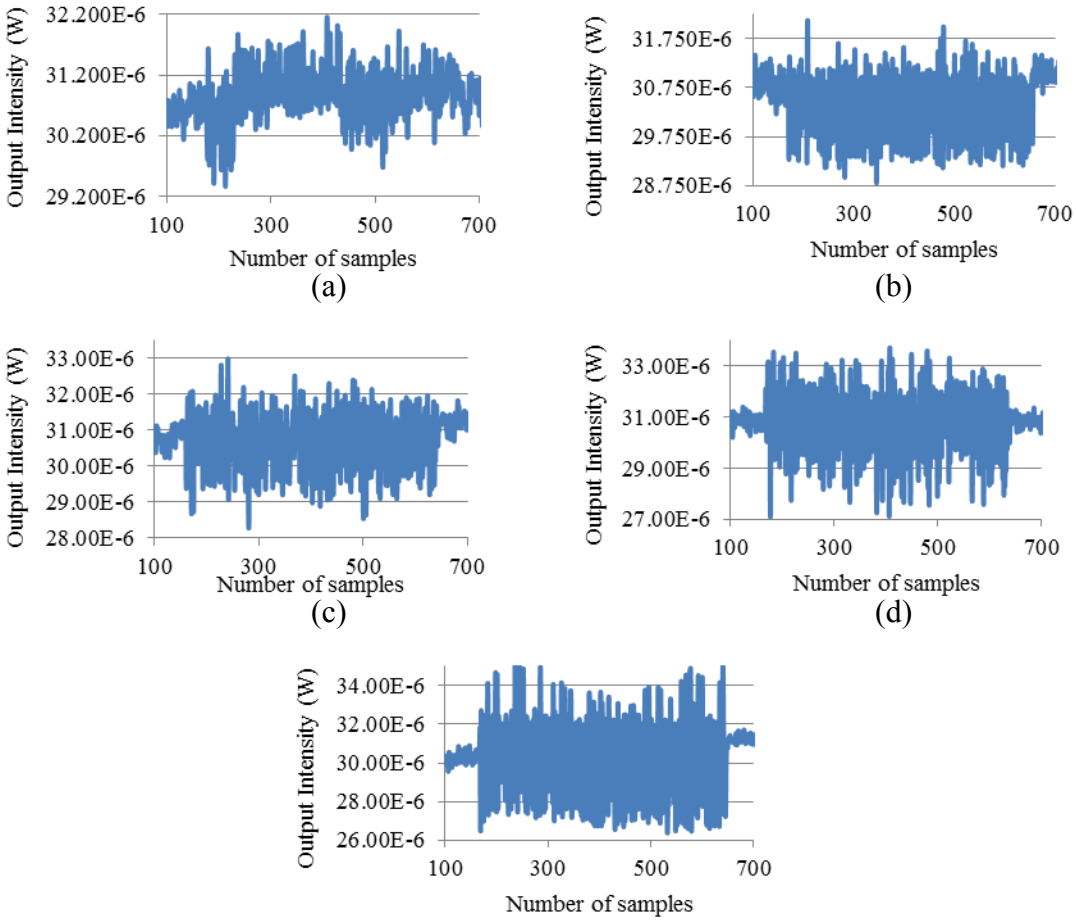

Figure B-4: 4 Springs 150 µm at 20 Hz accelerometer graphs

Table B-4: Output intensity difference from the 4 Springs 150 µm at 20 Hz graphs

	B-4 (a)	B-4 (b)	B-4 (c)	B-4 (d)	B-4 (e)
Signal and amplitude	20 Hz 2 V	20 Hz 4 V	20 Hz 6 V	20 Hz 8V	20 Hz 10 V
Output Intensity Difference	563.9 nW	1.59 µW	1.77 µW	2.52 µW	3.64 µW

Appendix B (Continued)

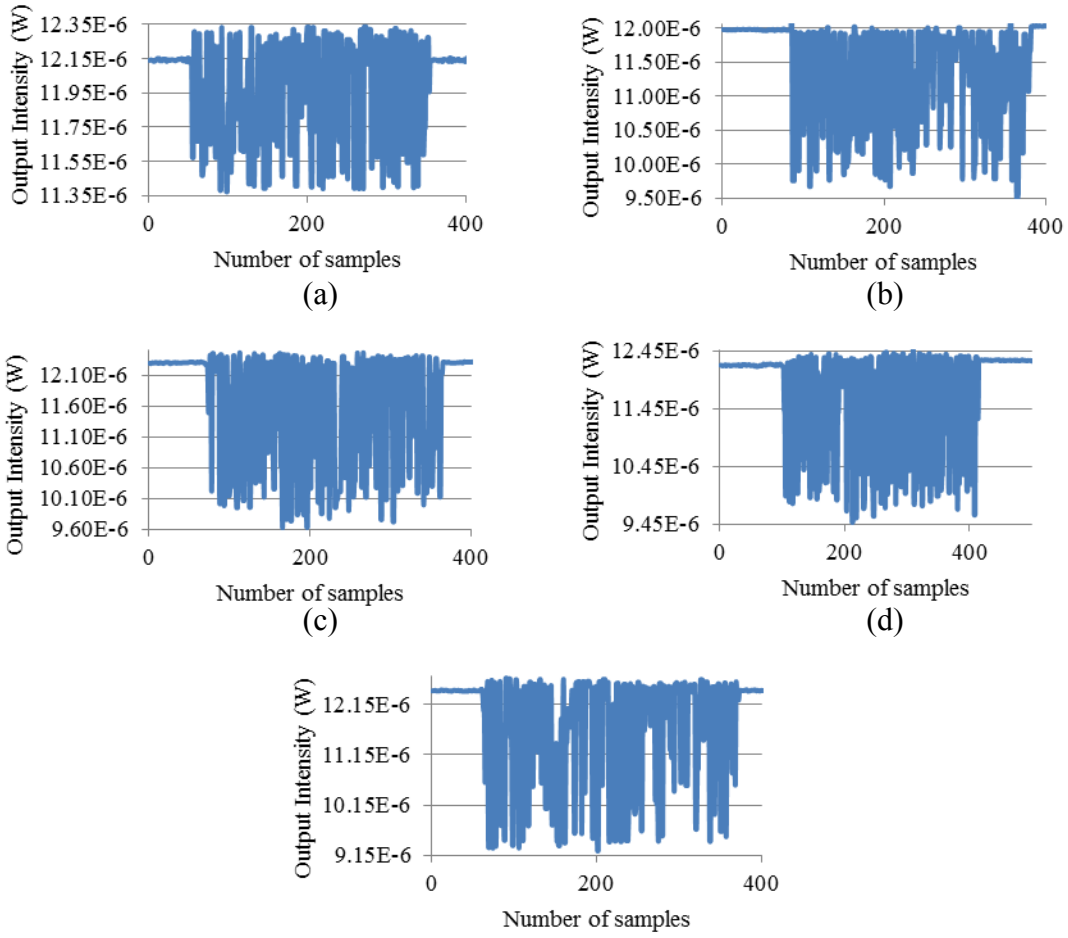

Figure B-5: 4 Springs 200 µm at 10 Hz accelerometer graphs

Table B-5: Output intensity difference from the 4 Springs 200 µm at 10 Hz graphs

	B-5 (a)	**B-5 (b)**	**B-5 (c)**	**B-5 (d)**	**B-5 (e)**
Signal and amplitude	10 Hz 2 V	10 Hz 4 V	10 Hz 6 V	10 Hz 8V	10 Hz 10 V
Output Intensity Difference	692.4 nW	1.99 µW	2.20 µW	2.44 µW	3.02 µW

Appendix B (Continued)

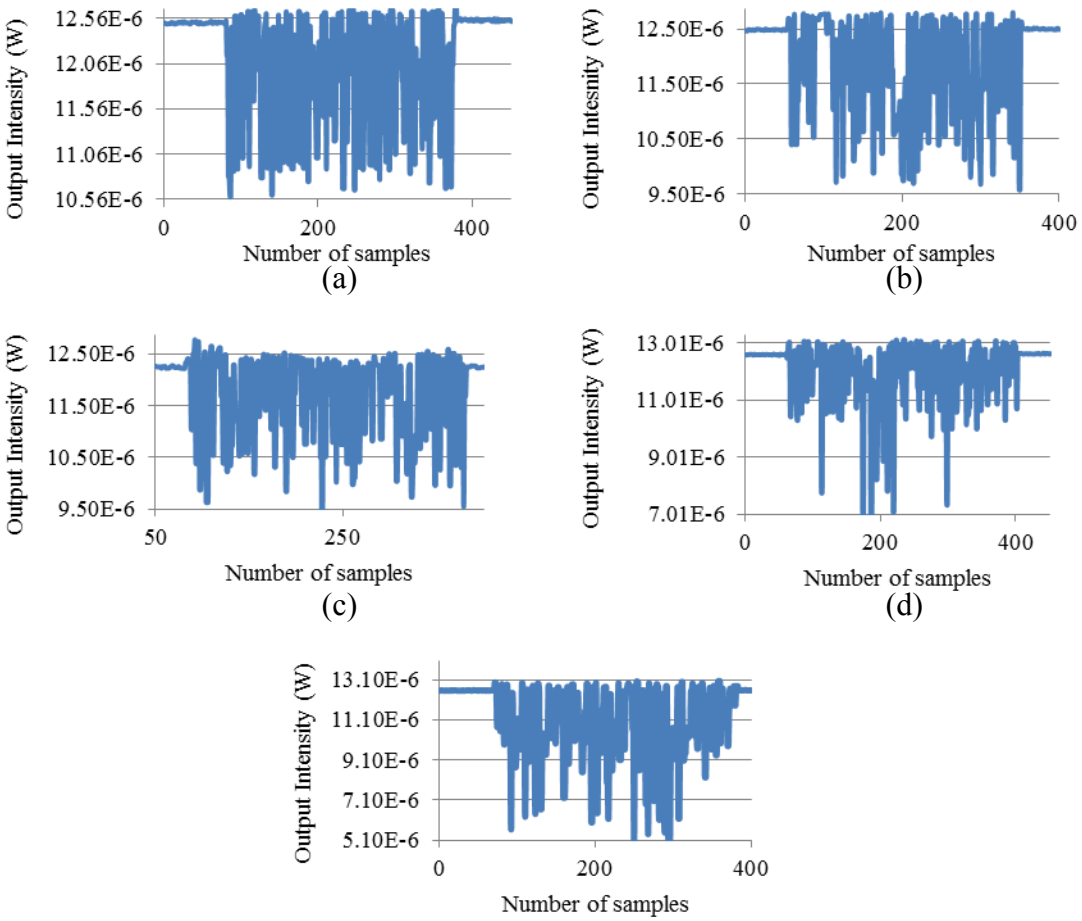

Figure B-6: 4 Springs 200 µm at 20 Hz accelerometer graphs

Table B-6: Output intensity difference from the 4 Springs 200 µm at 20 Hz graphs

	B-6 (a)	**B-6 (b)**	**B-6 (c)**	**B-6 (d)**	**B-6 (e)**
Signal and amplitude	20 Hz 2 V	20 Hz 4 V	20 Hz 6 V	20 Hz 8V	20 Hz 10 V
Output Intensity Difference	1.45 µW	1.99 µW	2.15 µW	4.8 µW	6.45 µW

Appendix B (Continued)

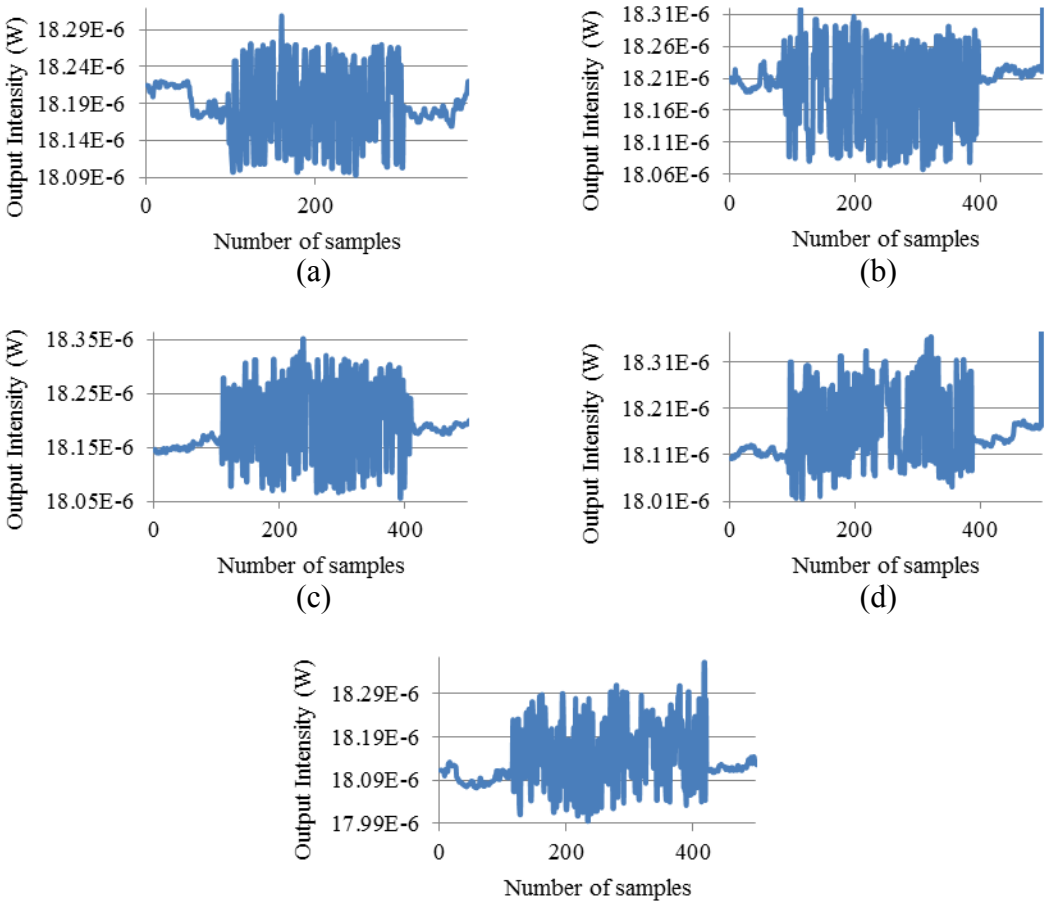

Figure B-7: 8 Springs 100 µm at 10 Hz accelerometer graphs

Table B-7: Output intensity difference from the 8 Springs 100 µm at 10 Hz graphs

	B-7 (a)	**B-7 (b)**	**B-7 (c)**	**B-7 (d)**	**B-7 (e)**
Signal and amplitude	10 Hz 2 V	10 Hz 4 V	10 Hz 6 V	10 Hz 8V	10 Hz 10 V
Output Intensity Difference	67.7 nW	127.2 nW	133.9 nW	159.9 nW	181.3 nW

Appendix B (Continued)

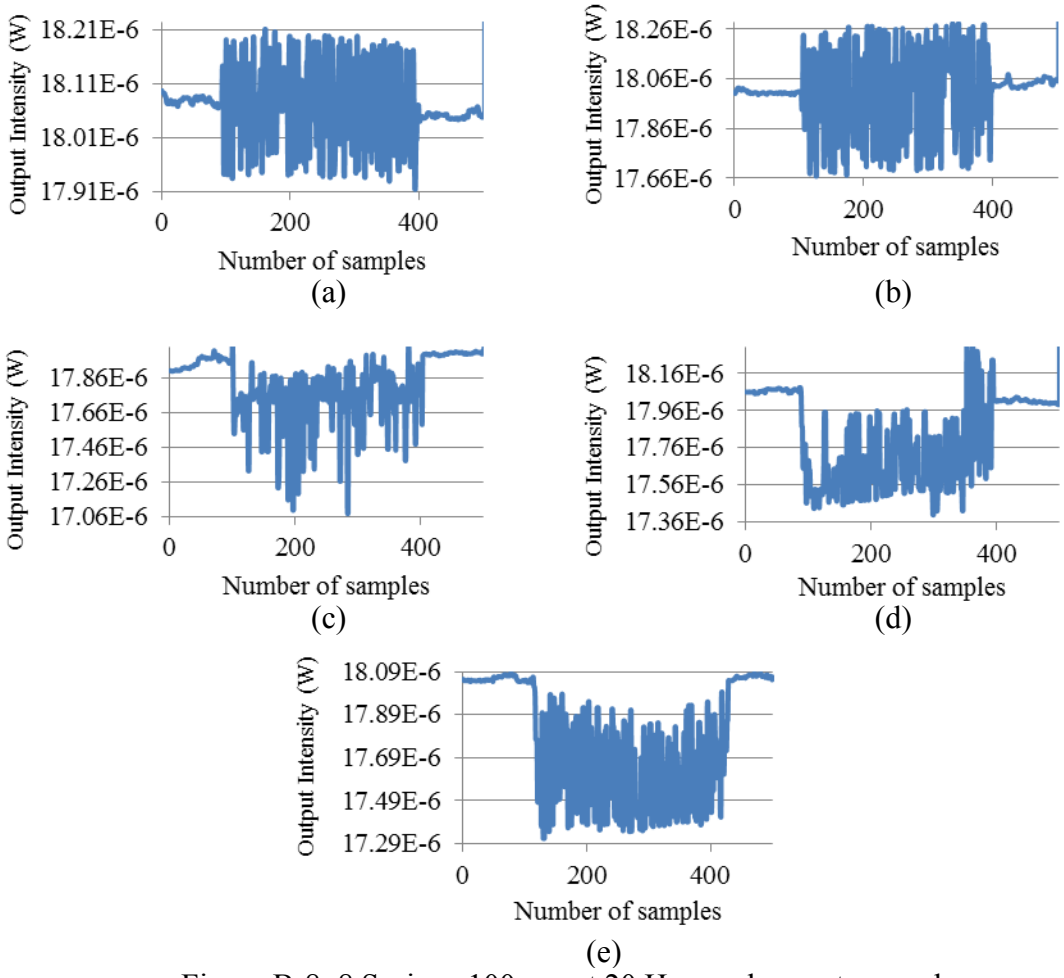

Figure B-8: 8 Springs 100 µm at 20 Hz accelerometer graphs

Table B-8: Output intensity difference from the 8 Springs 100 µm at 20 Hz graphs

	B-8 (a)	B-8 (b)	B-8 (c)	B-8 (d)	B-8 (e)
Signal and amplitude	20 Hz 2 V	20 Hz 4 V	20 Hz 6 V	20 Hz 8V	20 Hz 10 V
Output Intensity Difference	130.0 nW	325. 0nW	543.5 nW	568.6 Nw	704.5 nW

Appendix B (Continued)

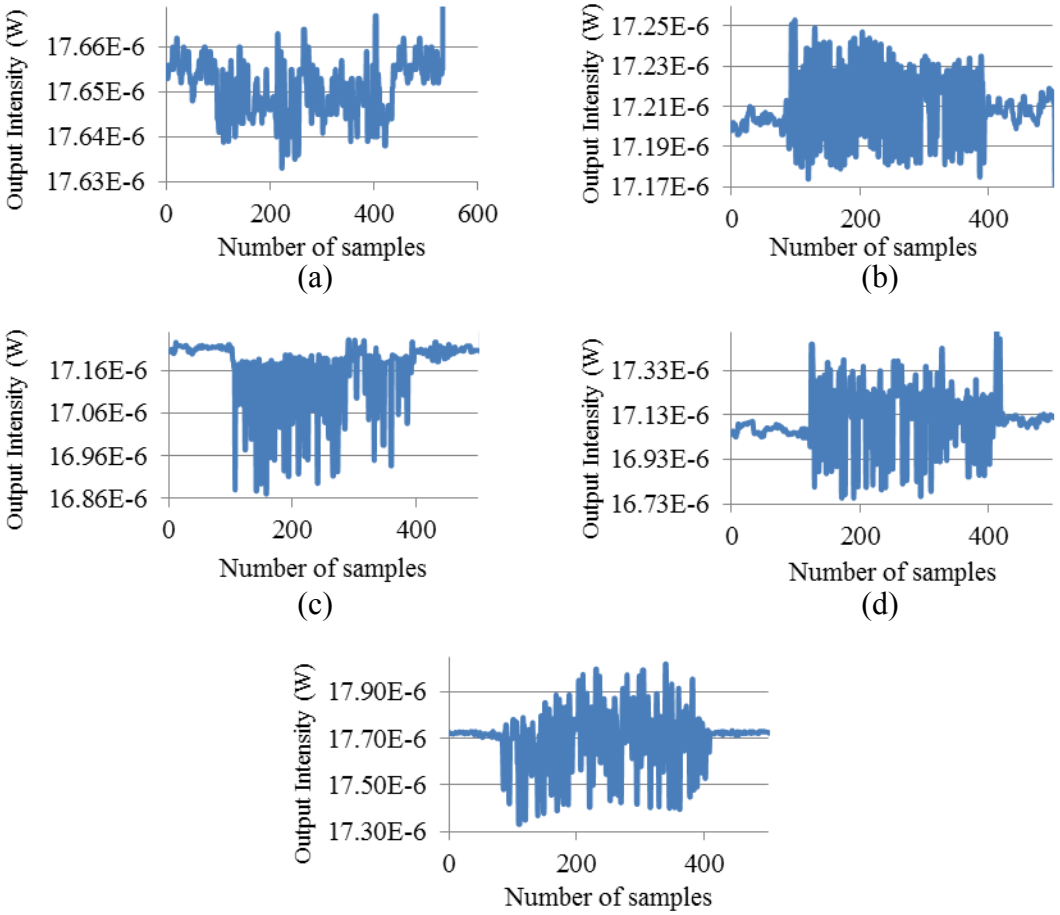

Figure B-9: 8 Springs 150 µm at 10 Hz accelerometer graphs

Table B-9: Output intensity difference from the 8 Springs 150 µm at 10 Hz graphs

	B-9 (a)	**B-9 (b)**	**B-9 (c)**	**B-9 (d)**	**B-9 (e)**
Signal and amplitude	10 Hz 2 V	10 Hz 4 V	10 Hz 6 V	10 Hz 8V	10 Hz 10 V
Output Intensity Difference	20.3 nW	25.3 nW	248.7 nW	291.5 nW	315.7 nW

Appendix B (Continued)

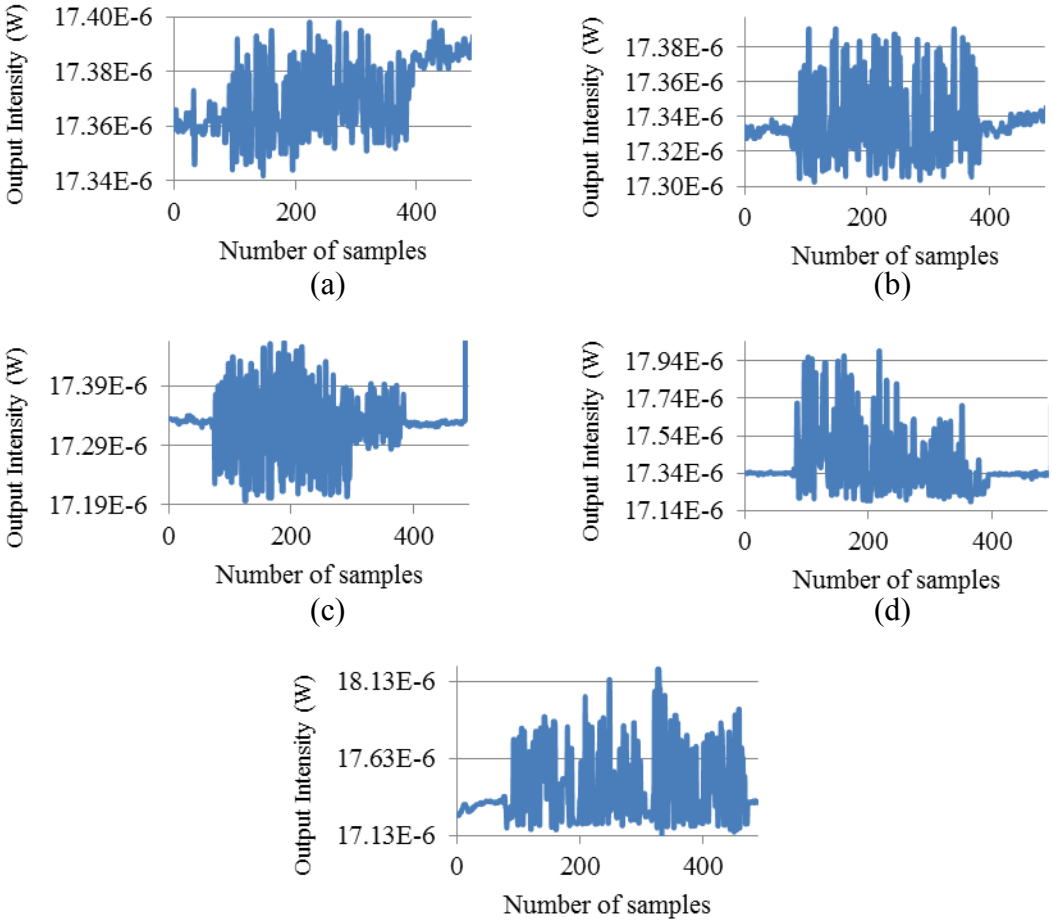

Figure B-10: 8 Springs 150 µm at 20 Hz accelerometer graphs

Table B-10: Output intensity difference from the 8 Springs 150 µm at 20 Hz graphs

	B-10 (a)	**B-10 (b)**	**B-10 (c)**	**B-10 (d)**	**B-10 (e)**
Signal and amplitude	20 Hz 2 V	20 Hz 4 V	20 Hz 6 V	20 Hz 8V	20 Hz 10 V
Output Intensity Difference	17.3 nW	44.0 nW	117.3 nW	503.5 nW	602.2 nW

Appendix B (Continued)

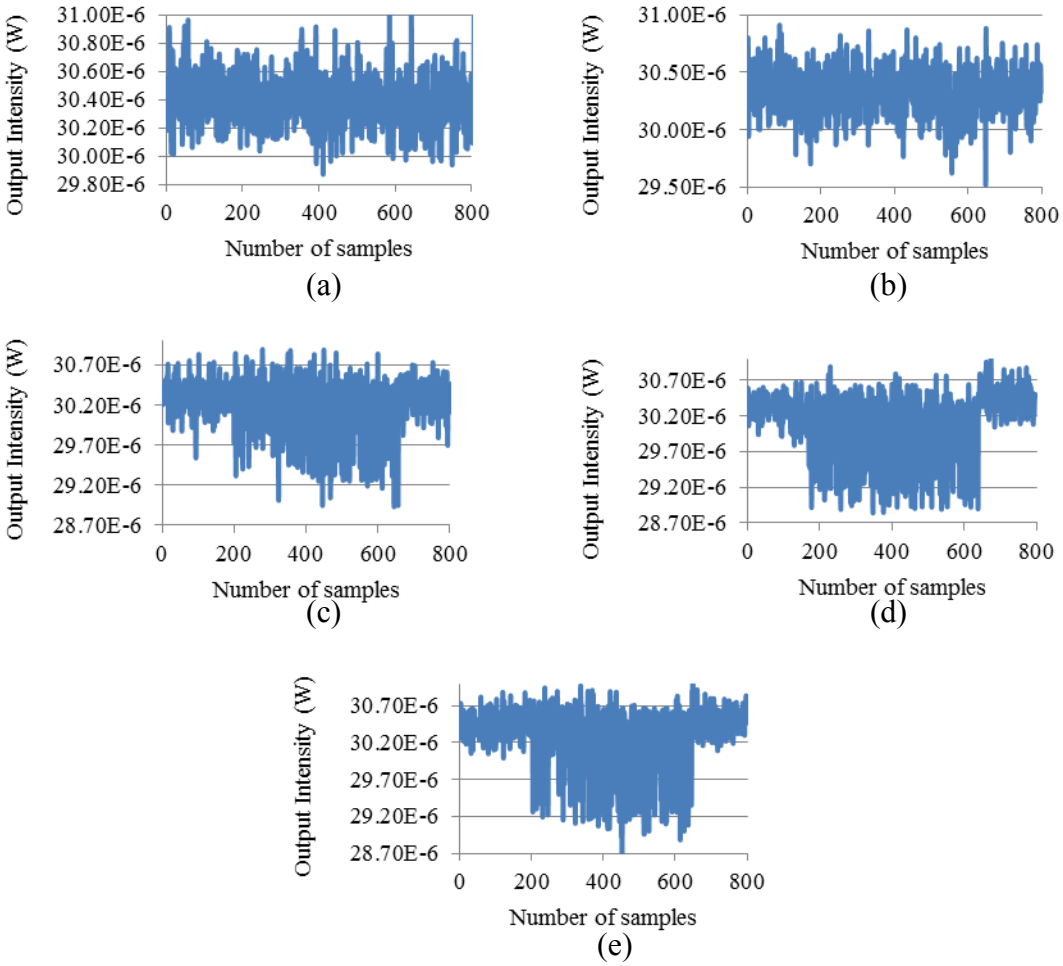

Figure B-11: 8 Springs 200 µm at 10 Hz accelerometer graphs

Table B-11: Output intensity difference from the 8 Springs 200 µm at 10 Hz graphs

	B-11 (a)	**B-11 (b)**	**B-11 (c)**	**B-11 (d)**	**B-11 (e)**
Signal and amplitude	10 Hz 2 V	10 Hz 4 V	10 Hz 6 V	10 Hz 8V	10 Hz 10 V
Output Intensity Difference	262.3 nW	357.2 nW	900.7 nW	1.3 µW	1.5 µW

Appendix B (Continued)

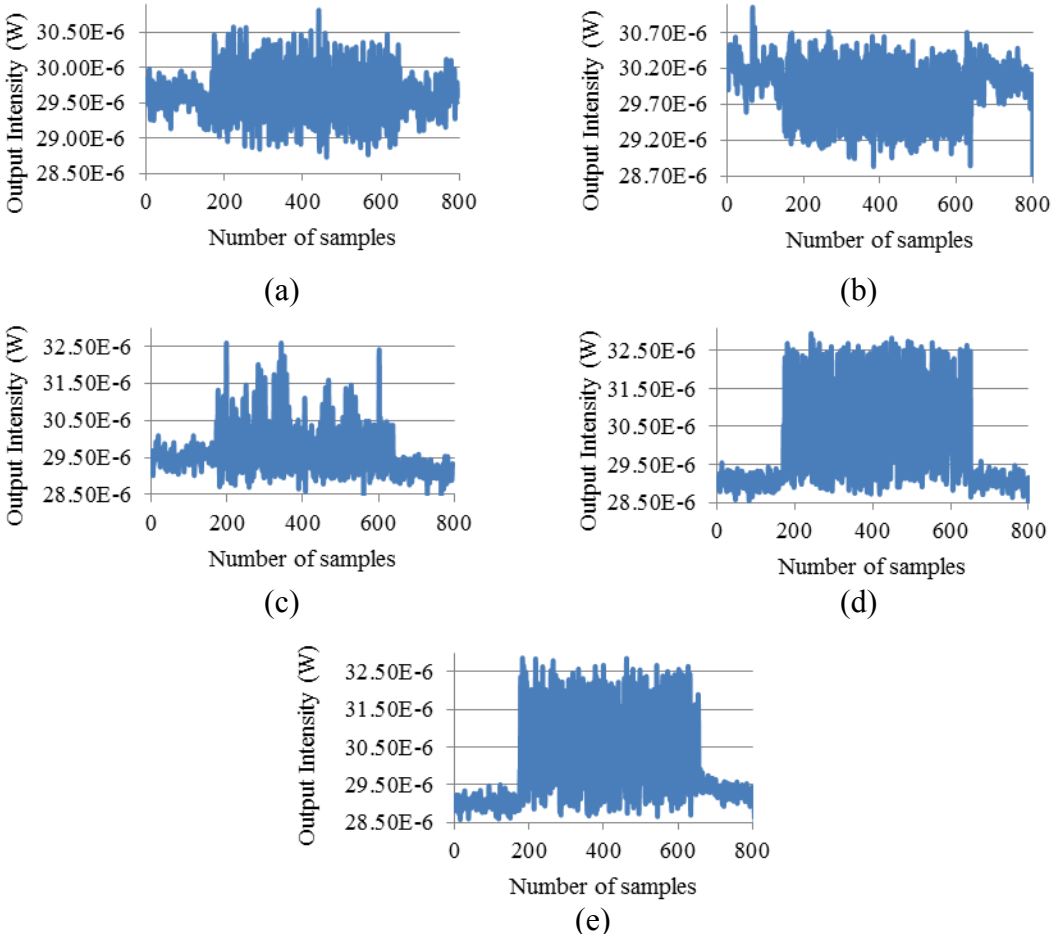

Figure B-12: 8 Springs 200 µm at 20 Hz accelerometer graphs

Table B-12: Output intensity difference from the 8 Springs 200 µm at 20 Hz graphs

	B-12 (a)	**B-12 (b)**	**B-12 (c)**	**B-12 (d)**	**B-12 (e)**
Signal and amplitude	20 Hz 2 V	20 Hz 4 V	20 Hz 6 V	20 Hz 8V	20 Hz 10 V
Output Intensity Difference	661.2 nW	860.8 nW	1.4 µW	2.9 µW	3.4 µW

About the Author

Mr. Al-Aakhir A. Rogers is completing his doctoral degree in electrical engineering at the University of South Florida (USF). He received both his B.S. and M.S. in Electrical Engineering from North Carolina Agricultural and Technical State University in Greensboro, NC.

During his tenure in the doctoral program, Al-Aakhir presented his research at the NATO Advanced Study Institute Optical Waveguide Sensing & Imaging in Medicine, Environment, Security and Defense in Ontario, Canada (October 2006). In 2007, he conducted research at the Nanotechnology Division of the Instrument Technology Research Center in Hsinchu, Taiwan as a recipient of the National Science Foundation (NSF) – East Asia Pacific Summer Institutes (EAPSI) Fellowship Program. He served as an NSF proposal reviewer for the EAPSI program from 2008 to 2010. Al-Aakhir was invited to give a lecture and present a poster at the 13th Meeting on Optical Engineering and Science in Tel-Aviv, Israel from March 9-10, 2011. Al-Aakhir has authored two first-author peer-reviewed publications, received a provisional patent for his dissertation research, and earned several awards and honors, including the 2010 USF Golden Bull and USF Diversity Honor Roll Awards, 2nd place, Outstanding Student Poster at the 2010 Great Minds in STEM Conference, and an Honorable Mention selection for the 2010 Ford Foundation Diversity Dissertation Fellowship.